

Nanomaterials for Optical Sensing and Sensors: Plasmonics, Raman, and Optofluidics

Guest Editors: Zhida Xu, Meng Lu, Hyunjong Jin, Tao Chen, and Tiziana C. Bond





Nanomaterials for Optical Sensing and Sensors: Plasmonics, Raman, and Optofluidics

Journal of Nanomaterials

Nanomaterials for Optical Sensing and Sensors: Plasmonics, Raman, and Optofluidics

Guest Editors: Zhida Xu, Meng Lu, Hyunjong Jin, Tao Chen,
and Tiziana C. Bond



Copyright © 2015 Hindawi Publishing Corporation. All rights reserved.

This is a special issue published in "Journal of Nanomaterials." All articles are open access articles distributed under the Creative Commons Attribution License, which permits unrestricted use, distribution, and reproduction in any medium, provided the original work is properly cited.

Editorial Board

Domenico Acierno, Italy
Katerina Aifantis, USA
Sheikh Akbar, USA
Nageh K. Allam, USA
Margarida Amaral, Portugal
Raul Arenal, Spain
Ilaria Armentano, Italy
Lavinia Balan, France
Thierry Baron, France
Andrew R. Barron, USA
Hongbin Bei, USA
Stefano Bellucci, Italy
Enrico Bergamaschi, Italy
Debes Bhattacharyya, New Zealand
Giovanni Bongiovanni, Italy
Theodorian Borca-Tasciuc, USA
Mohamed Bououdina, Bahrain
Torsten Brezesinski, Germany
C. Jeffrey Brinker, USA
Christian Brosseau, France
Yibing Cai, China
Chuanbao Cao, China
Victor M. Castao, Mexico
Albano Cavaleiro, Portugal
Bhanu P. S. Chauhan, USA
Yuan Chen, Singapore
Wei Chen, China
Tupei Chen, Singapore
Shafiq Chowdhury, USA
Jin-Ho Choy, Korea
Kwang-Leong Choy, UK
Yu-Lun Chueh, Taiwan
Elisabetta Comini, Italy
Giuseppe Compagnini, Italy
David Cornu, France
Miguel A. Correa-Duarte, Spain
P. Davide Cozzoli, Italy
Majid Darroudi, Iran
Shadi A. Dayeh, USA
Luca Deseri, USA
Yong Ding, USA
Bin Dong, China
Zehra Durmus, Turkey
Joydeep Dutta, Oman
Ali Eftekhari, USA
Samy El-Shall, USA
Farid El-Tantawy, Egypt
Ovidiu Ersen, France
Claude Estourns, France
Andrea Falqui, Saudi Arabia
Xiaosheng Fang, China
Bo Feng, China
Matteo Ferroni, Italy
Wolfgang Fritzsche, Germany
Alan Fuchs, USA
Peng Gao, China
Miguel A. Garcia, Spain
Siddhartha Ghosh, Singapore
P. K. Giri, India
Russell E. Gorga, USA
Jihua Gou, USA
Jean M. Greneche, France
Changzhi Gu, China
Lin Guo, China
John Zhanhu Guo, USA
Smrati Gupta, Germany
Kimberly Hamad-Schifferli, USA
Michael Harris, USA
Jr-Hau He, Taiwan
Nguyen D. Hoa, Vietnam
Michael Z. Hu, USA
Nay Ming Huang, Malaysia
Shaoming Huang, China
Qing Huang, China
David Hui, USA
Zafar Iqbal, USA
Balachandran Jeyadevan, Japan
Xin Jiang, Germany
Rakesh Joshi, Australia
Jeong-won Kang, Republic of Korea
Hassan Karimi-Maleh, Iran
Antonios Kelarakis, UK
Alireza Khataee, Iran
Ali Khorsand Zak, Iran
Dojin Kim, Republic of Korea
Wonbaek Kim, Republic of Korea
Philippe Knauth, France
Ralph Krupke, Germany
Christian Kbel, Germany
Sushil Kumar, India
Sanjeev Kumar, India
Prashant Kumar, UK
Subrata Kundu, India
Michele Laus, Italy
Eric Le Bourhis, France
Burtrand Lee, USA
Jun Li, Singapore
Shijun Liao, China
Meiyong Liao, Japan
Silvia Licocchia, Italy
Wei Lin, USA
Jun Liu, USA
Zainovia Lockman, Malaysia
Songwei Lu, USA
Jue Lu, USA
Ed Ma, USA
Malik Maaza, South Africa
Lutz Mädler, Germany
Gaurav Mago, USA
Morteza Mahmoudi, Iran
Mohammad A. Malik, UK
Devanesan Mangalaraj, India
Sanjay R. Mathur, Germany
Paulo Cesar Morais, Brazil
Mahendra A. More, India
Paul Munroe, Australia
Jae-Min Myoung, Republic of Korea
Rajesh R. Naik, USA
Albert Nasibulin, Russia
Toshiaki Natsuki, Japan
Koichi Niihara, Japan
Sherine Obare, USA
Won-Chun Oh, Republic of Korea
Atsuto Okamoto, Japan
Abdelwahab Omri, Canada
Ungyu Paik, Republic of Korea
Edward A. Payzant, USA
Ton Peijs, UK
Oscar Perales-Pérez, Puerto Rico
Wenxiu Que, China
Peter Reiss, France
Orlando Rojas, USA
Marco Rossi, Italy
Cengiz S. Ozkan, USA
Vladimir Šepelák, Germany



Huaiyu Shao, Japan
Prashant Sharma, USA
Donglu Shi, USA
Bhanu P. Singh, India
Surinder Singh, USA
Vladimir Sivakov, Germany
Yanlin Song, China
Ashok Sood, USA
Marinella Striccoli, Italy
Jing Sun, China
Xuping Sun, Saudi Arabia
Ashok K. Sundramoorthy, USA
Sabine Szunerits, France
Nyan-Hwa Tai, Taiwan

Bo Tan, Canada
Ion Tiginyanu, Moldova
Valeri P. Tolstoy, Russia
Muhammet S. Toprak, Sweden
Ramon Torrecillas, Spain
Takuya Tsuzuki, Australia
Tamer Uyar, Turkey
Bala Vaidhyanathan, UK
Luca Valentini, Italy
Rajender S. Varma, USA
Antonio Villaverde, Spain
Ajayan Vinu, Australia
Ruibing Wang, Macau
Shiren Wang, USA

Yong Wang, USA
Magnus Willander, Sweden
Ping Xiao, UK
Zhi Li Xiao, USA
Shuangxi Xing, China
Yangchuan Xing, USA
Doron Yadlovker, Israel
Piaoping Yang, China
Yoke K. Yap, USA
Ramin Yousefi, Iran
Kui Yu, Canada
William W. Yu, USA
Renyun Zhang, Sweden
Myung-Hwa Jung, Republic of Korea

Contents

Nanomaterials for Optical Sensing and Sensors: Plasmonics, Raman, and Optofluidics, Zhida Xu, Meng Lu, Hyunjong Jin, Tao Chen, and Tiziana C. Bond
Volume 2015, Article ID 162537, 3 pages

Investigating the Fabrication Imperfections of Plasmonic Nanohole Arrays and Its Effect on the Optical Transmission Spectra, Amr M. Mahros and Marwa M. Tharwat
Volume 2015, Article ID 178583, 8 pages

Molecular Logic Computation with Debugging Method, Xiangrong Liu, Juan Suo, Juan Liu, Yan Gao, and Xiangxiang Zeng
Volume 2015, Article ID 120365, 11 pages

FRET-Based Detection of Enzymatic Reaction of Botulinum on Microfluidic Device, Young Min Bae, Seung Oh Jin, Insoo Kim, and Ki Young Shin
Volume 2015, Article ID 126598, 7 pages

Investigation of the Validity of the Universal Scaling Law on Linear Chains of Silver Nanoparticles, Mohammed Alsawafta, Mamoun Wahbeh, and Vo-Van Truong
Volume 2015, Article ID 983413, 12 pages

Immobilization Techniques and Integrated Signal Enhancement for POC Nanocolor Microfluidic Devices, Marlies Schlauf, Saied Assadollahi, Roland Palkovits, Peter Pointl, and Thomas Gerhard Maria Schalkhammer
Volume 2015, Article ID 386794, 10 pages

Focused Ion Beam Assisted Interface Detection for Fabricating Functional Plasmonic Nanostructures, Houxiao Wang, Wei Zhou, and Er Ping Li
Volume 2015, Article ID 468069, 9 pages

Editorial

Nanomaterials for Optical Sensing and Sensors: Plasmonics, Raman, and Optofluidics

Zhida Xu,¹ Meng Lu,² Hyunjong Jin,³ Tao Chen,⁴ and Tiziana C. Bond⁵

¹University of Illinois at Urbana-Champaign, Urbana, IL 61801, USA

²Iowa State University, Ames, IA 50011, USA

³Samsung Electronics, Hwaseong, Gyeonggi, Republic of Korea

⁴Shanghai Institute of Technical Physics, Chinese Academy of Sciences, Shanghai 200083, China

⁵Lawrence Livermore National Laboratory, Livermore, CA 94550, USA

Correspondence should be addressed to Zhida Xu; zhidaxu1@illinois.edu

Received 6 August 2015; Accepted 13 August 2015

Copyright © 2015 Zhida Xu et al. This is an open access article distributed under the Creative Commons Attribution License, which permits unrestricted use, distribution, and reproduction in any medium, provided the original work is properly cited.

To date, environmental and healthcare problems have become the most important and challenging issues globally. Demands for fast and low-cost sensing methods and devices for environment monitoring [1], point-of-care diagnosis [2], and food and water safety control [3] are growing rapidly over the years, especially in the underdeveloped areas. Thanks to the advancement of nanotechnology in the past decade, nanomaterials, especially when combined with modern optical sensing techniques, provide us with many new tools, such as surface-enhanced Raman spectroscopy [4], surface plasmon resonance [5], photonic crystal [6], and optofluidics [7], for the sensing applications not accessible by traditional sensing techniques. In the recent decade the research in this field has become flourishing. Figure 1 shows the number of publications in this field according to Thomson Reuters' Web of Science. From Figure 1 we can see that the number of scientific publications has been sky-rocketing. In order to cover the recent progress and ongoing work in this booming field, this timely special issue is dedicated to synthesis, fabrication, characterization, and numerical modeling of nanomaterials and nanostructures with potential applications in biomedical researches [8], environment monitoring [9, 10], explosives trace detection [11], and so on.

This special issue contains 6 articles which cover the academic fields of environmental science, materials science, life science, nanotechnology, optics, physics, and chemistry.

In the research article "Investigation of the Validity of the Universal Scaling Law on Linear Chains of Silver Nanoparticles," M. Alsawaf et al. examined (the generalization of) the universal scaling behavior for spherical silver nanoparticles arranged in finite linear chains (eight nanoparticles) and embedded in different host media. The results of simulation show that the plasmon ruler equation can be successfully extended to represent the fractional plasmon shift of many interacting nanoparticles. The decay length and the amount of the fractional shift of the silver linear chains strongly depend on the polarization state of the incident polarization. The LM exhibits a significant shift of the plasmon resonance (indicated by the value of k) as compared to that of the TM. This can be explained by the fact that the enhancement of the local field under parallel polarization is more pronounced. On the other hand, the decay of the TM shows a strong dependency on the dielectric function of the surrounding medium. It decays twice faster than the LM, as the host medium becomes denser.

In the research article "Focused Ion Beam Assisted Interface Detection for Fabricating Functional Plasmonic Nanostructures," H. Wang et al. proposed the FIB-assisted interface detection and successfully carried out it using the sample-absorbed current as the detection signal, and the patterning depth control for the plasmonic structure fabrication was achieved through controlling machining time or ion dose using the EPM. Material-dependent currents were measured

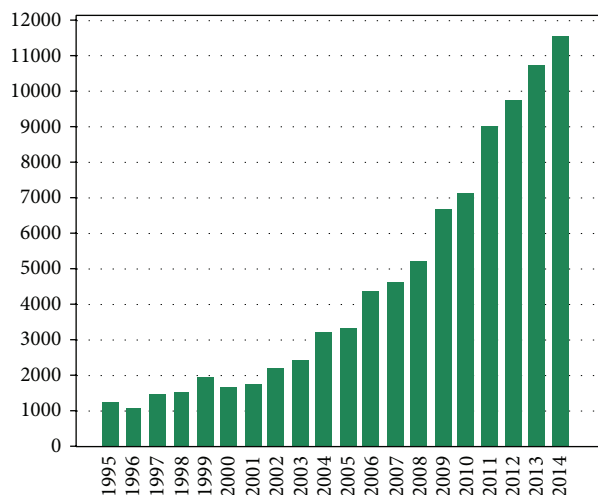


FIGURE 1: Number of publications in the field of optical sensing based on plasmonics and Raman spectroscopy for each year from 1995 to 2014. Source from Thomson Reuters' Web of Science.

through the EPM signal curves, and the quantitative models for the sample-absorbed currents and the ion beam current were also developed.

In the research article "Immobilization Techniques and Integrated Signal Enhancement for POC Nanocolor Microfluidic Devices," M. Schlauf et al. reported the development of a silver enhancement technology that operates even in the presence of high chloride concentrations as it may be encountered in biologic samples. The silver enhancement reagents may be integrated into the microfluidic assay platform to be released upon sample addition. Hereby a highly sensitive one-step-assay can be realized. M. Schlauf et al. also demonstrated that adsorptive immobilization via a cationic polymeric interlayer is a competitive and fast technique for the binding of the capture protein streptavidin onto planar SiO_2 -surfaces such as REA biochips.

In the research article "Investigating the Fabrication Imperfections of Plasmonic Nanohole Arrays and its Effect on the Optical Transmission Spectra," A. M. Mahros et al. investigated the extraordinary optical transmission spectra of thin gold films perforated with imperfect nano hole arrays using the finite difference time domain (FDTD) method. Exponential shapes for the nanohole sidewalls are used. The investigation of transmission spectra of imperfect nanohole arrays has not previously been demonstrated. It was found that the asymmetry between the two openings of the circular nanoholes or bending to their sidewalls strongly modifies both of the intensity and resonance positions of the transmission spectra. Furthermore, the results of this study assist in explaining the technicality of extraordinary optical transmission phenomenon and why some experimental results on transmission differ from those expected.

In the research article "FRET-Based Detection of Enzymatic Reaction of Botulinum on Microfluidic Device," Y. M. Bae et al. implemented a microfluidic device to detect the enzymatic reaction of botulinum toxin A (BTA) using Förster resonance energy transfer (FRET). The microfluidic

device comprised a main channel having two loading zones, a reaction chamber, and a side channel perpendicular to the main channel. The reaction chamber defined by weir in the main channel was packed with microbeads. The movement of the peptide substrate and the BTA in the microfluidic device was controlled by electrophoresis, and the enzymatic reaction of the BTA was detected through the changes of the fluorescence intensity in the reaction chamber. As a result, it was observed that the enzymatic reaction was affected by the electric voltage applied for the movement of the BTA and the peptide and improved by packing the microbeads in the reaction chamber. The microfluidic device provides with the tool to investigate the proteolysis of the substrate by the BTA.

In the research article "Molecular Logic Computation with Debugging Method," X. Liu et al. considered constructing full adder and serial binary adder, using the new concept of seesaw gate. The simulation of the full adder preformed properly as designed; however, unexpected exception is noted in the simulation of the serial binary adder. To identify and address the exception, they propose a new method for debugging the molecular circuit. The main idea for this method is to add fan-outs to monitor the circuit in a reverse stepwise manner. These fan-outs are fluorescent signals that can obtain the real-time concentration of the target molecule. By analyzing the monitoring result, the exception can be identified and located. In this paper, examples of XOR and serial binary adder circuits are described to prove the practicability and validity of the molecular circuit debugging method.

Acknowledgments

The guest editorial team would like to thank the authors for their contributions to this special issue and the reviewers for their time and dedication.

Zhida Xu
Meng Lu
Hyunjong Jin
Tao Chen
Tiziana C. Bond

References

- [1] C. K. Ho, A. Robinson, D. R. Miller, and M. J. Davis, "Overview of sensors and needs for environmental monitoring," *Sensors*, vol. 5, no. 1-2, pp. 4-37, 2005.
- [2] R. Kumar, G. P. Singh, I. Barman, N. C. Dingari, and G. Nabi, "A facile and real-time spectroscopic method for biofluid analysis in point-of-care diagnostics," *Bioanalysis*, vol. 5, no. 15, pp. 1853-1861, 2013.
- [3] R. H. Farahi, A. Passian, L. Tetard, and T. Thundat, "Critical issues in sensor science to aid food and water safety," *ACS Nano*, vol. 6, no. 6, pp. 4548-4556, 2012.
- [4] Z. Xu, J. Jiang, M. R. Gartia, and G. L. Liu, "Monolithic integrations of slanted silicon nanostructures on 3D microstructures and their application to surface-enhanced raman spectroscopy," *Journal of Physical Chemistry C*, vol. 116, no. 45, pp. 24161-24170, 2012.

- [5] A. G. Brolo, "Plasmonics for future biosensors," *Nature Photonics*, vol. 6, no. 11, pp. 709–713, 2012.
- [6] J. Li, M. D. Muntasir Hossain, B. Jia, D. Buso, and M. Gu, "Three-dimensional hybrid photonic crystals merged with localized plasmon resonances," *Optics Express*, vol. 18, no. 5, pp. 4491–4498, 2010.
- [7] Z. Xu, K. Han, I. Khan, X. Wang, and G. L. Liu, "Liquid refractive index sensing independent of opacity using an optofluidic diffraction sensor," *Optics Letters*, vol. 39, no. 20, pp. 6082–6085, 2014.
- [8] D. J. Bornhop, J. C. Latham, A. Kussrow, D. A. Markov, R. D. Jones, and H. S. Sørensen, "Free-solution, label-free molecular interactions studied by back-scattering interferometry," *Science*, vol. 317, no. 5845, pp. 1732–1736, 2007.
- [9] Z. Xu, Y. Chen, M. R. Gartia, J. Jiang, and G. L. Liu, "Surface plasmon enhanced broadband spectrophotometry on black silver substrates," *Applied Physics Letters*, vol. 98, no. 24, Article ID 241904, 2011.
- [10] W. Shotyk and M. Krachler, "Contamination of bottled waters with antimony leaching from polyethylene terephthalate (PET) increases upon storage," *Environmental Science and Technology*, vol. 41, no. 5, pp. 1560–1563, 2007.
- [11] A. Chou, E. Jaatinen, R. Buividas et al., "SERS substrate for detection of explosives," *Nanoscale*, vol. 4, no. 23, pp. 7419–7424, 2012.

Research Article

Investigating the Fabrication Imperfections of Plasmonic Nanohole Arrays and Its Effect on the Optical Transmission Spectra

Amr M. Mahros^{1,2} and Marwa M. Tharwat³

¹Department of Physics, King Abdulaziz University, Jeddah 21432, Saudi Arabia

²Department of Engineering Mathematics and Physics, Alexandria University, Alexandria 21544, Egypt

³Department of Electrical Engineering, King Abdulaziz University, Jeddah 21432, Saudi Arabia

Correspondence should be addressed to Amr M. Mahros; amr.mahros@mena.vt.edu

Received 24 November 2014; Revised 26 February 2015; Accepted 27 February 2015

Academic Editor: Meng Lu

Copyright © 2015 A. M. Mahros and M. M. Tharwat. This is an open access article distributed under the Creative Commons Attribution License, which permits unrestricted use, distribution, and reproduction in any medium, provided the original work is properly cited.

We investigate the extraordinary optical transmission spectra of thin gold films perforated with imperfect nanohole arrays using the finite difference time domain (FDTD) method. Exponential shapes for the nanohole sidewalls are used. To the best of our knowledge, such investigation of transmission spectra of imperfect nanohole arrays has not previously been demonstrated. It was found that the asymmetry between the two openings of the circular nanoholes or bending to their sidewalls strongly modifies both the intensity and resonance positions of the transmission spectra. Furthermore, the results of this study assist in explaining the technicality of extraordinary optical transmission phenomenon and why some experimental results on transmission differ from those expected.

1. Introduction

Metallic film perforated with periodic nanohole arrays is considered as one of the most interesting plasmonic structures and received a significant amount of attention. The extraordinary optical transmission spectra (EOT) of such structures have been the focus of considerable research activities. Discovery of EOT was first reported by Ebbesen in 1998 [1]. Numerous amounts of theoretical and experimental work about these structures are carried out by current researchers about investigating their optical properties.

The extraordinary behaviors, of the perforated metallic film, are largely due to the presence of surface plasmons (SPs), which can be excited by illuminating the film using a Gaussian beam. It was found in the literature that the coupling/decoupling phenomenon between SPs of patterned metallic film and incident light results in appearance of multiple resonance peaks in the transmission spectrum [2].

The EOT can be tuned through many physical and geometrical parameters including the hole shape, size, and

depth as well as film material, substrate refractive index, and array period. Arrays with simple aperture shapes can be tuned to resonate at much shorter wavelengths than those of complex hole shapes, such as annular, cross-shaped, and X-shaped apertures. However, more tunability had been achieved by applying a magnetic field [3–9].

The key parameters of these plasmonic structures are metal type, holes shape and dimensions, refractive index of surrounding environment, and structural periodicity which have significant impact on the resonance wavelength and its intensity. However, the impact of fabricating imperfect nanoholes on the transmission spectrum has not yet been investigated in the literature. Nanoholes fabrication imperfections may result in disparity between their two apertures or bending to their sidewalls.

Surface plasmons (SPs) and EOT have been recently employed in a myriad of applications including biomedical sensing, efficient solar cells, fluorescence microscopy, photothermal therapy, and fabrication of nanoantennas [10–12].

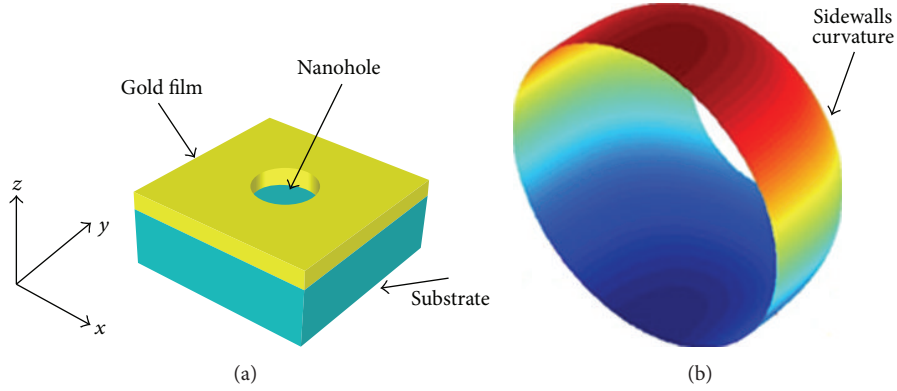


FIGURE 1: (a) A unit cell of a circular nanohole array perforated in a gold film. (b) Imperfect nanohole of asymmetric openings and sidewalls of exponential shape.

In this paper, we use the 3D finite difference time domain (FDTD) method to investigate the optical transmission spectrum of gold films patterned with imperfect circular nanoholes. We study the impact of changing the shape of imperfection on transmission spectra as a function of the nanohole depth, sidewalls tapering coefficient, and the imperfection ratio of asymmetric openings, showing that large modification can be achieved with realistic parameters. The impacts of independently varying these parameters are separately considered in our simulations, and the results are summarized in the following subsections.

This paper is organized as follows: the reported structure and FDTD simulation parameters are described in Section 2. Section 3 represents the optical transmission spectral responses of the designed plasmonic arrays and discussions for the effect of varying different key parameters. Finally, Section 4 provides conclusions of the obtained results.

2. Structure Description and FDTD Simulation

In this work, optical transmission spectra of the reported plasmonic imperfect nanohole arrays are obtained by solving Maxwell's equations of different materials using the FDTD algorithm. The FDTD method is applied by using the OptiFDTD simulation tool from Optiwave, Inc. The designed plasmonic structure layout is a circular nanohole array perforated in gold thin film "sandwiched" between glass substrate and air cladding as shown in Figure 1(a). The structural periodicity was 500 nm and the gold film thickness was 200 nm.

In Cartesian coordinates x , y , and z periodic boundary conditions were used in the x and y directions, while anisotropic perfect matching layer was used in the z -direction to serve as absorbing boundary condition. The frequency dependent relative permittivity $\epsilon_r(\omega)$ of the dispersive gold film is characterized by Lorentz-Drude model:

$$\epsilon_r(\omega) = \epsilon_\infty + \sum_{m=1}^N \frac{f_m \omega_{om}^2}{\omega_{om}^2 - \omega^2 + i\omega\Gamma_m}, \quad (1)$$

where ϵ_∞ denotes the permittivity at infinite frequency, f_m is a function of position specifying the oscillator strengths, and Γ_m is the damping coefficient. The incident wave frequency and the resonant frequencies are, respectively, represented by ω and ω_{om} . For the substrate layer, $\epsilon(\omega)$ was assumed as n^2 (n is the refractive index).

In order to realize a broadband simulation on the dispersive gold film, Gaussian modulated electromagnetic plane wave source was used. The continuous waves are centred at 680 nm, linearly polarized in y -direction, and convoluted with a Gaussian envelope function. The light pulse in time domain has an offset time of 0.8×10^{-14} s and half width of 1×10^{-14} s.

The simulation was performed at normal incidence (z -direction) of the plane wave through the nanohole arrays. The calculation mesh resolution was as high as 5 nm ($<0.1\lambda$). The simulation runs for 5,000 time steps for a calculation time of 100 fs. An x - y observation area will perform and calculate the transmission spectral analysis at 200 nm away from the gold/substrate interface.

Figure 1(b) shows the shape of the imperfect hole used during this simulation. Exponential shape for the nanohole sidewalls is used to express imperfection according to the following equation:

$$R(Z) = R_S + \frac{R_E - R_S}{e^{-\alpha} - 1} \left(e^{(-\alpha/d)Z} - 1 \right), \quad (2)$$

where $R(z)$ represents the radius of the nanohole along its axis at different positions over the gold film of thickness d such that $z = 0$ and $z = d$ at the air/gold and the gold/substrate interfaces, respectively. The nanohole openings radii at the air/gold and the gold/substrate interfaces are, respectively, denoted by R_S and R_E . The sidewalls exponential tapering coefficient is represented by α . Figure 2 shows some examples for the shape of the nonlinear exponential tapered sidewalls at different values of α when $R_S = 200$ nm, $d = 200$ nm, and $R_E = 125$ nm. The imperfection ratio is defined as ratio of the difference between the two openings' radii to the radius of the nanohole at the gold/substrate interface ($\delta R/R_E$).

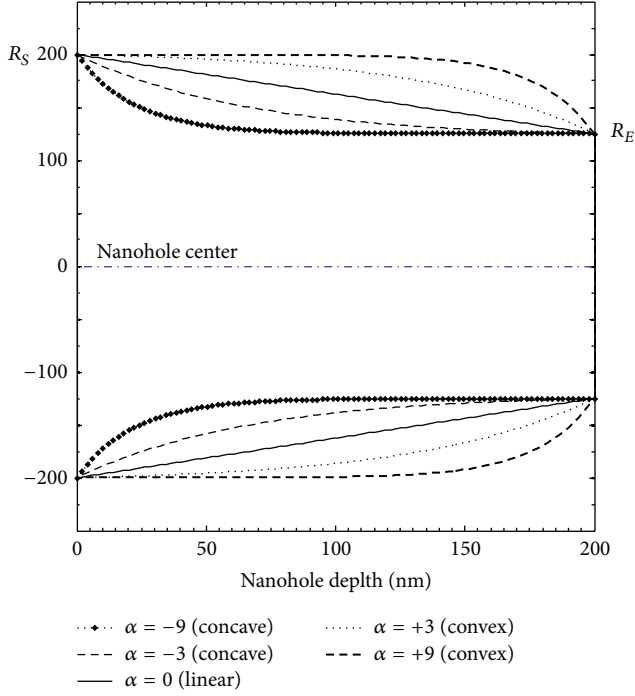


FIGURE 2: Examples for the shape of the exponential tapered sidewalls at different values of α .

3. Optical Transmission Spectral Responses of Nanohole Arrays

In our simulations, using the FDTD method, we looked at the optical transmission spectrum of the reported plasmonic imperfect nanohole array as a function of different structural parameters such as the sidewalls exponential tapering coefficient, the imperfection ratio between the two asymmetric openings, and nanohole depth. The impacts of independently varying these parameters are separately considered in our simulations, and the results are summarized in the following subsections.

3.1. Tapering Coefficient. In this subsection, we investigate modifying the transmission spectra of the gold-perforated imperfect nanohole arrays by bended sidewalls due to fabrication imperfections. The sidewalls exponential tapering coefficient was changed from -9 to 9 passing through zero associated with linearly tapered sidewalls. During this study, the nanohole depth and opening radii at air/gold and the gold/substrate are kept constants at 200 nm, 125 nm, and 200 nm, respectively.

Figure 3 shows the transmission spectra of the designed structure at different values of the tapering coefficient α . The results of Figure 3 exhibit the presence of two groups of resonance. The first group $R_S = 200$ nm is located at wavelengths less than 800 nm, while the second group “P2” is found at wavelengths larger than 800 nm.

It was found in the literature that these two sets of resonance wavelengths are associated with the air/gold and the gold/substrate interfaces. At normal incidence, the SP

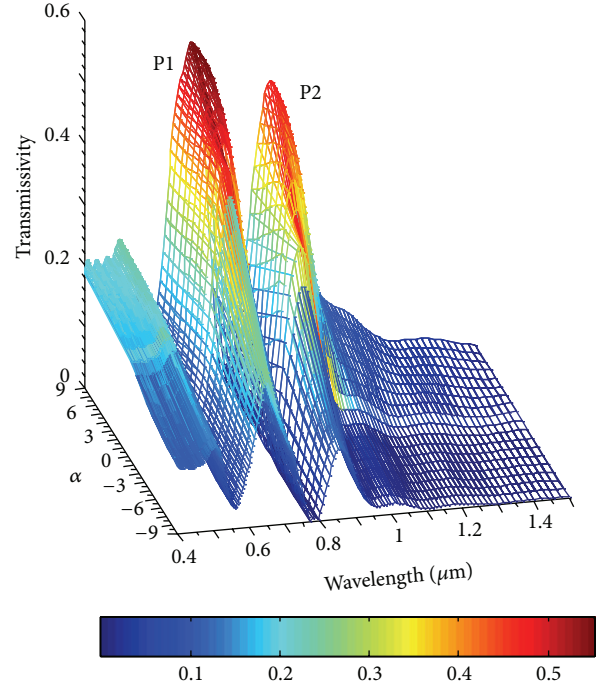


FIGURE 3: Optical transmission spectra of gold thin film perforated with imperfect nanoholes at different values of α .

resonance wavelengths λ_{SP} of a circular nanohole array can be approximated by the following equation:

$$\lambda_{SP}(i, j) = \text{Re} \left(\frac{\Lambda}{\sqrt{i^2 + j^2}} \sqrt{\frac{\epsilon_d \epsilon_m}{\epsilon_d + \epsilon_m}} \right), \quad (3)$$

where ϵ_d and ϵ_m , respectively, represent the relative permittivities of the adjacent medium and the metal and (i, j) are integers. Λ represents the structural periodicity value. The SP resonance wavelength in the range of 650 – 700 nm “P1” can be assigned to $\lambda_{SP}(1, 1)$ of the air/gold interface, while the resonance wavelength found at values larger than 800 nm “P2” is related to $\lambda_{SP}(1, 0)$ the gold/substrate interface.

Figure 4 shows the impact of changing the tapering coefficient on the position of the resonance wavelengths and the corresponding transmission peaks associated to “P1” and “P2” resonances.

As demonstrated in Figures 4(a) and 4(b), as α increases, the resonance wavelengths exhibit a clear redshift. The red shift may be attributed to the change of the effective depth of the nanohole. As α increases, the effective length of the resonator increases as shown in Figure 2. For higher absolute values of the exponential tapering coefficient, the sidewalls show monotony surface resulting in a fixed effective length of the resonator and constant resonance wavelengths.

Additionally, Figures 4(c) and 4(d) show the impact of changing α on the transmission peak intensity of “P1” and “P2”, respectively. The illustrated results demonstrate that the peak intensity values of “P1” and “P2” monotonically increase

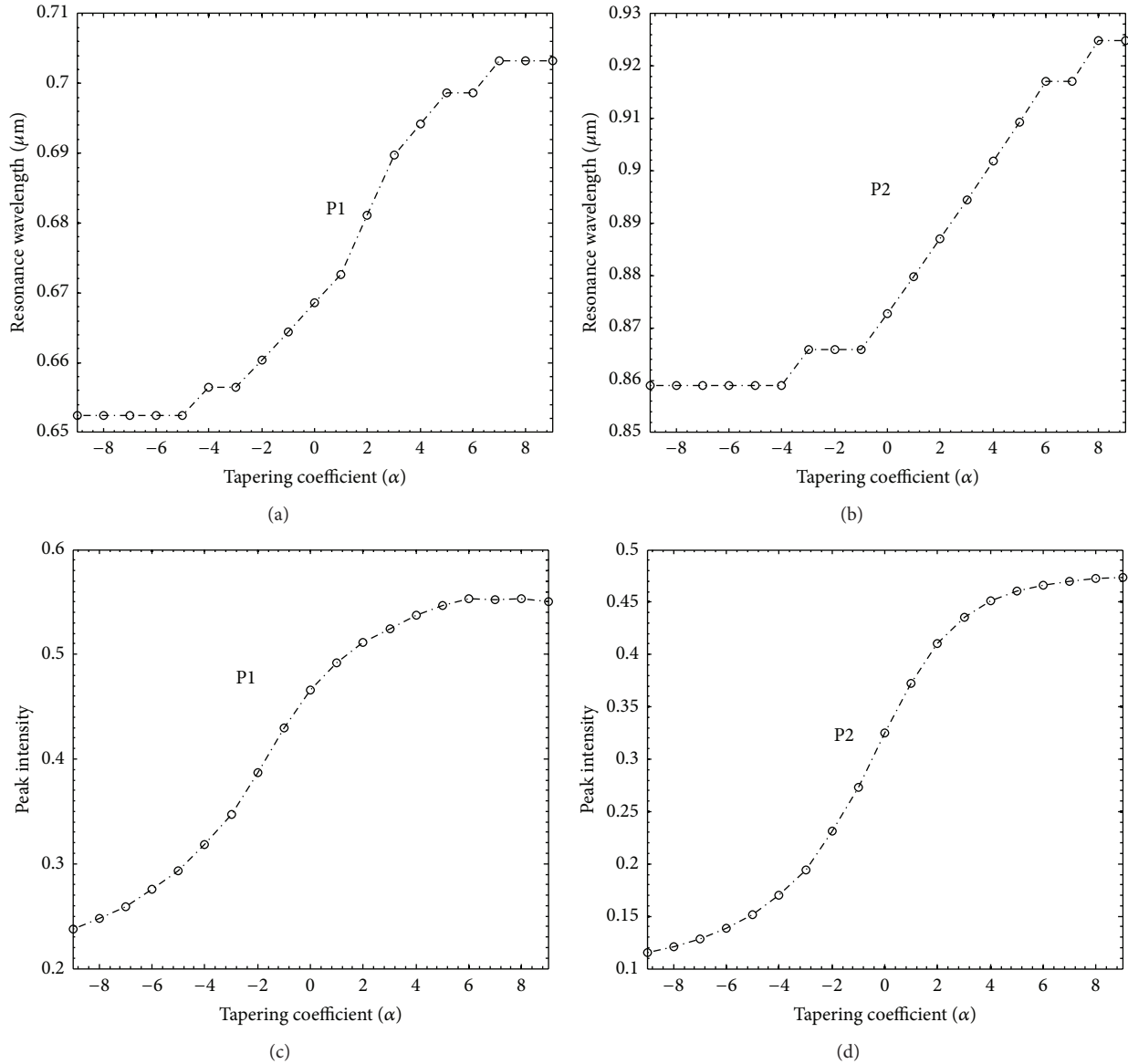


FIGURE 4: Effect of changing α on the position of resonance wavelengths of (a) “P1” and (b) “P2.” Impact of changing α on the transmission peak intensity of (c) “P1” and (d) “P2.”

with increasing α till it saturates at higher values of the tapering coefficient.

This happens because positive values of α provide convex metallic sidewalls which collect more optical energy to funnel to the other side of the metal surface. On the other hand, negative values of α define concave metallic sidewalls which are associated with higher reflection and lower transmission.

In comparison to the perfect circular nanohole arrays, Bethe predicted that the transmission peak intensity values of such structures are proportional to R^4 . Therefore, the difference in peak transmission coefficient can perhaps be attributed to the differences in “effective” hole radius.

3.2. Imperfection Ratio. In this subsection, we investigate the effect of changing the imperfection ratio ($\delta R/R_E$), up to 80%,

on the transmission spectra of the gold-perforated imperfect nanohole arrays. During this investigation, the nanohole depth and radius at gold/substrate interface remain constants at 200 nm and 125 nm, respectively. Note that changing the imperfection ratio, from 0 to 0.8, results in a change of enter opening radius from 125 nm to 225 nm. However, the exit opening radius is fixed at 125 nm.

Figure 5 demonstrates the modifying transmission spectra through gold-perforated imperfect nanohole array due to the change of $\delta R/R_E$. These simulations were performed for two arrays with different sidewalls tapering coefficients such that Figures 5(a) and 5(b) are illustrated for $\alpha = 4$ and $\alpha = 8$, respectively. The radius of the nanohole along its axis decreases between the air/gold interface and the gold/substrate interface following the exponential profile.

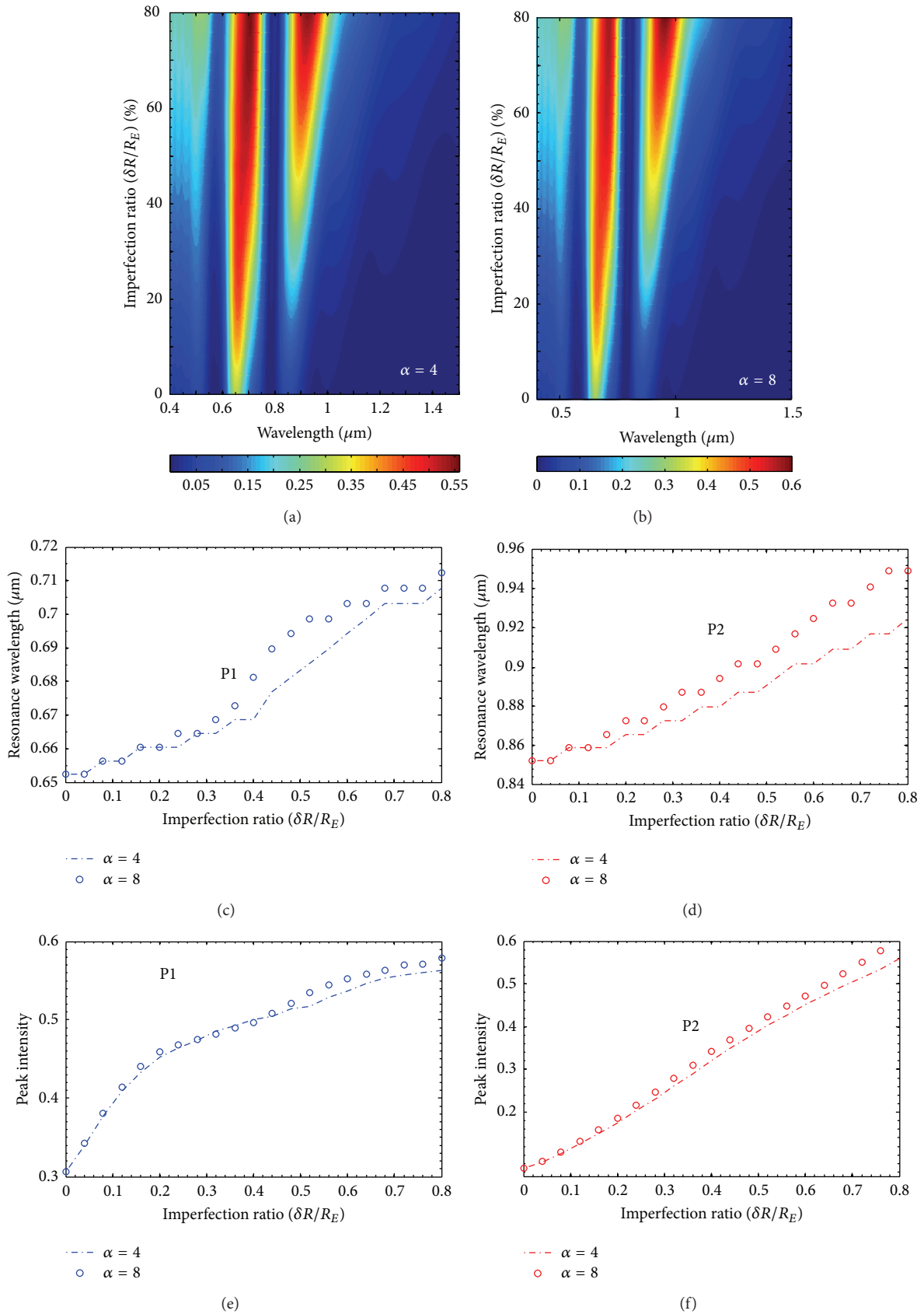


FIGURE 5: Effect of changing the imperfection ratio on (a) the transmission spectra ($\alpha = 4$), (b) the transmission spectra ($\alpha = 8$), the position of resonance wavelengths of (c) “P1” and (d) “P2,” and the transmission peak intensity of (e) “P1” and (f) “P2.”

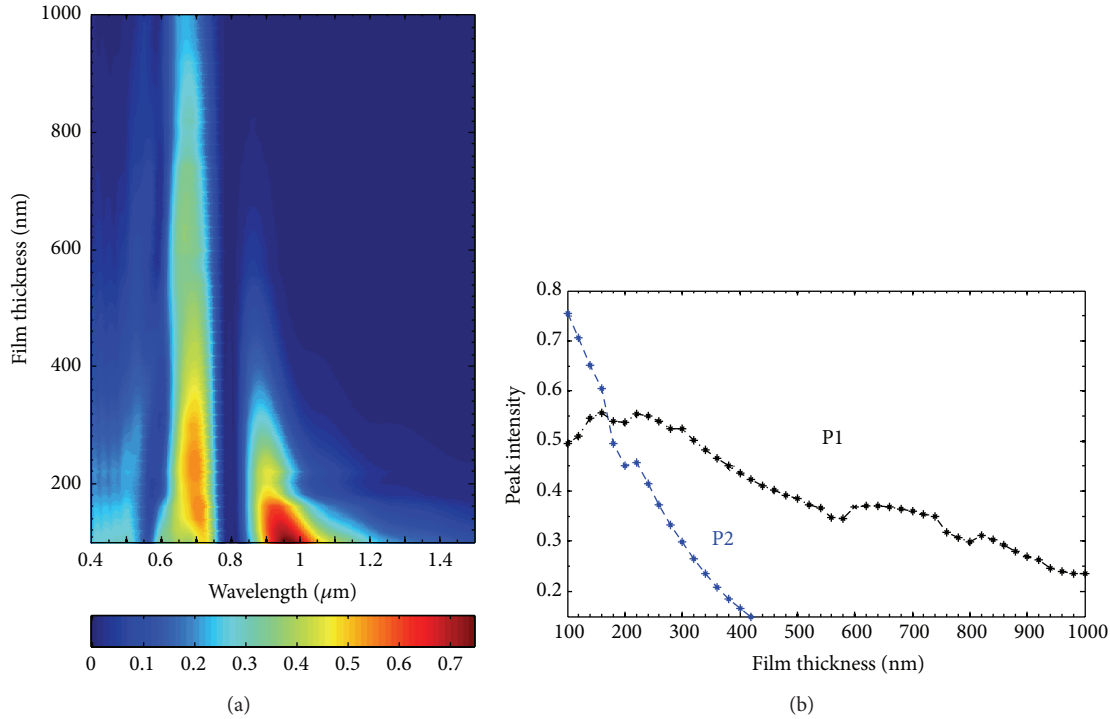


FIGURE 6: Effect of changing the imperfect nanohole depth on (a) the transmission spectra and (b) the transmission peak intensity of “P1” and “P2.”

Imperfect nanohole array with $\alpha = 4$ shows a higher decreasing rate than that of one with $\alpha = 8$.

It can be seen from Figures 5(c) and 5(e) that the peak transmittance and resonance wavelength of “P1” slightly change with increasing imperfection ratio. In sharp contrast, a clear red shift in the resonance position and dramatically ascent in the intensity of “P2” is achieved as shown in Figures 5(d) and 5(f).

As the imperfection ratio increases, the nonlinearity of the tapered exponential sidewalls increases. It is expected that increasing the nonlinearity magnifies the tunneling of light via coupled plasmonic modes localized in the nanohole. As the distance between the gold surfaces narrows, the localized plasmon polariton gets stronger. This might allow most of energy to flow inside the tapered nanohole and it is coupled with SP waves on the inner sidewalls. Increasing the confinement will result in red shift.

The impact of changing $\delta R/R_E$ on the resonance wavelength and the peak transmission of “P2” are almost double the effect on “P1.” This may be attributed to the fact that the exponential profile shows higher slope and hence stronger impact on “P2” at the gold/substrate interface than that on “P1” at the air/gold interface.

Furthermore, as shown in Figure 2, the impact of the sidewalls tapering coefficient on the slope of the sidewalls appears at higher values of z near the exit opening at gold/substrate interface. As a result, both the peak intensity and resonance wavelength of “P2” are notably influenced changing α as demonstrated in Figures 5(d) and 5(f). However, changing α

almost has no effect on both the peak intensity and resonance wavelength of “P1” as illustrated in Figures 5(c) and 5(e).

3.3. Nanohole Depth. In this subsection, the behavior of optical transmission spectra of the reported plasmonic structure is presented with changing the distance between the two asymmetry openings. We use the following parameters: $\Lambda = 500$ nm, $R_S = 200$ nm, $R_E = 125$ nm, $\alpha = 4$, and d in the range from 100 nm to 1000 nm. The impact of changing film thickness on the intensity and resonance positions of the transmission spectra is shown in Figure 6.

Figure 6(a) shows the two groups of peaks “P1” and “P2.” For film thickness higher than 400 nm, “P2” is totally suppressed and only “P1” is delivered. That will be useful in design of visible and near infrared photonic-based optical devices. Changing the film thickness almost has no impact on the resonance wavelengths of both “P1” and “P2.” Figure 6(b) demonstrates that the transmission peak intensity of “P1” slightly decreases with increasing nanohole depth. In sharp contrast, the intensity of “P2” suffers severe degradation with increasing the depth.

For further investigation, the spatial distribution of the total magnetic and electric field intensities at the middle of the nanohole is demonstrated in Figure 7. In Figure 7(a), magnetic field distribution in yz plane indicates that strong field is accumulating on the upper surface of the perfect nanohole. In sharp contrast, Figure 7(b) shows energy penetration into the imperfect nanohole with low reflections. The electric field distribution is localized on the air/gold interface of the perfect

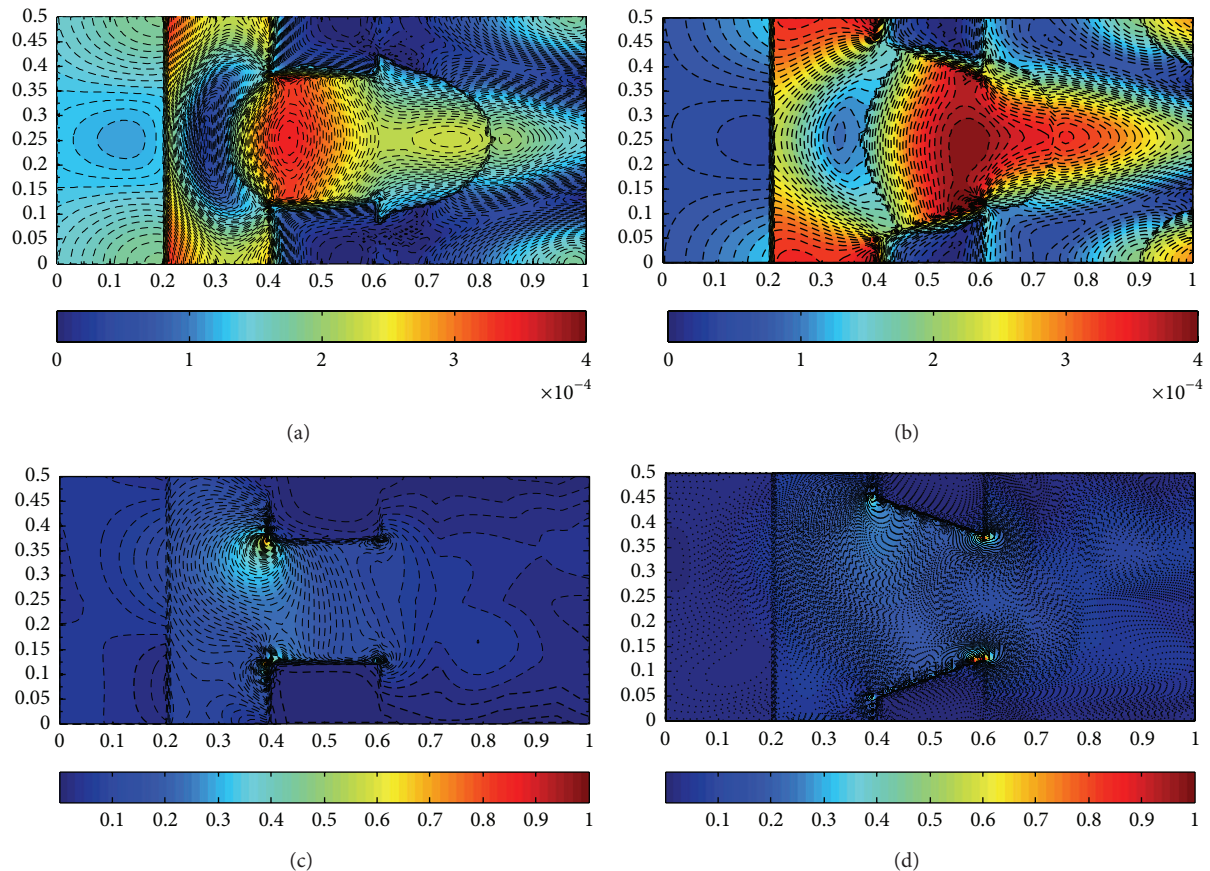


FIGURE 7: Spatial distribution of the total magnetic and electric field intensities in yz plane at the middle of the nanohole.

nanohole as shown in Figure 7(c). However, large entering radius at the air/gold interface and tapered sidewalls of the imperfect nanohole lead to concentration of the electric field at narrow exiting radius at the gold/glass substrate.

4. Conclusion

In this work, we comprehensively investigate the EOT properties of the imperfect circular plasmonic nanohole arrays. Using the FDTD method, we investigate the impact of several key parameters including nanohole depth, ratio between the asymmetric openings, and sidewalls tapering coefficient on the transmission spectra of thin gold films perforated with imperfect nanohole arrays. A notable red shift in the resonance wavelength of the plasmonic wave at the gold/substrate interface is achieved with increasing either the sidewalls tapering coefficient or the imperfection ratio. However, increasing film thickness causes a notable degradation in the transmission intensity above 400 nm.

Conflict of Interests

The authors declare that there is no conflict of interests regarding the publication of this paper.

References

- [1] T. W. Ebbesen, H. J. Lezec, H. F. Ghaemi, T. Thio, and P. A. Wolff, "Extraordinary optical transmission through sub-wavelength hole arrays," *Nature*, vol. 391, no. 6668, pp. 667–669, 1998.
- [2] H. F. Ghaemi, T. Thio, D. E. Grupp, T. W. Ebbesen, and H. J. Lezec, "Surface plasmons enhance optical transmission through subwavelength holes," *Physical Review B*, vol. 58, no. 11, pp. 6779–6782, 1998.
- [3] S. M. Orbons, M. I. Haftel, C. Schlockermann et al., "Dual resonance mechanisms facilitating enhanced optical transmission in coaxial waveguide arrays," *Optics Letters*, vol. 33, no. 8, pp. 821–823, 2008.
- [4] L. Lin and A. Roberts, "Light transmission through nanostructured metallic films: coupling between surface waves and localized resonances," *Optics Express*, vol. 19, no. 3, pp. 2626–2633, 2011.
- [5] R. Biswas, S. Neginhal, C. G. Ding, I. Puscasu, and E. Johnson, "Mechanisms underlying extraordinary transmission enhancement in subwavelength hole arrays," *Journal of the Optical Society of America B: Optical Physics*, vol. 24, no. 10, pp. 2589–2596, 2007.
- [6] T. Vallius, J. Turunen, M. Mansuripur, and S. Honkanen, "Transmission through single subwavelength apertures in thin metal films and effects of surface plasmons," *Journal of the Optical Society of America A: Optics and Image Science, and Vision*, vol. 21, no. 3, pp. 456–463, 2004.

- [7] A. K. Azad, Y. Zhao, W. Zhang, and M. He, "Effect of dielectric properties of metals on terahertz transmission subwavelength hole arrays," *Optics Letters*, vol. 31, no. 17, pp. 2637–2639, 2006.
- [8] M. J. Kofke, D. H. Waldeck, Z. Fakhraai, S. Ip, and G. C. Walker, "The effect of periodicity on the extraordinary optical transmission of annular aperture arrays," *Applied Physics Letters*, vol. 94, no. 2, Article ID 023104, 2009.
- [9] A. Battula, S. Chen, Y. Lu, R. J. Knize, and K. Reinhardt, "Tuning the extraordinary optical transmission through subwavelength hole array by applying a magnetic field," *Optics Letters*, vol. 32, no. 18, pp. 2692–2694, 2007.
- [10] R. Wannemacher, "Plasmon-supported transmission of light through nanometric holes in metallic thin films," *Optics Communications*, vol. 195, no. 1–4, pp. 107–118, 2001.
- [11] G. C. des Francs, D. Molenda, U. C. Fischer, and A. Naber, "Enhanced light confinement in a triangular aperture: experimental evidence and numerical calculations," *Physical Review B: Condensed Matter and Materials Physics*, vol. 72, no. 16, Article ID 165111, 2005.
- [12] I. Ashry, B. Zhang, S. V. Stoianov et al., "Probing the photonic density of states using layer-by-layer self-assembly," *Optics Letters*, vol. 37, no. 11, pp. 1835–1837, 2012.

Research Article

Molecular Logic Computation with Debugging Method

Xiangrong Liu,¹ Juan Suo,¹ Juan Liu,² Yan Gao,¹ and Xiangxiang Zeng¹

¹Department of Computer Science, Xiamen University, Xiamen 361005, China

²Department of Electric and Computer Engineering, Institute of Physical and Mechanical and Electrical Engineering, Xiamen University, Xiamen 361005, China

Correspondence should be addressed to Xiangxiang Zeng; xzeng@xmu.edu.cn

Received 10 December 2014; Accepted 19 January 2015

Academic Editor: Zhida Xu

Copyright © 2015 Xiangrong Liu et al. This is an open access article distributed under the Creative Commons Attribution License, which permits unrestricted use, distribution, and reproduction in any medium, provided the original work is properly cited.

Seesaw gate concept, which is based on a reversible DNA strand branch process, has been found to have the potential to be used in the construction of various computing devices. In this study, we consider constructing full adder and serial binary adder, using the new concept of seesaw gate. Our simulation of the full adder preformed properly as designed; however unexpected exception is noted in the simulation of the serial binary adder. To identify and address the exception, we propose a new method for debugging the molecular circuit. The main idea for this method is to add fan-outs to monitor the circuit in a reverse stepwise manner. These fan-outs are fluorescent signals that can obtain the real-time concentration of the target molecule. By analyzing the monitoring result, the exception can be identified and located. In this paper, examples of XOR and serial binary adder circuits are described to prove the practicability and validity of the molecular circuit debugging method.

1. Introduction

In recent years, the gap between the finite capability of silicon and the infinite demand of consumers has widened gradually. This condition has given rise to molecular computing as an alternative approach to silicon-based computing. Molecular computing is aimed at building computational devices using various kinds of molecules, including organic molecules, proteins, nucleic acids, enzymes, and even supramolecular hydrogels [1–5]. Various computing devices have been constructed with biological molecules [6–12]. Given its parallel and microscopic nature, DNA has great data storage capacity and flexible design. It thus shows great potential as a material for large-scale information processing.

Several computing devices, such as logic gates, circuits, and tiny circuit boards, have been developed based on DNA molecules. In 2004, Stojanovic and Stefanovic proposed a series of molecular logic gate circuits based on nucleic acid catalysts [13]. In 2006, Seelig et al. reported the design and experimental implementation of DNA-based digital logic circuits using single-stranded nucleic acids [4]. In 2013, Zhang et al. established AND and OR gates based on DNA self-assembly and strand branch migration methods [12]. In

2014, a microfluidic half adder chip is achieved by controlling the annealing and denaturation of double-stranded DNA [14].

With complex and uncertain parameters (e.g., concentration and temperature) to balance, molecular circuits always function abnormally, just not as we expected. In 2009, Qian and Winfree proposed a simple DNA gate motif, a seesaw gate, that used a reversible strand displacement reaction based on the toehold exchange principle [15]. Zou et al. proposed a dynamic selection strategy which can be DNA coding [16]. Unlike circuits with other techniques that can only involve at most tens of gates, the seesaw catalytic gate architecture appeared suitable for practical synthesis of large-scale circuits involving possibly thousands of gates. Furthermore, it was argued that synthesis and preparation of circuit components can be parallel and scalable. To illustrate the potential of this approach, some logic circuits even a four-bit square-root circuit that comprised 130 DNA strands were shown in [15, 17], which all enabled fast and reliable function.

In this study, we aim to employ seesaw gates to construct an important computational component, adder. As we know, adders are the basic components of silicon-based computers and an indispensable component of all computer systems.

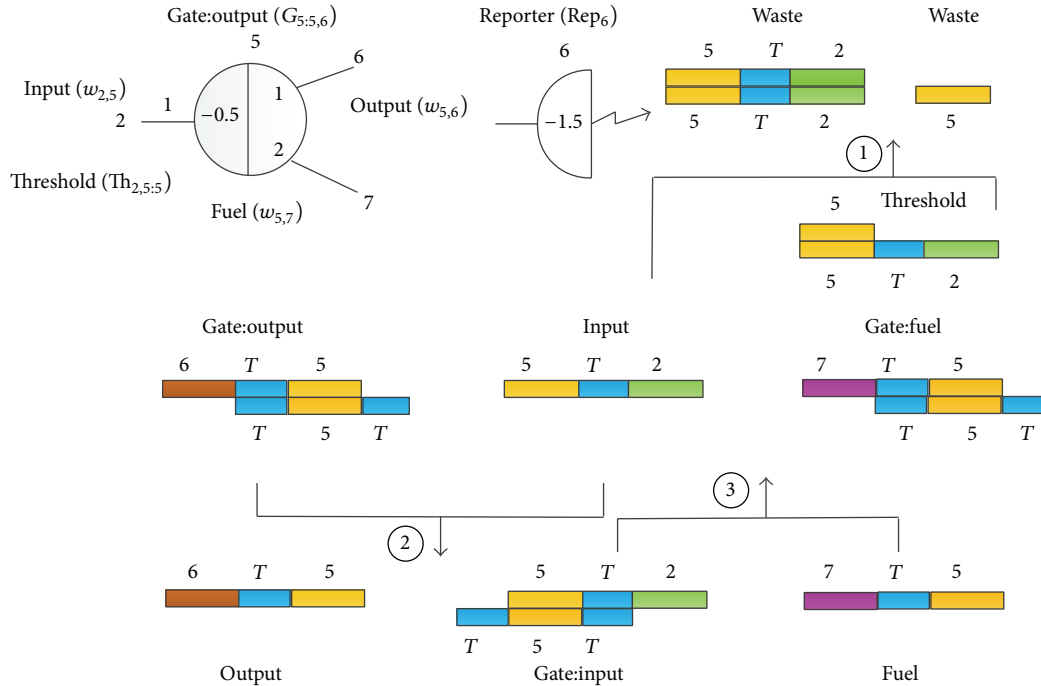


FIGURE 1: A simple DNA gate motif of seesaw gate.

Based on the seesaw gate concept proposed by Qian et al., we construct full adder and serial binary adder. As indicated by the term seesaw, the computing process is not static but a complex process of dynamic interaction, which can lead to a cyclic response based on DNA strand migration. With the recycling mechanism, the electrical adder can be transformed into some cyclic chemical reactions that can ensure a beneficial cycle in a long time. To test and verify the function of the molecular adder models, some simulations based on kinetic equations are performed. The simulation results show that the full adder yields expected results. However, the same is not achieved in the simulation of the serial binary adder, in which unexpected exception occurs. To identify and address this exception, we propose a method for debugging the molecular circuit by adding fluorescent signals to monitor the target molecule. As the fluorescent signals can detect the location of the exception, the abnormal circuit can be corrected using the error message.

The remainder of this paper is arranged as follows: the next section introduces the concept of seesaw gate; Section 3 describes the design and the simulation of full and serial binary adders based on seesaw gates; Section 4 proposes a debugging method for molecular circuits, and examples of XOR and serial binary adders are described to prove the practicability and validity of the debugging method; and conclusions and some open problems for future work are presented in Section 5.

2. Simple DNA Gate Motif, Seesaw Gate

In this section, we introduce a simple DNA gate motif, “seesaw” gate, which is an enzyme-free DNA machinery mainly

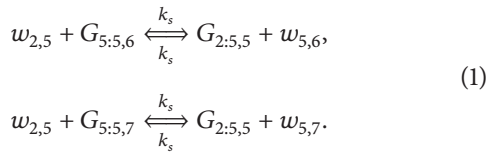
based on DNA strand migration [17, 18]. The entire reaction is a cyclic response, which means the reaction can work permanently in a self-motivated and self-directed way in a given condition. Typically, a threshold must be exceeded before catalysis occurs. When connected into circuits involving many interacting catalytic gates, complex circuit behavior can be obtained.

The reaction mechanism is a simplified version of the entropy-driven catalytic gate introduced in [15, 19]. The fundamental operation is toehold exchange, which is a toehold-mediated strand displacement reaction that results in a free right-side signal strand replacing a bound left-side signal strand. Figure 1 shows a simple DNA gate motif, seesaw gate. In the top left corner, it is abstract diagram for a seesaw gate and a reporter. Numbers ahead of or at the top of nodes indicate identities of nodes (or interfaces to those nodes in a network) and numbers within the nodes or on the wires indicate relative concentration of different initial DNA species. Each species plays a specific role (e.g., input is a single molecular; gate:output is a compound molecular) and has a unique name that is useful while translating the reactions into some equivalent kinetic equations (e.g., $w_{2,5}$ and $G_{5,5,6}$). The other part is about basic reaction mechanisms involved in a seesaw network, which consists of three parts: thresholding, seesawing, and reporting. First the threshold gate absorbs the input strand. When the threshold is exceeded, the input strand begins to displace the output strand from the gate:output complex. An analogous process then allows the fuel strand to similarly displace the input strand from the new gate:input complex, completing a catalytic cycle that has the net effect of exchanging one left-side signal strand in solution (the fuel) for another left-side signal strand (the output).

Finally, the output production can be acquired through the concentration of the reporter molecular. In principle, enough output can be obtained in a given condition with enough fuel and gate:output complex.

The chemical reactions described in Figure 1 can be equivalently translated into some kinetic equations. The main equations are shown below from (1) to (3). In these equations, $w_{2,5}$ and others indicate reacting molecular species, k_s indicates the slow strand displacement rate of seesawing and reporting reactions, and k_f indicates the fast strand displacement rate of thresholding reactions. Other side-reactions are ignored, which are also discussed in detail in [17].

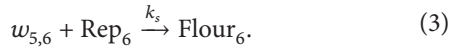
Seesawing reactions:



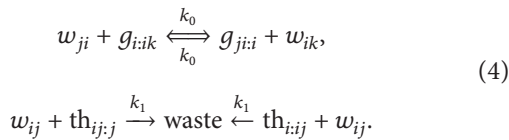
Thresholding reactions:



Reporting reactions:



These chemical reactions modelling the toehold exchange steps and threshold absorption steps can be written uniformly. For all $i, j, k \in \{1, 2, \dots, N\}$, where the variables refer to the molecular species,



Using standard mass action chemical kinetics, it gives rise to a system of ordinary differential equations (ODEs) for the dynamics. In the following, w_{ij} and similar terms refer to the concentration of the respective species, rather than to the species themselves:

$$\begin{aligned} \frac{dw_{ij}}{dt} &= k_0 \left(\sum_{n=1}^N w_{ni} \cdot g_{i:ij} + w_{jn} \cdot g_{ij:j} \right. \\ &\quad \left. - w_{ij} \cdot g_{ni:i} - w_{ij} \cdot g_{j:jn} \right), \\ \frac{dg_{i:ij}}{dt} &= k_0 \left(\sum_{n=1}^N w_{ij} \cdot g_{ni:i} - w_{ni} \cdot g_{i:ij} \right), \end{aligned}$$

$$\frac{dg_{ij:j}}{dt} = k_0 \left(\sum_{n=1}^N w_{ij} \cdot g_{j:jn} - w_{jn} \cdot g_{ij:j} \right),$$

$$\frac{dth_{i:ij}}{dt} = -k_1 \cdot w_{ij} \cdot th_{i:ij},$$

$$\frac{dth_{ij:j}}{dt} = -k_1 \cdot w_{ij} \cdot th_{ij:j}. \quad (5)$$

These dynamics have conserved quantities for each gate node i and for each signal wire ij :

$$\begin{aligned} \sum_{n=1}^N g_{ni:i} + g_{i:in} &\equiv c_i, \\ g_{i:ij} - th_{i:ij} + w_{ij} + g_{ij:j} - th_{ij:j} &\equiv c_{ij}, \\ \frac{dc_i}{dt} = \frac{dc_{ij}}{dt} &= 0. \end{aligned} \quad (6)$$

With these dynamic equations above, simulations have been performed masterly by Mathematic in a PC platform (Windows OS, I3 processor, 2 G RAM).

3. Molecular Adders Based on the Concept of Seesaw Gate

In electronics, an adder is a digital circuit that performs addition of numbers. In many computers and other types of processors, adders are used not only in arithmetic logic units, but also in other parts of the processor, where they are used to calculate addresses, table indices, and similar operations. In this section, we propose full adder and serial binary adder, with the concept described above, which is based on toehold-mediated DNA strand displacement.

3.1. Molecular Full Adder. A full adder adds binary numbers and accounts for values carried in and out. A single-bit full adder adds three single-bit numbers, often written as A , B , and C_0 ; A and B are the operands, and C_0 is a bit carried in from the next less significant stage. The full adder is usually a component in a cascade of adders which add 8-, 16-, and 32-bit binary numbers, and so on. The circuit produces a two-bit output, namely, output carry and sum, which are typically represented by the signals C_1 and S . The logic expression of the full adder is shown below:

$$\begin{aligned} S &= A \oplus B \oplus C_0, \\ C_1 &= A \cdot B + C_0 \cdot (A \oplus B). \end{aligned} \quad (7)$$

Add a file containing a digital circuit netlist, which can translate into an equivalent dual-rail circuit, in which each input is replaced by a pair of inputs, representing logic ON and OFF separately. The equivalent seesaw circuit of the full adder is shown in Figure 2, in which numbers ahead of or at the top of nodes indicate identities of nodes (or interfaces to

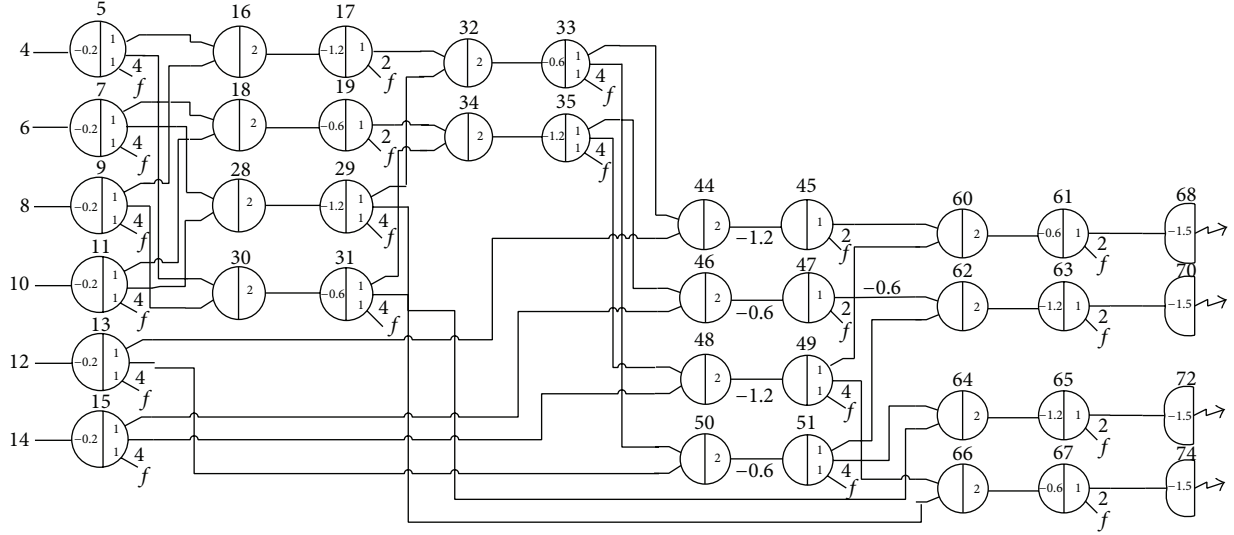
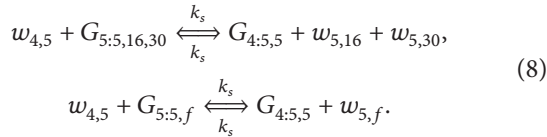


FIGURE 2: The seesaw circuit of the full adder.

those nodes in a network) and numbers within the nodes or on the wires indicate relative concentration of different initial DNA species. The seesaw circuit consists of 38 seesaw gates, any one of which is equivalent to the seesaw gate described in Figure 1. For example, the top left gate (gate:output $G_{5:5,16,30}$) is a general seesaw gate, whose input is $w_{4,5}$, threshold is $\text{Th}_{4,5:5}$, outputs are $w_{5,16}$ and $w_{5,30}$, and fuel is $w_{5,f}$. The seesaw reactions of gate 5 (namely, $G_{5:5,16,30}$) are described after Figure 2.

Seesawing reactions of gate 5:



Thresholding reactions of gate 5:



All of the other 37 gates are just like gate 5, are general seesaw gates, and can be similarly translated into corresponding seesaw reactions. Introduced in Section 2, all these seesaw reactions can be translated into equivalent dynamic equations, which can be simulated by mathematic in a PC platform.

Simulations are performed with the reference concentration $1x = 30 \text{ nM}$. The simulation result is shown in Figure 3, the horizontal axis represents the reaction time (from 0 h to 10 h), and the vertical axis represents the relative output concentration (from $0x$ to $10x$). Moreover, the red curve describes the slope of the sum ($S = 0$) over time, the green curve describes the slope of the sum ($S = 1$) over time, the blue curve describes the slope of carry-over ($C = 0$) over time, and the yellow curve describes the slope of carry-over ($C = 1$) over time. When the reaction is almost completed, only one of the red and green curves (similarly blue and yellow) must stay at the high concentration ($\geq 0.8x$), and the other must

stay at the low concentration ($\leq 0.2x$). This guarantees that only one result of $S = 1$ and $S = 0$ (similarly $C = 1$ and $C = 0$) can stay true, which is also reasonable in the real world. Any other condition is regarded as an exception. Finally, the high concentration curves represent the final true result. For example, if input signals A , B , and C_0 all stay OFF (i.e., between $0x$ and $0.1x$), as shown in Figure 3(a), the final high concentration curves are $S = 0$ and $C_1 = 0$, which is the true result, which means that the computing result is (sum = 0, carry = 0). The whole value table of full adder is shown in Table 1. It can be found that all the conditions go cohere with the theoretical value.

3.2. Molecular Serial Binary Adder. The serial binary adder is a digital circuit that performs binary addition bit by bit. It has two two-bit inputs for the numbers to be added (A_2A_1 , B_2B_1) and a single-bit input for the carry-in (C_0). The outputs are a two-bit output for the sum (S_2S_1) and single-bit output for carry-out (C_2). First A_1 , B_1 , and C_0 are added together to produce the low-bit sum (S_1) and low-bit carry-out (C_1). The high-bit carry-in signal is the previously calculated low-bit carry-out signal, so A_2 , B_2 , and C_1 are added together to produce the high-bit sum (S_2) and high-bit carry-out (C_2). Addition is performed by adding each bit from lowest to highest, one per clock cycle. The logic expression of the serial binary adder is shown below:

$$\begin{aligned} S_1 &= A_1 \oplus B_1 \oplus C_0, \\ C_1 &= A_1 * B_1 + (A_1 + B_1) * C_0, \\ S_2 &= A_2 \oplus B_2 \oplus C_1, \\ C_2 &= A_2 * B_2 + (A_2 + B_2) * C_1. \end{aligned} \quad (10)$$

In this paper, we use two full adders to achieve the serial binary adder, in which the carry-over of the first full adder is regarded as the input of the second full adder. Unfortunately, an exception occurs unexpectedly during simulation. As shown in Figure 4, when the input is (0, 0, 0, 0, 0),

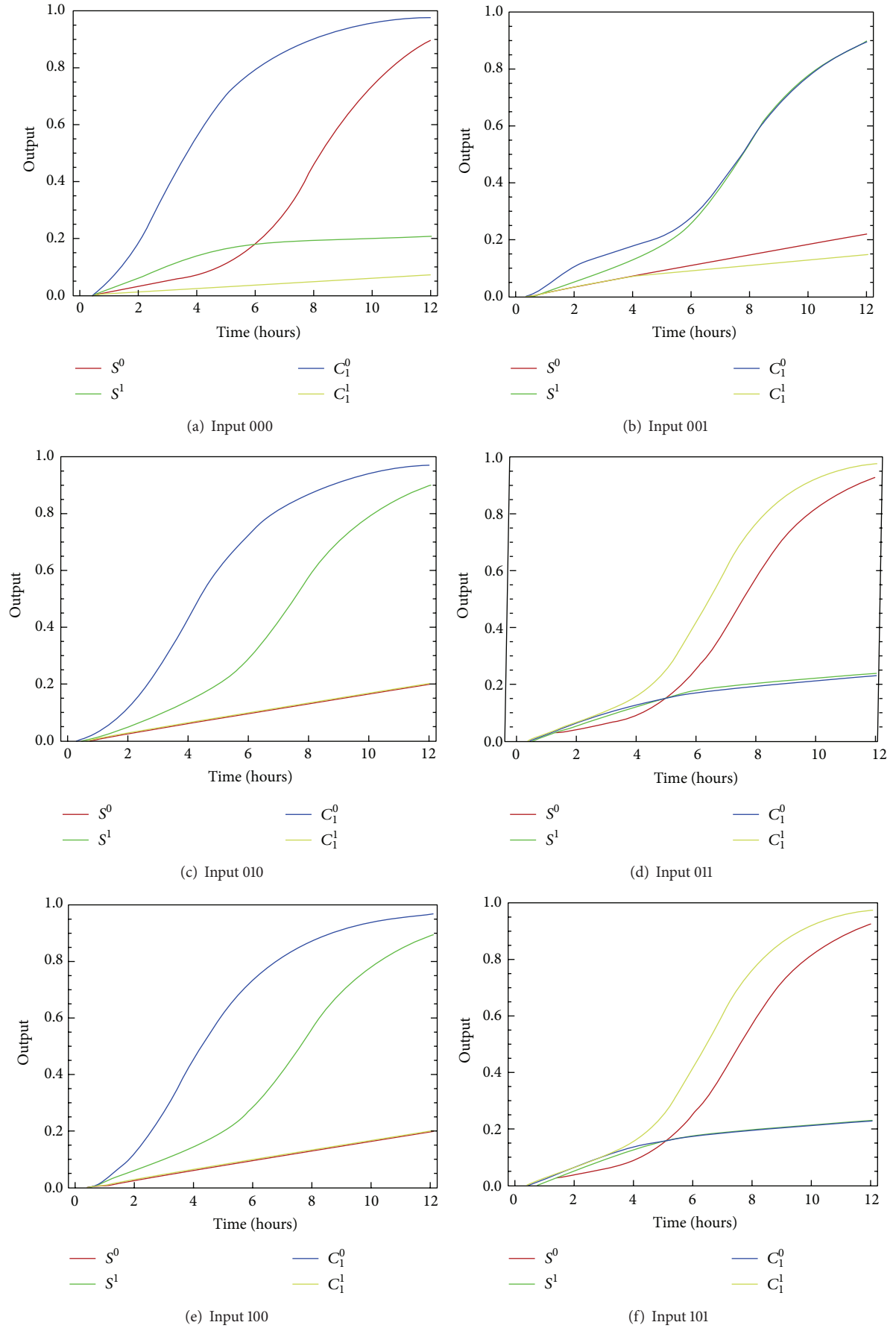


FIGURE 3: Continued.

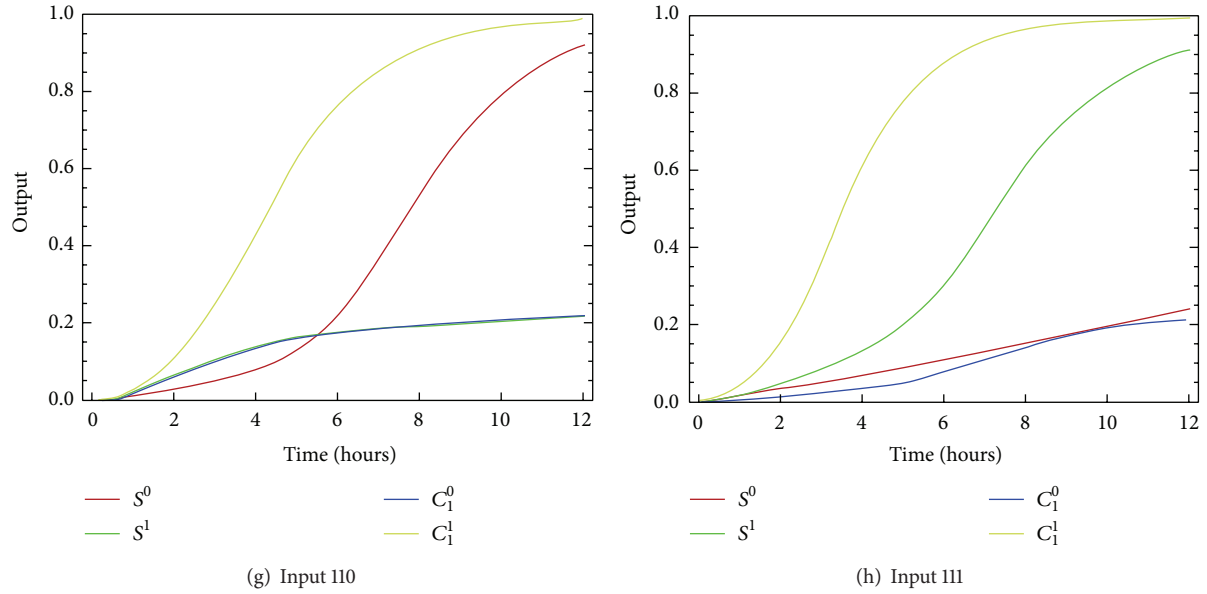


FIGURE 3: The simulation result of the full adder.

TABLE 1: The value table of the half adder seesaw circuit.

Inputs	$S = 0$	$S = 1$	$C_1 = 0$	$C_1 = 1$	Computing results
(A = OFF, B = OFF, C_0 = OFF)	1	0	0	1	$S = 0, C_1 = 1$
(A = OFF, B = OFF, C_0 = ON)	0	1	1	0	$S = 1, C_1 = 0$
(A = OFF, B = ON, C_0 = OFF)	0	1	1	0	$S = 1, C_1 = 0$
(A = OFF, B = ON, C_0 = ON)	1	0	0	1	$S = 0, C_1 = 1$
(A = ON, B = OFF, C_0 = OFF)	0	1	1	0	$S = 1, C_1 = 0$
(A = ON, B = OFF, C_0 = ON)	1	0	0	1	$S = 0, C_1 = 1$
(A = ON, B = ON, C_0 = OFF)	1	0	0	1	$S = 0, C_1 = 1$
(A = ON, B = ON, C_0 = ON)	0	1	0	1	$S = 1, C_1 = 1$

the concentrations of $S_1 = 1$ and $S_1 = 0$ (similarly $S_2 = 1$ and $S_2 = 0$) are both over 0.5, indicating that both $S_1 = 1$ and $S_1 = 0$ (similarly $S_2 = 1$ and $S_2 = 0$) are true results, which are contrary to the reality. However, at this point, the final values of $S_1 = 1$ and $S_1 = 0$ (similarly $S_2 = 1$ and $S_2 = 0$) still can be distinguished, which have not been the worst offenders. However, when the input is (1, 1, 1, 1, 1), the concentrations of $S_1 = 1$ and $S_1 = 0$ (similarly $S_2 = 1$ and $S_2 = 0$) ascend nearly at the same height (which are both over 0.9), such that we are unable to distinguish the “low concentration” and “high concentration,” which is a very serious exception. In the next part, we will analyze the reason for this situation and propose a method to solve it.

4. A Debugging Method for Molecular Circuit

As of this writing, many well-worked molecular computing devices, including logic gates, circuits, and tiny circuit boards, exist. However, an effective debugging method for molecular circuit is still needed. In the molecular circuit, exceptions always occur unexpectedly because of the tiny differences in temperature, concentration, reaction duration, and other factors. Thus, proposing a method to debug the molecular

circuits is of great importance to the development of molecular computing. In this paper, we propose a method to address this issue.

The main idea is to add fan-outs to the seesaw circuit. Fan-outs are molecular fluorescent signals that can monitor the target molecule (any possible abnormal molecule). The real-time concentration of the target molecule can be obtained, which can help us analyze the circuit exception. If the site of the exception is unknown, debugging can be implemented from the output end step by step, until the exception molecular is discovered. The results in Figure 6 indicate that the new fluorescent signal nearly does not influence the initial molecular circuit, which means that our debugging does not change the original circuit. In the following section, some examples are shown to explain the process and manipulation of this method, as well as to prove the practicability and validity of the method.

4.1. Debugging of the XOR Circuit. Exclusive or XOR is a logical operation that outputs truly whenever both inputs differ (one is true, and the other is false). The opposite of XOR is logical biconditional, which outputs truly whenever both

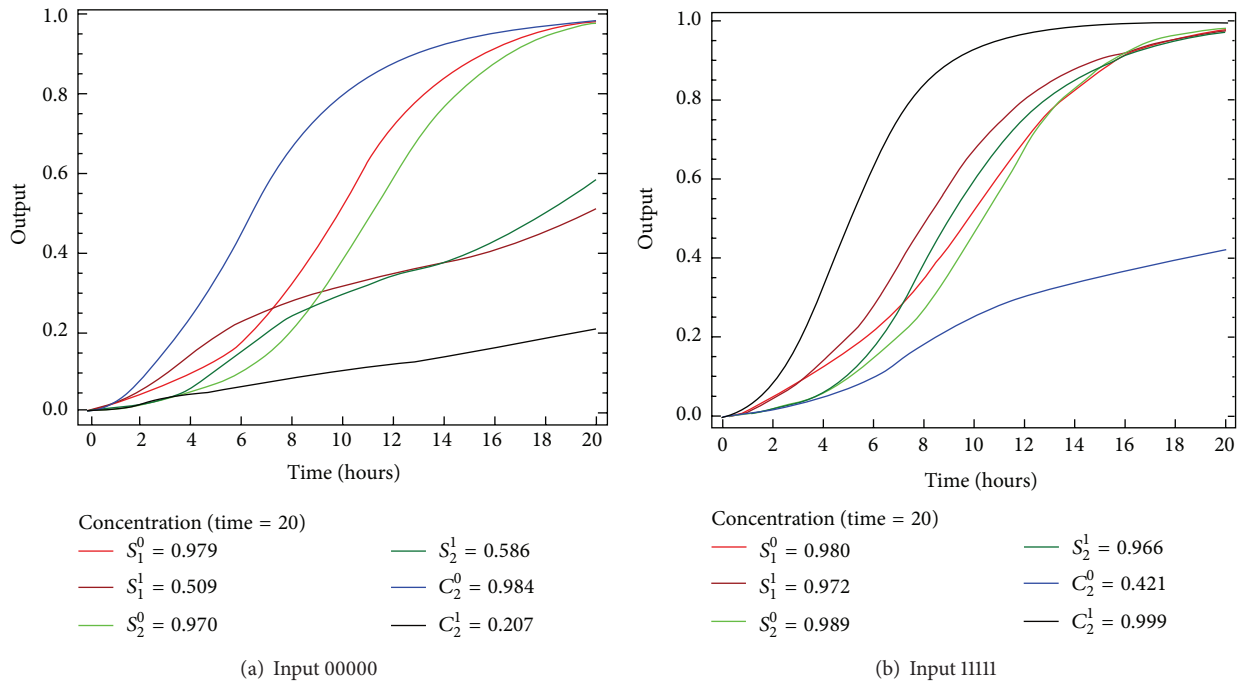


FIGURE 4: The simulation result of the serial binary adder.

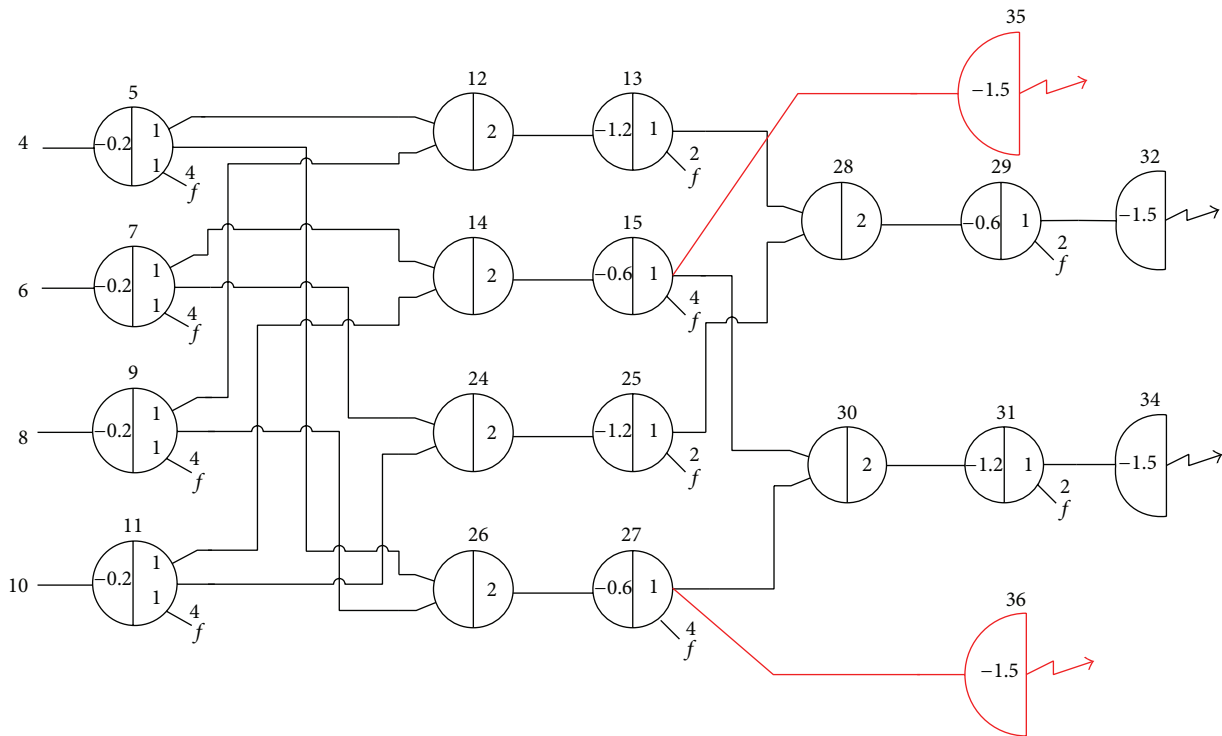


FIGURE 5: The seesaw circuit of the XOR circuit with monitoring molecular.

inputs are the same. It gains the name “exclusive or” because the meaning of “or” is ambiguous when both operands are true; “exclusive or” excludes that case. XOR is sometimes thought of as one or the other but not both. The XOR circuit is a simple circuit that is used to obtain the monitoring results, so we first choose the XOR circuit for analysis. Two inputs (A

and B) and an output (S) exist in the XOR circuit. The logic expression of the XOR circuit is shown below:

$$S = A \oplus B = A \cdot B' + A' \cdot B. \quad (11)$$

To debug the XOR circuit, as shown in Figure 5, we add two fluorescent signals (35 and 36) for monitoring the target

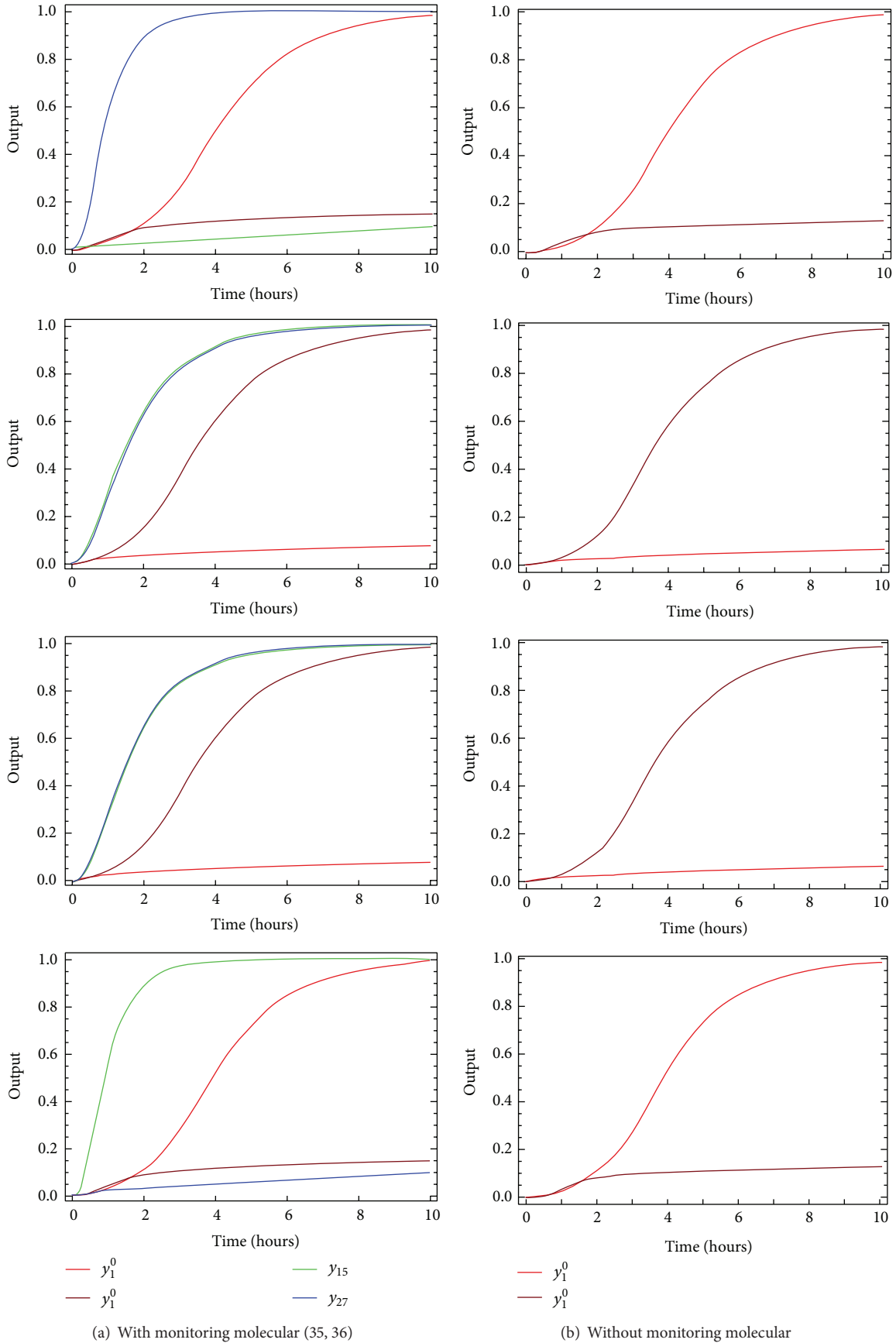


FIGURE 6: The simulation result of the XOR circuit.

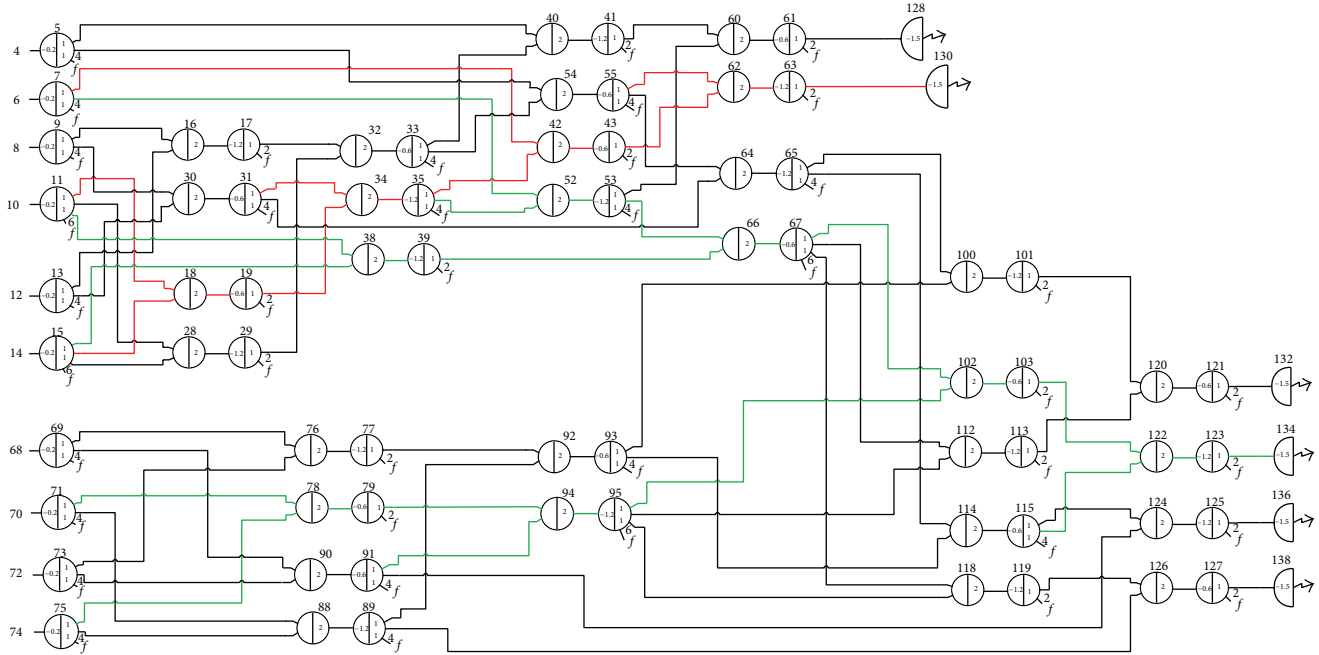


FIGURE 7: The error line of the serial binary adder circuit.

TABLE 2: The contrast between the simulation result of with monitoring and without monitoring.

Input	Monitor	$T = 2$	$T = 4$	$T = 6$	$T = 8$
(0, 0)	yes/no	0.033/0.029	0.046/0.041	0.055/0.050	0.064/0.059
(0, 1)	yes/no	0.106/0.102	0.497/0.506	0.825/0.833	0.943/0.947
(1, 0)	yes/no	0.033/0.029	0.046/0.041	0.055/0.050	0.064/0.059
(1, 1)	yes/no	0.112/0.107	0.525/0.534	0.853/0.853	0.952/0.956

molecule directly before the output signal, which is the direct input of the final output, which will directly influence the final result. Four fluorescent signals exist in the circuit. The original fluorescent signals (32, 34) monitor the real output. The added fluorescent signals (35, 36) monitor the temporary output, wherein an exception may occur. Other parts of the circuit remain unchanged.

The simulation result is shown in Figure 6. The changed circuit results with monitoring molecule are shown in Figure 6(a), whereas the original circuit results without monitoring molecule are shown in Figure 6(b). Table 2 shows the actual simulation results of the two cases, from which we can find the contrast between the simulation result of with monitoring molecule and without monitoring molecule and that the average of the difference between the two cases equals 0.004, which proves that the output almost remains unchanged and the debugging method does not influence the initial molecular circuit. Furthermore, the output of the monitoring molecule is consistent with the theoretical value and proves that circuit functions properly at the monitoring point.

4.2. Debugging of the Serial Binary Adder Circuit. In the aforementioned section, we pointed out that the serial binary

adder does not function properly. An exception occurs when the input is (1, 1, 1, 1) and concentrations of $S_1 = 1$ and $S_1 = 0$ (similarly $S_2 = 1$ and $S_2 = 0$) are both over 0.9. Thus, both $S_1 = 1$ and $S_1 = 0$ (similarly $S_2 = 1$ and $S_2 = 0$) are true results. Actually, the concentration of $S_1 = 1$ and $S_2 = 1$ should be low, with a final value that does not exceed 0.2. Therefore, an exception must occur somewhere. To determine where the exception occurs, we debug the circuit with the above method in a reverse stepwise manner.

We analyze the exception of $S_1 = 1$. The concentration of $S_1 = 1$ is obtained from fluorescent signal 130 (Figure 7), which represents the output of AND (62, 63). The direct input of AND (62, 63) is the first target molecule to monitor, which are molecules 43 and 55, so we add two fluorescent signals to monitor molecules 43 and 55. The monitoring result is shown in Figure 8(a), showing that molecule 55 functions well, but molecule 43 indicates an exception, which should be a low concentration in theory. We then monitor the direct input of molecule 43, which are molecules 7 and 35. The monitoring results are shown in Figure 8(b), in which both molecules indicate an emerging exception. Subsequently, we monitor the direct input of molecule 35, which are molecules 19 and 31, and the monitoring results are shown in Figure 8(c), which shows that molecule 19 indicates an exception. We then

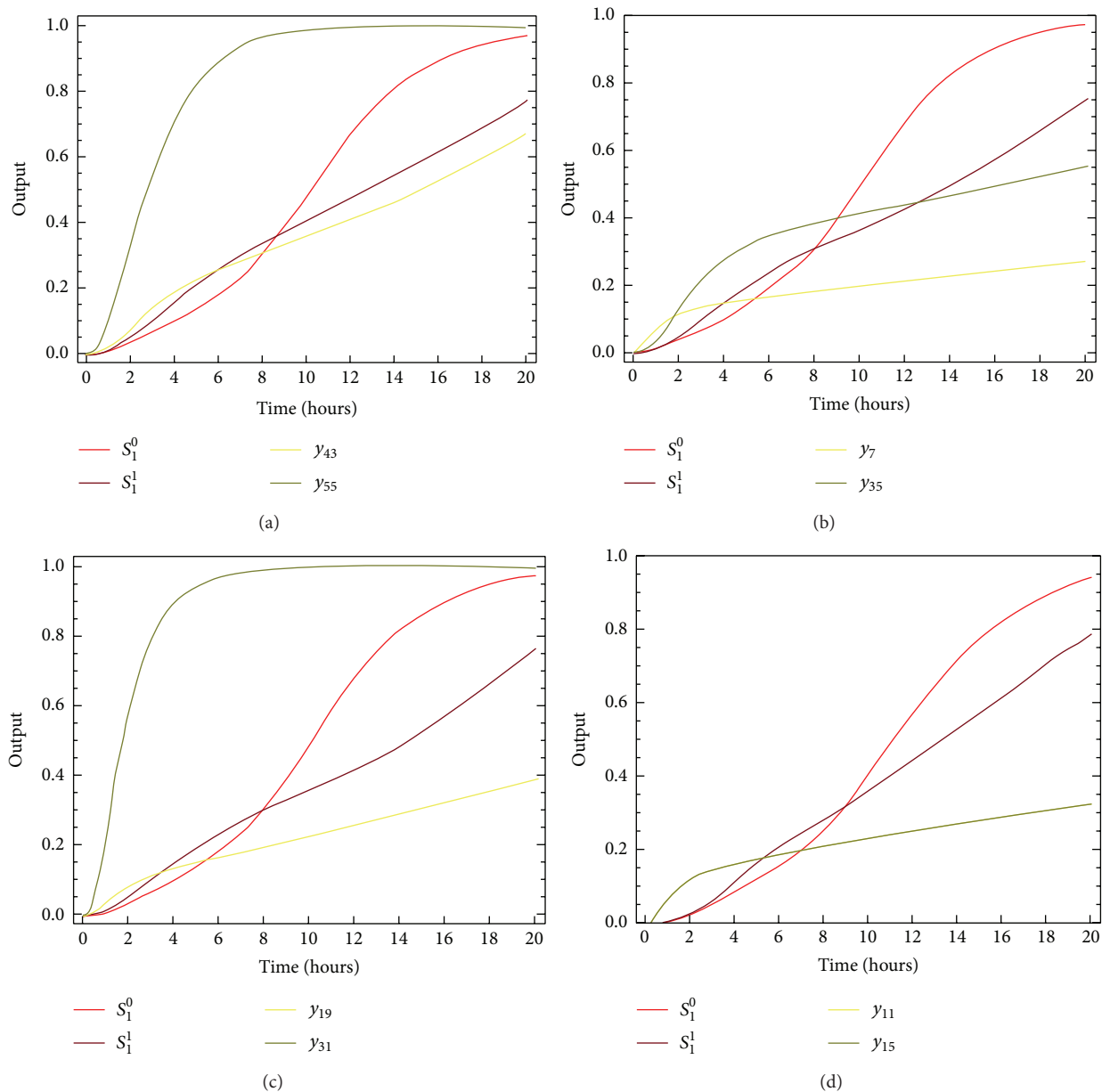


FIGURE 8: The simulation result of the serial binary adder circuit.

monitor the direct input of molecule 19, which are molecules 11 and 15. The monitoring results are shown in Figure 8(d); both molecules demonstrate an exception, which is also the point where exception occurs first. Thus, the exception point is found. The error transmission line described above is shown in Figure 7 (red line). The other error line of $S_2 = 1$ can be obtained in the same way, which is shown in Figure 7 (green line).

5. Conclusions and Future Work

In this paper, we construct several adders with a simple DNA gate motif, namely, the seesaw gate. The seesaw gate is a single DNA strand that can bind to signal strands via

toehold domain. In the initial state, the input signals with a high concentration will react with the compound molecule in which the output signals are bound. The fundamental operation is toehold exchange, which is a toehold-mediated strand displacement reaction that results in a free right-side signal strand replacing a bound left-side signal strand. Typically, circuits with any arbitrarily complex can be constructed via cascading the simple gates. We build some adders with the above concept, including half adder, full adder, and serial binary adder. The validity and correctness of the half adder and full adder are demonstrated by simulation experiment.

During the simulation of the serial binary adder, an exception occurs, which leads to the incorrectness of the output. We find that the fan-out of the seesaw gate can

influence the output, which is bordered by the threshold. When the output is with high concentration, more fan-outs lead to lower concentration of the output; when the output is with low concentration, more fan-outs lead to higher concentration of the output. In the case of the serial binary adder, the fan-outs number has reached upper limit, and the output with low concentration is higher than that under normal conditions, thereby leading to the exception.

To solve this problem, we propose a method to debug the molecular circuit. The main idea is to add fan-outs to the seesaw circuit, which is a molecular fluorescent signal. With the fluorescent molecule, we can obtain the output of any gate. Thus, the debugging process can be implemented in a stepwise manner, similar to the occasion of the serial binary adder circuit above.

For future studies, two directions can be considered. First, we should design an adaptive debugging method, which is a self-correcting mechanism that can adjust the parameters (e.g., concentration and threshold) aimed at different circuits automatically. Second, to solve the abnormal occasion, we should study the signal reconstruction mechanism for recovery of the distorted signal, which can help deal with the output exception of the serial binary adder circuit. Moreover, with the signal reconstruction mechanism, more large-scale circuits are more likely to be implemented.

Conflict of Interests

The authors declare that there is no conflict of interests regarding the publication of this paper.

Acknowledgments

The work is supported by National Natural Science Foundation of China (Grants nos. 61472333, 61370010, 51405408, and 71103154), Natural Science Foundation of Fujian Province of China (nos. 2011J01334, 2014J01253), Ph.D. Programs Foundation of Ministry of Education of China (20120121120039), and China Scholarship Council (201308350065).

References

- [1] S. Coe, W.-K. Woo, M. Bawendi, and V. Bulović, "Electroluminescence from single monolayers of nanocrystals in molecular organic devices," *Nature*, vol. 420, no. 6917, pp. 800–803, 2002.
- [2] S. Dydel and P. Bała, "Large scale protein sequence alignment using FPGA reprogrammable logic devices," in *Field Programmable Logic and Application*, vol. 3203 of *Lecture Notes in Computer Science*, pp. 23–32, Springer, Berlin, Germany, 2004.
- [3] H. Komatsu, S. Matsumoto, S.-I. Tamaru, K. Kaneko, M. Ikeda, and I. Hamachi, "Supramolecular hydrogel exhibiting four basic logic gate functions to fine-tune substance release," *Journal of the American Chemical Society*, vol. 131, no. 15, pp. 5580–5585, 2009.
- [4] G. Seelig, D. Soloveichik, D. Y. Zhang, and E. Winfree, "Enzyme-free nucleic acid logic circuits," *Science*, vol. 314, no. 5805, pp. 1585–1588, 2006.
- [5] D. R. Stewart, D. A. A. Ohlberg, P. A. Beck et al., "Molecule-independent electrical switching in Pt/organic monolayer/Ti devices," *Nano Letters*, vol. 4, no. 1, pp. 133–136, 2004.
- [6] Y. Benenson, R. Adart, T. Paz-Elizur, Z. Livneh, and E. Shapiro, "DNA molecule provides a computing machine with both data and fuel," *Proceedings of the National Academy of Sciences of the United States of America*, vol. 100, no. 5, pp. 2191–2196, 2003.
- [7] Y. Benenson, T. Paz-Elizur, R. Adar, E. Keinan, Z. Livneh, and E. Shapiro, "Programmable and autonomous computing machine made of biomolecules," *Nature*, vol. 414, no. 6862, pp. 430–434, 2001.
- [8] W. He, X. Ma, X. Yang, Y. Zhao, J. Qiu, and H. Hang, "A role for the arginine methylation of Rad9 in checkpoint control and cellular sensitivity to DNA damage," *Nucleic Acids Research*, vol. 39, no. 11, pp. 4719–4727, 2011.
- [9] C. Mao, T. H. LaBean, J. H. Reif, and N. C. Seeman, "Logical computation using algorithmic self-assembly of DNA triple-crossover molecules," *Nature*, vol. 407, no. 6803, pp. 493–496, 2000.
- [10] J. Yang, C. Dong, Y. Dong, S. Liu, L. Pan, and C. Zhang, "Logic nanoparticle beacon triggered by the binding-induced effect of multiple inputs," *ACS Applied Materials & Interfaces*, vol. 6, no. 16, pp. 14486–14492, 2014.
- [11] C. Zhang, J. Ma, J. Yang, H. Inaki Schlaberg, S. Liu, and J. Xu, "Nanoparticle aggregation logic computing controlled by DNA branch migration," *Applied Physics Letters*, vol. 103, no. 9, Article ID 093106, 2013.
- [12] C. Zhang, L. Ma, Y. Dong, J. Yang, and J. Xu, "Molecular logic computing model based on DNA self-assembly strand branch migration," *Chinese Science Bulletin*, vol. 58, no. 1, pp. 32–38, 2013.
- [13] M. N. Stojanovic and D. Stefanovic, "A deoxyribozyme-based molecular automaton," *Nature Biotechnology*, vol. 21, no. 9, pp. 1069–1074, 2003.
- [14] J. Wang and R. Huang, "Design and implementation of a microfluidic half adder chip based on double-stranded DNA," *IEEE Transactions on Nanobioscience*, vol. 13, no. 2, pp. 146–151, 2014.
- [15] L. Qian and E. Winfree, "A simple DNA gate motif for synthesizing large-scale circuits," in *DNA Computing*, vol. 5347 of *Lecture Notes in Computer Science*, pp. 70–89, Springer, Berlin, Germany, 2009.
- [16] Q. Zou, Y. Mao, L. Hu, Y. Wu, and Z. Ji, "miRClassify: an advanced web server for miRNA family classification and annotation," *Computers in Biology and Medicine*, vol. 45, no. 1, pp. 157–160, 2014.
- [17] L. Qian and E. Winfree, "Scaling up digital circuit computation with DNA strand displacement cascades," *Science*, vol. 332, no. 6034, pp. 1196–1201, 2011.
- [18] L. Qian, E. Winfree, and J. Bruck, "Neural network computation with DNA strand displacement cascades," *Nature*, vol. 475, no. 7356, pp. 368–372, 2011.
- [19] D. Y. Zhang, A. J. Turberfield, B. Yurke, and E. Winfree, "Engineering entropy-driven reactions and networks catalyzed by DNA," *Science*, vol. 318, no. 5853, pp. 1121–1125, 2007.

Research Article

FRET-Based Detection of Enzymatic Reaction of Botulinum on Microfluidic Device

Young Min Bae, Seung Oh Jin, Insoo Kim, and Ki Young Shin

Korea Electrotechnology Research Institute, 111 Hangeulro, Ansan 426-910, Republic of Korea

Correspondence should be addressed to Young Min Bae; kimbym@keri.re.kr

Received 22 April 2015; Revised 3 July 2015; Accepted 16 July 2015

Academic Editor: Zhida Xu

Copyright © 2015 Young Min Bae et al. This is an open access article distributed under the Creative Commons Attribution License, which permits unrestricted use, distribution, and reproduction in any medium, provided the original work is properly cited.

A microfluidic device was implemented to detect the enzymatic reaction of botulinum toxin A (BTA) using Förster resonance energy transfer (FRET). The microfluidic device comprised a main channel having two loading zones, a reaction chamber and a side channel perpendicular to the main channel. The reaction chamber defined by weir in the main channel was packed with microbeads. The movement of the peptide substrate and the BTA in the microfluidic device was controlled by electrophoresis, and the enzymatic reaction of the BTA was detected through the changes of the fluorescence intensity in the reaction chamber. As a result, it was observed that the enzymatic reaction was affected by the electric voltage applied for the movement of the BTA and the peptide and improved by packing the microbeads in the reaction chamber. The microfluidic device provides the tool to investigate the proteolysis of the substrate by the BTA.

1. Introduction

Microfluidics technology that deals with the behavior, precise control, and manipulation of tiny volume of fluids in microliter scale has been used to execute various biological protocols to detect specific biomaterials [1]. By scaling down conventional biological protocols executed in laboratories into chip-based analyses, the microfluidics provides advantages as follows: (1) a tiny sample volume is required, (2) an analysis time is reduced, (3) experimental procedures are automated, and (4) high-throughput system (HTS) can be implemented [2, 3]. For example, the antigen-antibody binding for immunoassay and the catalytic reaction of enzymes were executed in microfluidic devices [4, 5].

Botulism, which is a rare but serious paralytic illness, is caused by botulinum toxins (BTs) that are produced by a bacterium, *Clostridium botulinum* (*C. botulinum*) [6]. There are three main kinds of botulism, of which food-borne botulism is caused by eating foods that contain the botulinum toxin. As *C. botulinum* can survive the boiling temperature of water at sea level, it is hard to remove its toxicity. The toxicity of BTs is due to their enzymatic function. The BTs, of which there are seven serologically distinct types, are composed of two peptide sequences—a heavy chain and

a light chain [7]. The heavy chain is particularly important for targeting the toxin to specific types of axon terminals, and the light chain is the proteolytic enzyme that cleaves the specific peptide sequence of neuronal proteins inside the axon terminal, which blocks the releases of acetylcholine in a neuronal system [8]. As the BTs, of which the median lethal dose LD50 is around 1–10 ng/kg, are fatal to humans, they are considered as a candidate for biological weapons [9]. Indeed, the methods for detecting the enzymatic reaction of BTs have been implemented using the technique such as Förster resonance energy transfer (FRET) [10, 11].

In this study, we proposed the structure of microfluidic device to implement the FRET reaction and demonstrated the feasibility of it to detect the enzymatic reaction of botulinum toxin A (BTA). It is unique that the device is designed to execute the enzymatic reaction of the BTA and detect a fluorescence signal due to the FRET technique. The detailed scheme of the FRET technique based on the enzymatic reaction is represented by Figure 1. In the “before reaction” state, there is the peptide substrate that can be specifically cleaved by BT. Fluorescein isothiocyanate (FITC) as a donor and 4,4-dimethylaminoazobenzene-4'-carboxylic acid (DABCYL) as an acceptor are chemically attached in both ends of peptide substrate, respectively. In the “before reaction” state, when

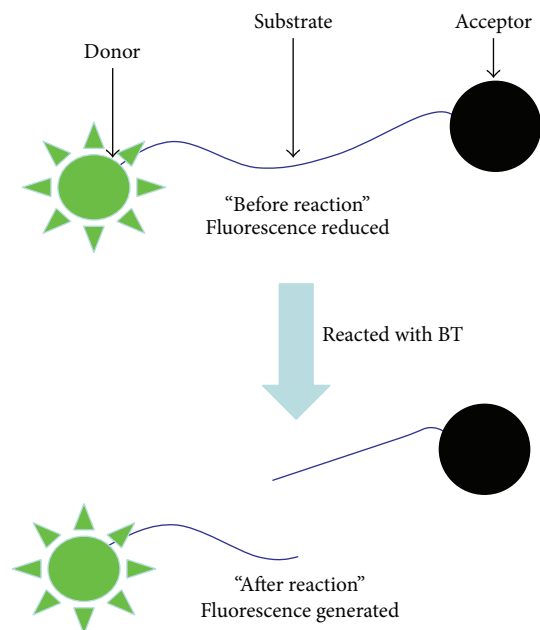


FIGURE 1: FRET-based detection of the proteolytic reaction of the BTA using FRET.

the light with specific wavelength for exciting the donor is irradiated, the emitted photon is absorbed by the acceptor, which results in reducing fluorescence of the donor. However, after the specific sequence of peptide is cleaved by BTs (the "after reaction" state in Figure 1), the photon due to the emission of donor is not absorbed by the acceptor. Here, the enzymatic reaction of the BTA was executed in the microfluidic device fabricated with PDMS (polydimethylsiloxane), and the fluorescence due to the emission from the donor was observed using a fluorescence microscope. Finally, the applicability of the microfluidic device to detect the enzymatic reaction of BTA was investigated.

2. Materials and Methods

2.1. Materials. PDMS prepolymer (Sylgard 184) was purchased from Dow Corning company, and polystyrene microbeads having a nominal diameter of $9.77\ \mu\text{m}$ were purchased from Bangs Laboratories.

A light chain of BTA and a substrate having a peptide sequence cleaved by the light chain of BTA were purchased from List Biological Laboratories, Inc. The peptide sequence of substrate is TRDIDQANQRTTK (T, threonine; R, arginine; I, isoleucine; D, aspartic acid; A, alanine; N, asparagine; Q, glutamine; and K, lysine) [12]. The substrate has FITC as a donor and DABCYL as an acceptor bound chemically in both ends of it. All other chemicals were purchased from Sigma-Aldrich company.

All aqueous solution was prepared using $18\ \text{M}\Omega\text{-cm}$ water. A $0.01\ \text{M}$ phosphate-buffered saline (PBS, pH 7.4) solution containing $138\ \text{mM}$ NaCl, $2.7\ \text{mM}$ KCl, $8.1\ \text{mM}$ Na_2HPO_4 , $1.47\ \text{mM}$ KH_2PO_4 , and 0.05% Tween 20 was used in all experiments.

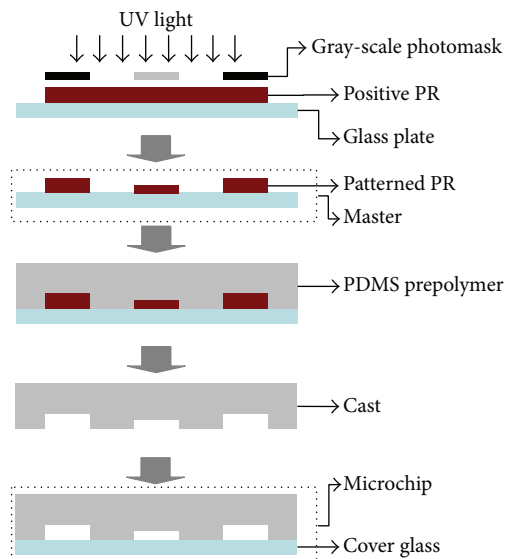


FIGURE 2: Fabrication of microfluidic device using photolithography and PDMS molding technique.

2.2. Fabrication of Microfluidic Device. The microfluidic device was fabricated using the PDMS molding method described elsewhere (Figure 2) [13, 14]. The positive photoresistive (PR) film (AZ P4620, Clariant Co.) deposited on a glass plate was patterned by gray-scale photolithography [15]. A photographic film (Kodak Precision Line Film LPD4) was used as a gray-scale photomask for the photolithographic process. In order to prepare the photomask, after the microchannel pattern was drawn using the commercial software (CorelDraw 9, Corel Corporation, USA), it was printed onto a high-quality, glossy paper with a dye-sublimation printer. Then, the printed design was photoreduced by a factor of 10 onto the photographic film. The glass plate with the PR film patterned was used as the master.

To fabricate the microfluidic device, a 10 : 1 mixture of the PDMS prepolymer and the curing agent was poured onto the master and then cured at 60°C for at least 2 hours. After being separated from the master, the cast (the cured PDMS) and a clean microscopy glass were treated with an oxygen plasma (60 W, model PDC-32G, Harrick Scientific, Ossining, NY) for 30 sec. After that, immediately, the device was completed by irreversibly sealing the cast with the microscopy glass. After being sealed, the microchannel was filled with deionized water to keep the inner surface hydrophilic and stored until needed.

2.3. Experimental Setup. Fluorescence change due to the enzymatic reaction of BT was observed using a fluorescence microscope (Nikon Eclipse TE 300, Nikon Co., Tokyo, Japan) equipped with band-pass filters, a 100 W mercury lamp, and a CCD camera. As the FITC as the donor has the excitation in $488\ \text{nm}$ wavelength and the emission in $523\ \text{nm}$ wavelength, the corresponding filter set was used in the setup of fluorescence microscope.

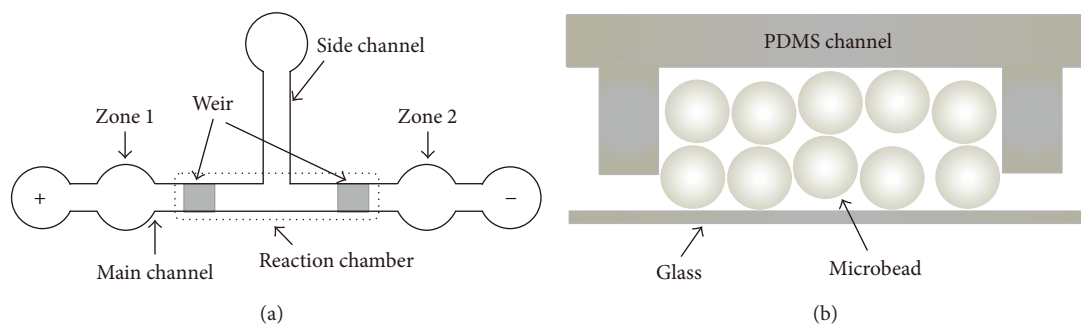


FIGURE 3: Microfluidic device designed for the enzymatic reaction of BT: (a) the layout of microfluidic device (not scaled), (b) a scheme of reaction chamber packed with microbeads (not scaled).

3. Results and Discussion

3.1. Operation of Microfluidic Device. The layout of microfluidic device designed for executing the enzymatic reaction of the BTA was shown in Figure 3(a). The microfluidic device of “T” shape comprises a main channel having two loading zones and a reaction chamber and a side channel perpendicular to it. The length of main channel is 14 mm, and the width of channels is $150\ \mu\text{m}$. Zones 1 and 2 for loading the substrate and the BTA are, respectively, located on both ends of the main channel as shown in Figure 3(a). In addition, two weirs are fabricated in between both loading zones, and the distance between the weirs is 2 mm. A reaction chamber is defined as the part of the main channel between both weirs (Figure 3(b)). The reaction chamber was packed with polystyrene microbeads. The microbeads injected into the microchannel through the side channel are moved into the main channel, and the weirs of the height lower than the diameter of microbeads block the movements of microbeads into the ends of main channel, so the microbeads were packed in the reaction chamber. To prepare the weir in the microchannel, the weir should be thinner than the other area in the microchannel pattern on the master. Conventionally, the type of master with multiple thicknesses is fabricated using a two-step photolithographic process: microchannel patterns are fabricated in the first step, and only parts of weir are exposed and developed in the second step. However, the two-step process is complicated and needs a precise alignment to rightly allocate weirs on microchannel. Here, the process for fabricating the master having the weir structure was simplified by employing gray-scale photolithography (Figure 2). In the gray-scale photolithography, as the intensity of UV light passing through a gray-scale pattern is reduced, the photochemical reaction is controlled on a local area of PR layer [15]. Therefore, the thickness of PR layer exposed to UV light through the gray-scale pattern can be controlled in the developing process. Based on the preliminary experiment on the change of thickness of positive PR layer as a function of a gray level of photomask, the gray level of the weir area was determined to be 50% (the gray levels of 0 and 100% are full transparency and no transparency, resp.). So, the microchannel pattern with the transparencies of 50% only in the weir part and 100% in the other area was used to prepare the gray-scale photomask.

Figures 4(a) and 4(b) show the micrograph of the part of weir in the device fabricated by the PDMS molding technique. The height of microchannels and reaction chamber except for the weir was $21.3 \pm 1\ \mu\text{m}$, which is the same as the thickness of PR layer. The height and length in the part of weir were $5.7 \pm 0.3\ \mu\text{m}$ and $150\ \mu\text{m}$, respectively. Some roughness was observed on the channel surface of the part of weir. This was due to the fact that as the gray-level of photomask was controlled with the density of black microdot, the PR layer was not evenly removed in the developing process. Figures 4(c) and 4(d) show the micrographs of the right and left sides of reaction chamber packed with microbeads. The microbead solution was injected with a syringe through the side channel. During the microbeads injection, they were not observed to pass through the weir.

The operation of the microfluidic device is as follows: (1) the substrate and the BTA are loaded in zones 1 and 2 with micropipettes, respectively, (2) electric potential is applied to both ends of the main channel with the electric direction as shown in Figure 3(a), and (3) a change of fluorescence intensity in the reaction chamber due to the enzymatic reaction of the BTA is observed. The isoelectric point (pI) of the peptide substrate is 9.0 and the pI value of the BTA is 6 [16]. Therefore, under the buffer solution of pH 7.4, the substrate and the toxin are positively and negatively charged, respectively. When the electric field is applied between both ends of the main channel, the substrate moves toward the electric negative side and the BTA moves toward the electric positive side. Both materials are mixed in the reaction chamber packed with the microbeads, followed by the enzymatic reaction of the BTA. Each part of substrates cleaved by the reaction is moved toward the direction determined according to their pI value. The portion of peptide attached to FITC, of which the pI value is 4, moves toward the electric positive side. Therefore, in our experiment, the changes of fluorescence in the end of the reaction chamber close to the electric positive side were observed.

Figures 5(a) and 5(b) show the fluorescence image in the reaction experiment in which the BTA was loaded in zone 2 and in the control experiment in which the BTA was not loaded, respectively. In the reaction experiment, $10\ \mu\text{L}$ of substrate ($20\ \mu\text{M}$) and $10\ \mu\text{L}$ of the BTA ($2\ \mu\text{g}/\text{mL}$) were, respectively, loaded in zone 1 and zone 2, followed by

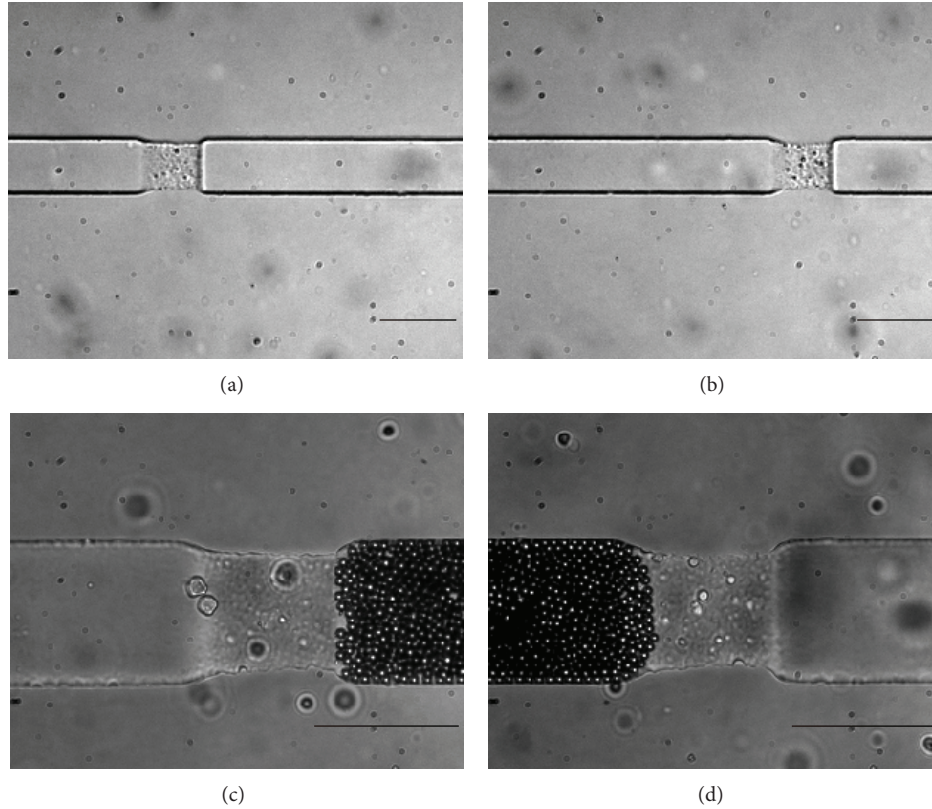


FIGURE 4: Micrograph of the weirs fabricated in the microfluidic device: (a) and (b) show the weir fabricated in the right and left sides of main channel; (c) and (d) show both ends of reaction chamber packed with microbeads. The scale bar in the figures means $100\ \mu\text{m}$.

applying the electric potential of $10\ \text{V}$ to both ends of the main channel as the direction shown in Figure 3(a). In the reaction experiment (Figure 5(a)), the fluorescence intensity in the rectangle area marked with the dotted line became constant in around $5\ \text{min}$. Figure 5(c) shows the profile of fluorescence intensity in the rectangle area marked with the dotted line in Figures 5(a) and 5(b). In both profile curves, the fluorescence intensities due to FITC label attached in the substrate increased in the area of microchannel; however, it was observed that the fluorescence intensity in the reaction experiment was higher than that in the control experiment. The difference of fluorescence meant that the enzymatic reaction was generated in the reaction chamber and the part of substrate with FITC moved toward the electric positive side.

Therefore, the microfluidic device could be applied to detect the enzymatic reaction of BT, and the enzymatic reaction is estimated as the difference between both fluorescence intensities in the reaction and in control experiments.

3.2. Characteristics of Microfluidic Device. The effect of the magnitude of electric field applied to both ends of the main channel was investigated. Figure 6(a) shows the change of fluorescence intensity as a function of the voltage applied. The fluorescence intensity was observed in around $5\ \text{min}$ after the voltage was applied to both sides of the main channel. The enzymatic reaction in the electric field of $5\ \text{V}$ was highest

and the fluorescence intensity decreased with the increasing voltage. In movement of biomaterials charged electrically using electrophoresis, the velocity of charged materials is proportional to the strength of electric field applied with the following equation [16]:

$$v = E \times \mu_e, \quad (1)$$

where μ_e = electrophoretic mobility of particle moved, v = the velocity, and E = electric field strength.

In the experiment, as the substrate and the BTA are, respectively, charged positively and negatively in the buffer solution of pH 7.4, they are transported into the reaction chamber. However, with the increasing voltage, the substrate and the BTA moved too fast to complete the reactions in the reaction chamber, which resulted in the decrease of the enzymatic reaction.

In addition, the effect of microbeads packed in the reaction chamber was investigated. Figure 6(b) shows the average fluorescence intensities of microchannel in both experiments in which the microbeads were packed in the reaction chamber and were not. The electric potential of $5\ \text{V}$ was applied in both experiments. The fluorescence intensities in both experiments were higher than that in the control experiment, which meant that the enzymatic reaction was generated in both experiments. However, the fluorescence intensity in the reaction chamber packed with microbeads was higher than that in the reaction chamber without

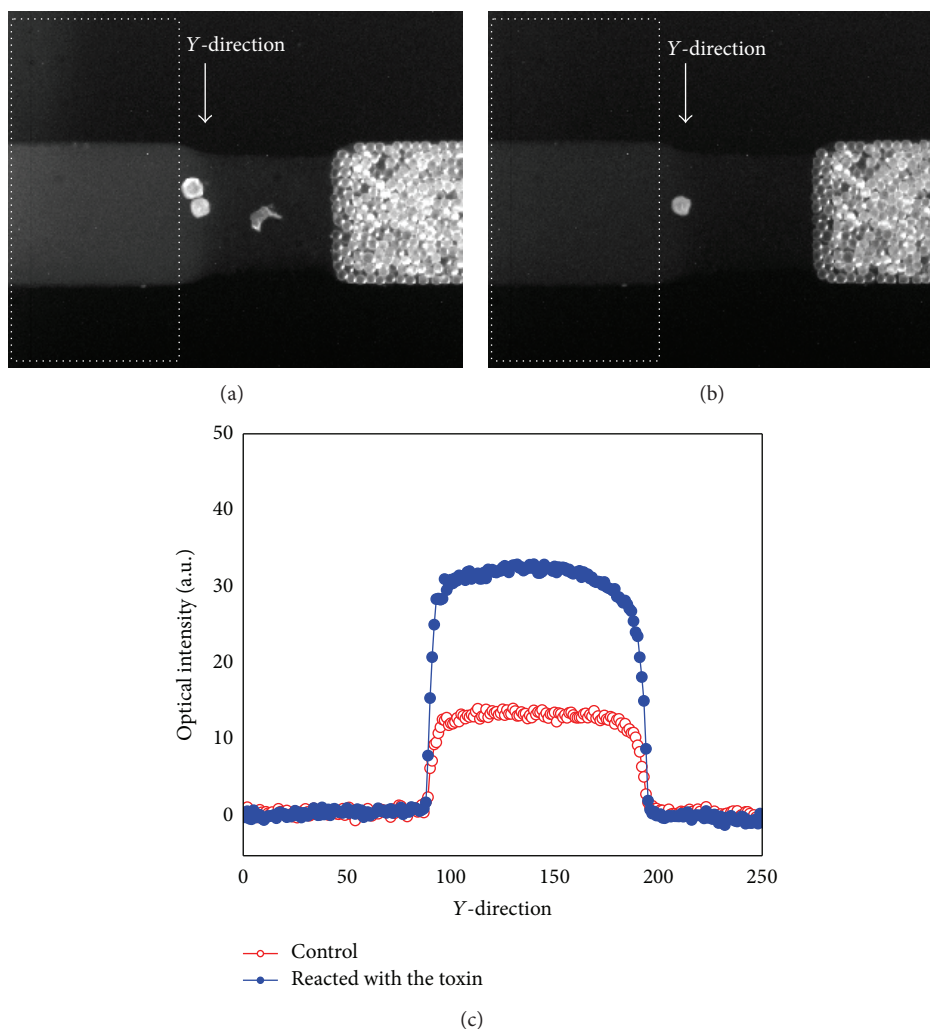


FIGURE 5: Operation of microfluidic device to execute the enzymatic reaction of the BTA according to 10 V application. (a) The fluorescence image of microchannel in the reaction experiment with loading the BTA, (b) the fluorescence image of microchannel in the control experiment without loading the BTA, and (c) the comparison of profiles of fluorescence intensity of both the experiments.

microbeads. Generally, because the Reynolds number of flow is small in microchannel, the turbulent flow is difficult to occur. So, mixing in microchannel is dependent on diffusion of mixtures. For efficient mixing in the microchannel, the surface area for mixing and the diffusion time should increase [17, 18]. In the microfluidic device designed, microbeads packed in the reaction chamber not only increased the surface area for mixing, but also extended the physical path of the substrate and the BTA to pass through, which increased the diffusion time. In other reports, microbeads bed was used for efficiently mixing two laminar flows and increasing enzyme reaction in microchannel [19]. Conclusively, the reaction chamber packed with microbeads made the substrate and the BTA mixed well, which increased the BTA's enzymatic reaction.

4. Conclusions

Botulinum toxins (BTs) are a kind of protease that cleaves a specific sequence of peptide (substrate) by hydrolysis. Here, a

microfluidic device was designed to detect the proteolysis by BT using the Förster resonance energy transfer (FRET) and implemented using the PDMS molding technique. A master for the device having multiple thicknesses of pattern was prepared using gray-scale photolithography. The microfluidic device of "T" shape comprises a main channel with a reaction chamber and a side channel, and the reaction chamber packed with polystyrene microbeads was defined with two weirs fabricated in the main channel. The electrophoresis was used to transport the substrate and the BTA into the reaction chamber. Fluorescence signals due to the enzymatic reaction were observed on the microfluidic device, and the enzymatic reaction was affected by the magnitude of voltage applied. In addition, it was observed that the microbeads packed in the reaction chamber could improve the enzymatic reaction of BT by increasing the diffusion time and surface area for mixing both materials. As a result, the microfluidic device developed in this study can be applied to detect the enzymatic reaction of BT.

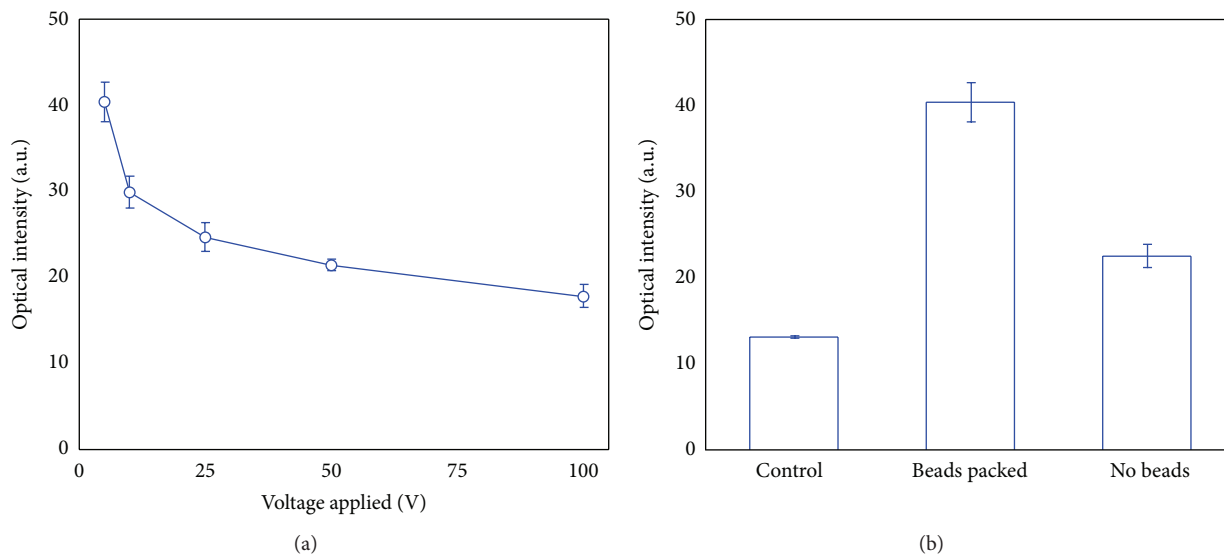


FIGURE 6: Characteristics of the microfluidic device. (a) Effect of electric field applied on the enzymatic reaction of the BTA. (b) Effect of microbeads packed in the reaction chamber as a passive mixer.

Conflict of Interests

The authors declare that there is no conflict of interests regarding the publication of this paper.

Acknowledgment

This research was supported by Korea Electrotechnology Research Institute (KERI) Primary Research Program through the National Research Council of Science & Technology (NST) funded by the Ministry of Science, ICT and Future Planning (MSIP) (no. 15-12-N0101-29).

References

- [1] R. Bashir, "BioMEMS: state-of-the-art in detection, opportunities and prospects," *Advanced Drug Delivery Reviews*, vol. 56, no. 11, pp. 1565–1586, 2004.
- [2] A. Bernard, B. Michel, and E. Delamarche, "Micromosaic immunoassays," *Analytical Chemistry*, vol. 73, no. 1, pp. 8–12, 2001.
- [3] G. H. Seong, W. Zhan, and R. M. Crooks, "Fabrication of microchambers defined by photopolymerized hydrogels and weirs within microfluidic systems: application to DNA hybridization," *Analytical Chemistry*, vol. 74, no. 14, pp. 3372–3377, 2002.
- [4] K. Sato, M. Yamanaka, H. Takahashi, M. Tokeshi, H. Kimura, and T. Kitamori, "Microchip-based immunoassay system with branching multichannels for simultaneous determination of interferon-gamma," *Electrophoresis*, vol. 23, no. 5, pp. 734–739, 2002.
- [5] J. Heo and R. M. Crooks, "Microfluidic biosensor based on an array of hydrogel-entrapped enzymes," *Analytical Chemistry*, vol. 77, no. 21, pp. 6843–6851, 2005.
- [6] CDC, "Botulism," 1999, <http://www.cdc.gov>.
- [7] R. Jin, A. Rummel, T. Binz, and A. T. Brunger, "Botulinum neurotoxin B recognizes its protein receptor with high affinity and specificity," *Nature*, vol. 444, no. 7122, pp. 1092–1095, 2006.
- [8] G. E. Boldt, L. M. Eubanks, and K. D. Janda, "Identification of a botulinum neurotoxin A protease inhibitor displaying efficacy in a cellular model," *Chemical Communications*, vol. 2006, no. 29, pp. 3063–3065, 2006.
- [9] S. S. Arnon, R. Schechter, T. V. Inglesby et al., "Botulinum toxin as a biological weapon: medical and public health management," *The Journal of the American Medical Association*, vol. 285, no. 8, pp. 1059–1070, 2001.
- [10] M. Pires-Alves, M. Ho, K. K. Aberle, K. D. Janda, and B. A. Wilson, "Tandem fluorescent proteins as enhanced FRET-based substrates for botulinum neurotoxin activity," *Toxicon*, vol. 53, no. 4, pp. 392–399, 2009.
- [11] M. Dongo, W. H. Tepp, E. A. Johnson, and E. R. Chapman, "Using fluorescent sensors to detect botulinum neurotoxin activity in vitro and in living cells," *Proceedings of the National Academy of Sciences of the United States of America*, vol. 101, no. 41, pp. 14701–14706, 2004.
- [12] N. R. Shine, K. R. Crawford, and L. J. A. Eaton, "Substrate peptides and assays for detecting and measuring proteolytic activity of serotype a neurotoxin from clostridium botulinum," U.S. Patent No. 6504006, 2003.
- [13] R. F. Service, "Materials science: throwing—or molding—a curve into nanofabrication," *Science*, vol. 273, no. 5273, p. 312, 1996.
- [14] D. C. Duffy, J. C. McDonald, O. J. A. Schueller, and G. M. Whitesides, "Rapid prototyping of microfluidic systems in poly(dimethylsiloxane)," *Analytical Chemistry*, vol. 70, no. 23, pp. 4974–4984, 1998.
- [15] M.-H. Wu, C. Park, and G. M. Whitesides, "Fabrication of arrays of microlenses with controlled profiles using gray-scale microlens projection photolithography," *Langmuir*, vol. 18, no. 24, pp. 9312–9318, 2002.
- [16] S. S. Dukhin and B. V. Derjaguin, *Electrokinetic Phenomena*, John Wiley & Sons, 1974.

- [17] D. R. Meldrum and M. R. Holl, "Microscale bioanalytical systems," *Science*, vol. 297, no. 5584, pp. 1197–1198, 2002.
- [18] M. K. Jeon, J.-H. Kim, J. Noh, S. H. Kim, H. G. Park, and S. I. Woo, "Design and characterization of a passive recycle micromixer," *Journal of Micromechanics and Microengineering*, vol. 15, no. 2, pp. 346–350, 2005.
- [19] G. H. Seong and R. M. Crooks, "Efficient mixing and reactions within microfluidic channels using microbead-supported catalysts," *Journal of the American Chemical Society*, vol. 124, no. 45, pp. 13360–13361, 2002.

Research Article

Investigation of the Validity of the Universal Scaling Law on Linear Chains of Silver Nanoparticles

Mohammed Alsawafta,¹ Mamoun Wahbeh,² and Vo-Van Truong²

¹College of Art and Science, American University of Kuwait, 13034 Safat, Kuwait

²Department of Physics, Concordia University, Montréal, QC, Canada H4B 1R6

Correspondence should be addressed to Mohammed Alsawafta; malsawafta@auk.edu.kw

Received 14 December 2014; Accepted 4 February 2015

Academic Editor: Zhida Xu

Copyright © 2015 Mohammed Alsawafta et al. This is an open access article distributed under the Creative Commons Attribution License, which permits unrestricted use, distribution, and reproduction in any medium, provided the original work is properly cited.

Due to the wide range of variation in the plasmonic characteristics of the metallic nanoparticles arranged in linear arrays, the optical spectra of these arrays provide a powerful platform for spectroscopic studies and biosensing applications. Due to the coupling effect between the interacting nanoparticles, the excited resonance mode is shifted with the interparticle separation. The change in the resonance energy of the coupled mode is expressed by the fractional plasmon shift which would normally follow a universal scaling behavior. Such a universal law has been successfully applied on a system of dimers under parallel polarization. It has been found that the plasmon shift decays exponentially over interparticle spacing. The decay length is independent of both the nanoparticle and dielectric properties of the surrounding medium. In this paper, the discrete dipole approximation (DDA) is used to examine the validity of extending the universal scaling law to linear chains of several interacting nanoparticles embedded in various host media for both parallel and perpendicular polarizations. Our calculations reveal that the decay length of both the coupled longitudinal mode (LM) and transverse modes (TM) is strongly dependent on the refractive index of the surrounding medium (n_m). The decay constant of the LM is linearly proportional to n_m while the corresponding constant of the TM decays exponentially with n_m . Upon changing the nanoparticle size, the change in the peak position of the LM decreases exponentially with the interparticle separation and hence, it obeys the universal law. The sensitivity of coupled LM to the nanoparticle size is more pronounced at both smaller nanoparticle sizes and separations. The sensitivity of the coupled TM to the nanoparticle size on the other hand changes linearly with the separation and therefore, the universal law does not apply in the case of the excited TM.

1. Introduction

Transition metal nanoparticles have attracted considerable attention due to their unique electrical, optical, chemical, and magnetic properties as compared to their bulk counterparts [1, 2]. Noble-metal nanoparticles of a size smaller than the incident wavelength can effectively scatter and selectively absorb light at a certain wavelength in both visible and near-infrared regions [3, 4]. The fascinating optical properties of the metallic nanostructures originate from the excitation of the localized surface plasmon resonance (LSPR) [5, 6]. Due to the enhancement of the local field in the vicinity of the nanoparticles (hot spots), they are used in both biosensing [7, 8] and Surface Enhanced Raman Scattering (SERS) applications [9, 10].

Well-defined metallic nanoparticles arranged in several dimensional arrays provide an interesting opportunity to tune their optical properties over a wide range of optical parameters [11–13]. Periodic structures of nanoparticles can lead to a significant enhancement of the local electromagnetic field, which can be used to improve detection and characterization capabilities down to single-molecule level [13, 14]. Finite chains of metallic nanoparticles are considered as energy guides because of the possibility to transport their plasmonic energies along the chain axis [11, 13, 14]. The tuned plasmonic coupling between the interacting nanoparticles is an efficient way to distribute and direct the coupled energy through the plasmonic elements. In order to optimize the coupled plasmonic energy, one needs to understand the effect of various parameters on the collective plasmonic resonances.

These parameters are the interparticle separation (D), the number of the interacting nanoparticles (N), the polarization states of the incident light, and the refractive index of the host media (n_m) where the nanoparticles are embedded. Depending on the spacing between the nanoparticles, two regimes of plasmonic coupling are considered: (i) when the nanoparticles are arranged in close-packed configurations, they interact via their near-fields and this leads to either a red- or blue-shift of the plasmonic band depending on the type of the incident light [11]. In general, this interaction results in enhanced LSPR and sensing capabilities of SERS. (ii) If the nanoparticles are further displaced by a distance comparable to the incident wavelength, they interact through their radiative fields [11, 15, 16]. These far-field couplings are important for the plasmon enhanced fluorescence of the adsorbed molecules on the nanoparticles surface [11].

The dependency of the plasmon coupling parameters on the interparticle spacing was experimentally studied for nanoparticles of different shapes arranged in various configurations. These nanoparticles were either a dimer of nanodiscs or single-sized spherical nanoparticles arranged in 1D array of different sizes [17]. These nanoparticles were embedded in host media of constant refractive index. No study is reported yet on the effect of the nanoparticle size and the dielectric properties of the host medium on the coupled plasmon resonance for linear chains composed of several plasmonic elements. It has been found that the coupled plasmon resonance wavelength of a dimer system shifts exponentially with the interparticle separation. This shift was expressed by the fractional plasmon shift leading to a universal scaling behaviour [17, 18]. The universality relies on the fact that the decay constant is independent of the nanoparticle size, shape, metal type, and host medium. Consequently, the proposed “plasmon ruler equation” [17, 18] was used to evaluate the spacing between a pair of nanoparticles from their measured plasmon shift. The universal scaling behaviour has been successfully applied to a trimer of nanospheres [19]. To the best of our knowledge, no study is reported on the validity of the scaling behavior for a linear chain of nanoparticles composed of several plasmonic elements.

The first purpose of this paper is to better understand and provide a full picture of the effect of several parameters on the near-field couplings. The parameters include the nanoparticle size, chain size and dielectric properties of the surrounding media at different polarization angles. The second purpose is to examine the validity of extending the universal scaling law to a linear chain that consists of several identical silver nanospheres. We believe that the results of the current study will provide a pathway to design nanoparticle chains for many technological applications. In order to perform the required calculations, the absorption spectra of linear silver chains consisting of spherical nanoparticles were simulated by using the discrete dipole approximation (DDA) method [20–22].

2. The Discrete Dipole Approximation (DDA)

The DDA method is a numerical approximation used to solve Maxwell’s equations of the scattering problem of electromagnetic waves by metallic nanoparticles. Based on the induced

electric dipole moment in the nanoparticles, DDA is used to calculate their optical cross-sections of different shapes and sizes in complex surrounding media. It involves replacing each nanoparticle by a three-dimensional array of polarizable points arranged in a cubic configuration whose side length is equal to the interdipole spacing. The optical properties of the nanoparticles are determined by three factors: (1) the incident wavelength, (2) the polarizability of the nanoparticles, and (3) the mutual interaction between both dipoles within the same nanoparticle and other dipoles in the nearby nanoparticles. The mathematical formulation of DDA is beyond the scope of the current study and is fully described elsewhere [20–22]. DDA is tolerant regarding the target geometry and size. The only limitation to be considered is that the interdipole separation should be smaller than the incident wavelength and any other structural parameters. The accuracy of DDA is widely accepted when a large number of dipoles are used to properly mimic the geometrical parameters of the target. In this study, the desired output of DDA is the absorption cross-section of the nanoparticle, normalized to its geometrical cross-section, which yields the corresponding efficiency (Q_{abs}).

3. Target Geometry and Orientation

The target under investigation is represented by 1D array of N silver nanoparticles of similar polarizabilities. The selected nanoparticles are spherical in shape, different in size, placed at various separations (D), and embedded in different host media. D is the border-to-border distance between the nearest-neighbor nanoparticles and it is usually defined in terms of the sphere radius. The optical spectra of many-body interaction problems are calculated by using the DDA method.

The nanoparticle chains are irradiated with an electromagnetic plane wave. The structure and the orientation of the chains relative to the incident field are shown in Figure 1. The plane of incidence is set to be the x - y plane and the incident electric field (E) is aligned along the y -axis. The linearly polarized (p -polarized) incident light determines the polarization angle (φ) between E and the chain axis. At oblique angles, the incident electric field has two components: one parallel to the chain axis and the other one oriented along the y - z plane. In this case, the observation of dipolar plasmonic modes of different origins is possible under distinct combinations of many parameters. On the other hand, the electric field of the s -polarized light has one component perpendicular to the chain axis at any angle of incidence, and hence, only one plasmonic band of transversal character is expected. In the case of unpolarized light, the spectra are calculated as an average over the two polarizations directions, and the spectrum exhibits all LSPR modes.

In all the simulations, the interdipole separation was kept constant at around 0.53 nm, giving a total of 14330 dipoles per nanosphere. The chosen number of dipoles was sufficient to mimic the structure of the nanosphere correctly and to achieve a proper convergence of the simulations.

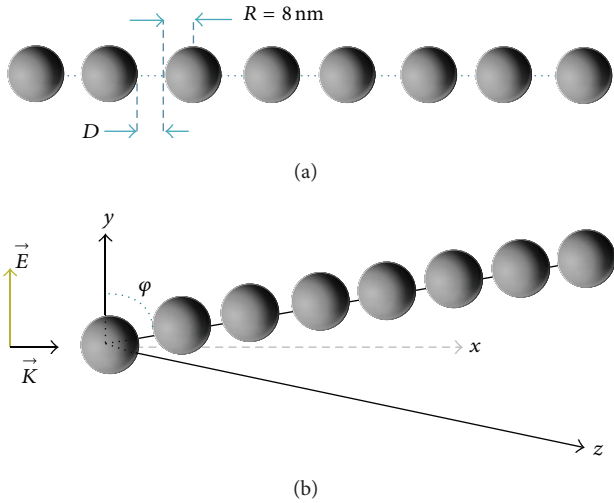


FIGURE 1: Schematic representation of a linear chain composed of 8 silver spheres (diameter $2R$) with an interparticle separation of D . The incident electric field is parallel to the y -axis; φ is the polarization angle between the electric field and the chain axis.

4. Results and Discussion

4.1. Chain Size. Assuming a dipolar approximation, the nanoparticles can be represented as point dipoles. In this sense, the interactions between them are classified into two types: (1) when $D \ll \lambda_{\text{inc}}$, the near-field interactions is dominant with a distance dependence of $1/D^3$; (2) when $\lambda_{\text{inc}}/n_m \approx D$, the plasmonic coupling is dominated by far-field interactions with a distance dependence of D^{-1} . The aim of the present study is to investigate the near-field plasmon coupling, without including any complications from the radiative coupling effect. The near-field coupling between nanoparticles within the chain leads to a pronounced change in the spatial distribution of the local field around the nanoparticles. This results in a significant change in the extinction spectra of the whole system. The optical behavior of interacting nanoparticles is no longer considered as the optical response of a single plasmonic entity but is rather considered as collective coupled resonances of the plasmons of all interacting bodies. For nanoparticles smaller in size, their extinction (absorption and scattering) spectrum is mainly dominated by the absorption cross-section [23]. This can be explained by the small albedo and the enhancement of the near-field absorption. Therefore, the optical spectra of the selected nanoparticles are considered to be represented by their absorption spectra.

It is necessary to represent the chain with a sufficient number of spheres, so that the plasmon parameters (resonance wavelength and plasmon bandwidth) become insensitive or independent of the chain size. To find a convenient N that satisfies this criterion, several chains consisting of different N s of identical spheres are considered. These nanospheres have a monotonic radius of 8 nm and are separated by 4 nm ($D = R/2$). It is assumed that the nanoparticles are embedded in polydimethylsiloxane (PDMS) ($n = 1.46$). The absorption

spectra of the linear chain at different sizes are calculated under both parallel and perpendicular polarizations are shown in Figure 2.

When nanoparticles are placed in close proximity, the local fields of individual nanoparticles overlap, producing a plasmon coupling resonance. These coupled plasmon modes within the chain are caused by the electrostatic interaction between the opposite polarization charges on both sides of the gap separating neighboring nanospheres. This interaction extends from the nanoparticles surface to a distance comparable to their diameter [24]. In the target under investigation, the nanoparticles are placed close enough, so the plasmonic coupling is effective. The plasmon resonance wavelength is either red- or blue-shifted. The type of the plasmonic shift depends strongly on the direction of the incident electric field (incident polarization) [11]. The two scenarios will be discussed separately below in terms of N .

4.1.1. Parallel Polarization. At $\varphi = 0^\circ$, the incident electric field is perfectly aligned along the chain axis which results in the charge oscillations in a direction parallel to that axis. This leads to the excitation of the longitudinal mode (LM). The resonance wavelength of the LM is red-shifted when the N increases. The peak shifts from 425 nm for $N = 2$ to 475 nm for $N = 8$. The increase in the band position is accompanied by a slight increase in the absorption amplitude. The applied and induced electric fields are constructively combined. They are aligned in the same direction and against the Coulombic restoring force. The decrease in the static interaction results in an increase in the period of the electronic oscillations and, hence, the band position of the LM shifts to a higher wavelength as illustrated in Figure 2(a).

For longer chains ($N > 8$), the resonance wavelength becomes insensitive of the chain size with a significant enhancement in the absorption intensity. This enhancement indicates the dominant role of coupled plasmon modes in the chain. In a system of $N \geq 2$, the charges are accumulated at the opposite facing surfaces, thus greatly enhancing the local fields in the gaps between the nanoparticles. For this reason, these gaps are called hot spots and the combined local field amplification is called nanolensing [13, 25]. These spots are localized at both the nanoparticles intersection points and along the line connecting them. Theoretical calculations and experimental measurements of the nanolensing are of great interest because they provide a way to amplify the spectroscopic signal of the adsorbed molecules in the vicinity of the nanoparticles.

The field enhancement is mainly controlled by damping processes of different origins. These processes are classified into radiative and dissipative damping. Due to the small size of the nanoparticles considered in the current study, the decrease in the peak enhancement with increasing N caused by the radiation damping process is negligible. The increase in the absorption amplitude for larger numbers of N has been observed experimentally [13]. Therefore, the theoretical results presented in this work are in agreement with the experimental observations. Wang et al. [13] studied the near-field coupling between spherical silver nanoparticles of

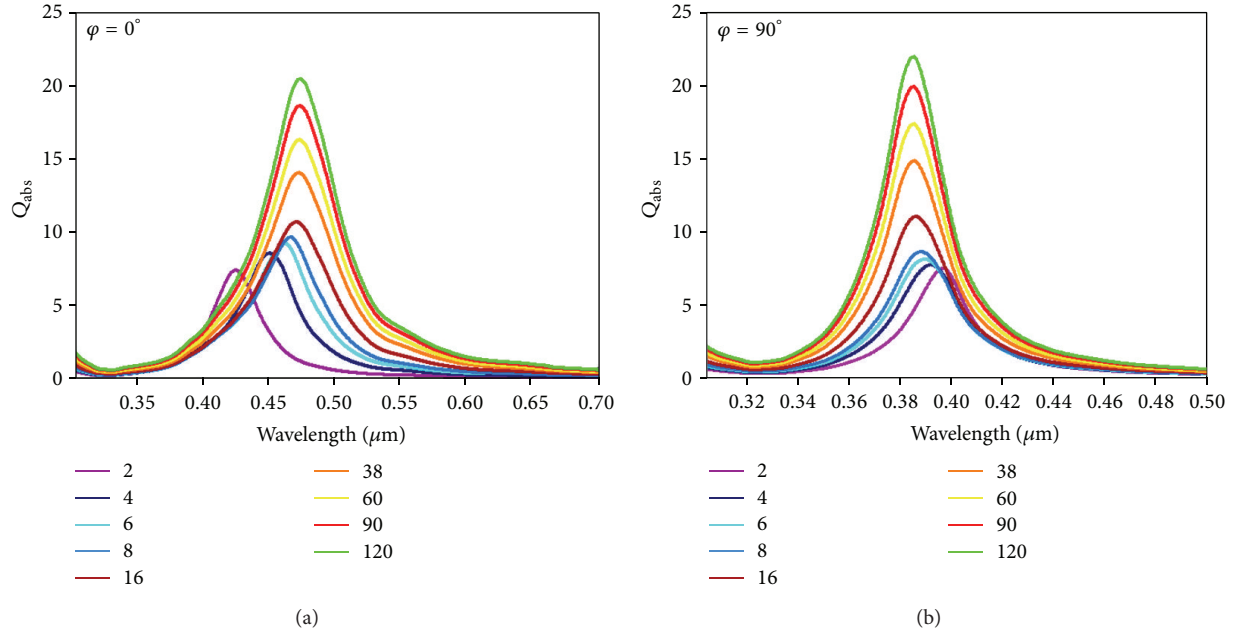


FIGURE 2: Absorption spectra of linear chains composed of various numbers of silver spheres under (a) parallel polarization and (b) perpendicular polarization.

a larger size ($R = 20$ nm) in terms of the chain size. The nanoparticles were arranged in a close-packed linear chain. The nanoparticles were placed very close to each other at a distance of 1 nm. The main finding in their study is that the field enhancement decreased with N which contradicts both previously published experimental results and our current observations. Actually, the selected nanoparticles size is the key for explaining this contradiction. In the case of Wang's study, the nanoparticles were larger and as such, it is expected that the scattering cross-section has the main contribution to the extinction cross-section. This results in an enhancement of the radiation damping process as the size of the chain increases and, hence, decreases the amplitude of the field enhancement.

4.1.2. Perpendicular Polarization. Under perpendicular polarization, the electric field is aligned perpendicular to the chain axis. Therefore, another plasmonic band of different dipolar character is excited (transverse mode (TM)). In this case, the induced electric field is antiparallel (out of phase) to the applied one and it is in the same direction of the restoring force, thus increasing the resonance frequency (blue shift) as shown in Figure 2(b). The change in the band position of the LM is more noticeable as compared to that of the TM. This can be explained by the strong electrostatic interactions between the induced dipoles when the LM is excited. In both polarizations, as N exceeds 8 nanoparticles, no change in the peak position of either LM or TM is observed because the plasmonic coupling reaches a saturation limit. For this reason, as well because of the satisfactory convergences and the reasonable computational costs, the chain consisting of 8 spheres is chosen to be representative of what will be studied in the subsequent sections. Anyhow, adding more nanoparticles into the chain increases the intensity of the induced field

and, hence, the absorption efficiency with no change in the resonance energy of the plasmonic band.

4.2. Effect of the Dielectric Environment on Near-Field Interactions. In order to better understand how the plasmonic coupling influences the plasmonic modes, we compare the absorption spectra of silver linear chains when the nanoparticles ($2R = 8$ nm) are embedded in various environments ($n_m = 1, 1.33, 1.46$, and 1.66 ; the spectra corresponding to the last two values of n_m will be omitted) at different D s ($0.2R, 0.25R, 0.5R, R, 2R$, and $3R$). The dependency of the plasmon couplings on these parameters is studied at various polarization angles.

The absorption spectrum of a single nanosphere is shown in each set of calculated spectra for the linear chains. It exhibits a peak at 355 nm (in air) which represents the well-known Mie's resonance in the quasistatic regime for an isotropic homogenous nanoparticle of spherical shape. Due to the high symmetry order of spherical nanospheres, their optical spectra are independent on both the polarization angle and polarization state of the incident light.

4.2.1. Parallel Polarization. At parallel polarization, the band position of the LM is blue-shifted with D in all media. Due to enhancement of the coupled field, the LM is broadened in all media when nanoparticles are placed at distance smaller than R . At $D \leq R/4$, in addition to the main plasmonic band, a shoulder at lower wavelength can be observed. While the main resonance peaks are due to the plasmonic coupling effect within the chain, the shoulder is associated with a dipole resonance of each single nanosphere [13]. In a water medium, the shoulder is located at a wavelength of around 380 nm with no significant change in either its band position or amplitude.

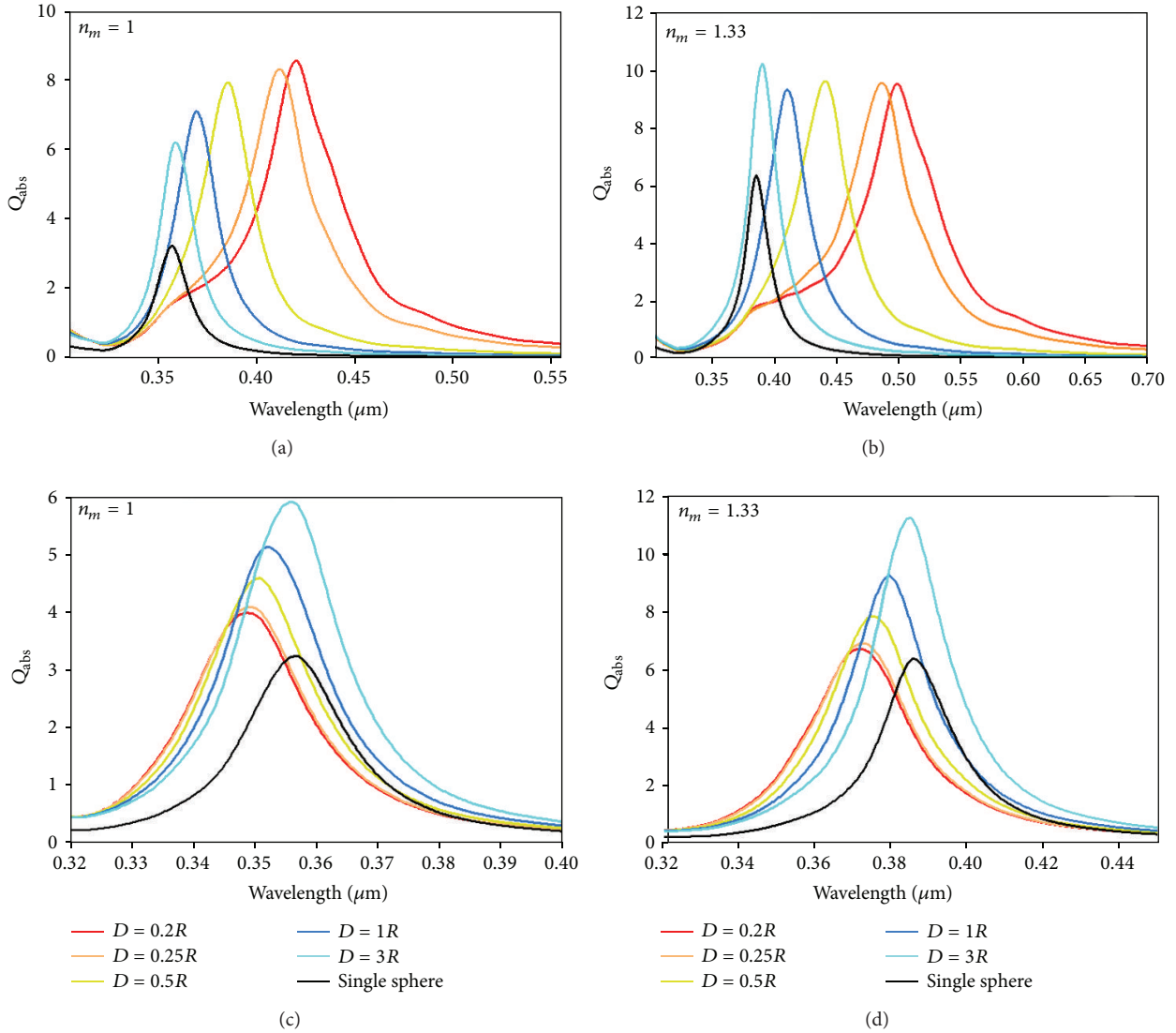


FIGURE 3: Absorption spectra of silver linear chains under (a, b) parallel polarization and (c, d) perpendicular polarization, at different interparticle separations and immersed in various embedding materials.

4.2.2. Perpendicular Polarization. When the incident field is transverse to the chains, the interactions between the nanoparticles are weak and cause a change in the resonance wavelength with D . The resonance wavelength of the TM is red-shifted as D increases as illustrated in Figures 3(c) and 3(d). In the case of perpendicular polarization, in a host media composed of air, the absorption efficiency of nanoparticles increases with D , in contrast to the case when the nanoparticles are illuminated by light of parallel polarization (see Figures 3(a) and 3(b)). In both polarizations, the band position of both TM and LM is red-shifted with n_m , with an increase in the absorption amplitude, as expected.

In an air environment, the absorption efficiency of the LM reaches a maximum around 8.6 at the smallest D ($= 0.2R$) and then gradually decreases as D increases. On the contrary, the amplitude of the TM increases with D . For $D \leq R$, the LM

amplitude tends to have the same value as the surrounding medium becomes denser as shown in Figure 4(a). As the nanoparticles are set apart at a distance larger than the size of an individual sphere ($D = 3R$), a sudden increase in the LM amplitude is observed. On the other hand, the TM amplitude is directly proportional to n_m at all values of D as illustrated in Figure 4(b).

In general, as D increases, the type of the plasmon shift of both modes is in sharp contrast for both polarization directions. The diversity in their optical response can be explained on the basis of the dipole-dipole coupling model. Under parallel polarization, the coupling is attractive, while in the other polarization case, the coupling is repulsive. This results in red and blue shift in the plasmonic bands as D decreases for parallel and perpendicular polarization, respectively. It is clear that the effect of the electromagnetic

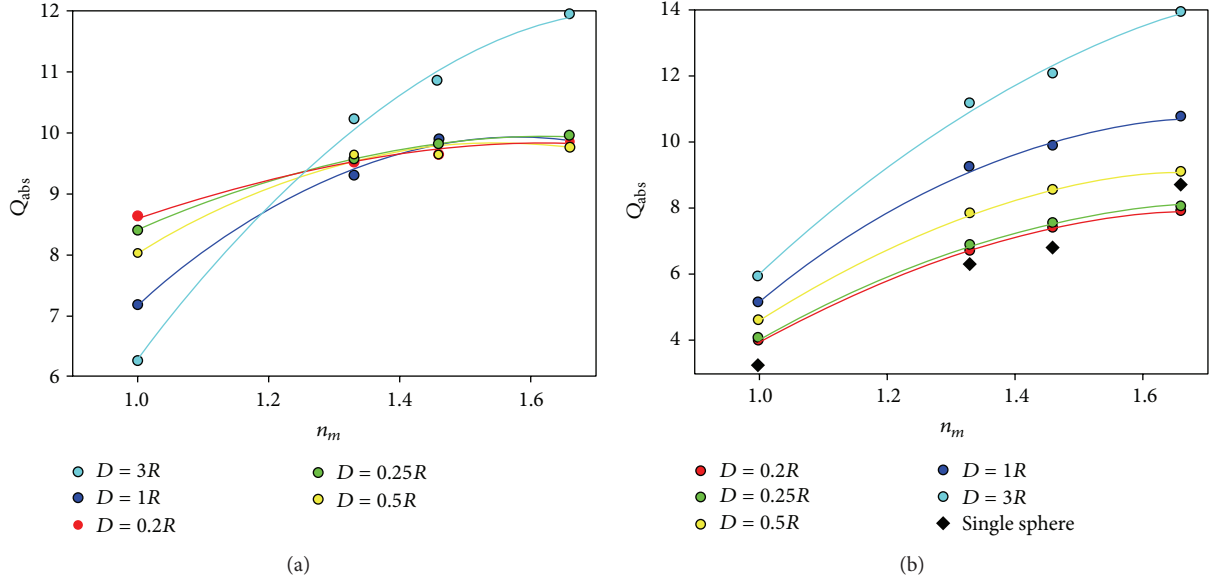


FIGURE 4: Absorption efficiency of various chains at different D s as a function of n_m for (a) parallel and (b) perpendicular polarizations.

coupling is stronger for the parallel polarization, as indicated by the large change in the band position of the coupled resonance mode.

In the case of dimers, the plasmonic couplings cause a shift in the resonance band that decays exponentially with D . Jain et al. [17] have derived a universal plasmon scaling behaviour, according to the so-called plasmon ruler equation. This equation can be exploited to estimate the interparticle separation in a metallic dimer:

$$\frac{\Delta\lambda}{\lambda_o} = \frac{\lambda_{\text{res}} - \lambda_o}{\lambda_o} \approx k \exp\left(\frac{-D/2R}{b}\right), \quad (1)$$

where λ_{res} , λ_o , and b are the fractional plasmon shift, the coupled resonance wavelength, the resonance wavelength of the single nanosphere, and the decay constant, respectively. The value of the constant k depends on the type of the incident polarization. k is positive for parallel polarization which indicates the shift of the LM to the higher wavelength. The negative value of k is associated with perpendicular polarization and it indicates the blue-shift of the TM. In general, k may be used to compare the amount of the plasmon shift; it exhibits larger magnitudes for the silver nanoparticles as compared to that of gold nanoparticles [17]. This indicates that, for silver nanoparticles, the local fields are stronger than the corresponding ones for gold. The interband transitions in the gold nanoparticles occur in the vicinity of the plasmon modes. The excitation of the interband electrons results in damping the resonance modes and hence, reduces the intensity of the local fields compared to that of silver nanoparticles.

As a result of the plasmonic coupling, it has been found that the lattice coherent frequency is also shifted. The change in the phonon frequency decays exponentially with D . The similar trend of both plasmon and phonon frequencies is

TABLE 1: Values of both constants k and b in terms of n_m for parallel polarization.

	$n_m = 1$	$n_m = 1.33$	$n_m = 1.46$	$n_m = 1.66$
b	0.185	0.206	0.221	0.235
k	0.2904	0.4487	0.4881	0.552

TABLE 2: Values of both constants k and b in terms of n_m for perpendicular polarization.

	$n_m = 1$	$n_m = 1.33$	$n_m = 1.46$	$n_m = 1.66$
b	0.933	0.5104	0.45135	0.4274
k	-0.0268	-0.0427	-0.0525	-0.0647

a result of dependency of the general scaling behavior on the field coupling.

The fractional plasmon shift in silver chains embedded in all the selected host exhibits the same universal decay trend as shown in Figure 5 (data are shown for only $n_m = 1.66$). Therefore, the previous equation is still applicable for the multibody interaction problem considered in the current study.

Tables 1 and 2 show the dependency of both k and b on the dielectric properties of the host media for parallel and perpendicular polarizations, respectively. It seems that the value of b is only slightly dependent on n_m for parallel polarization, while the corresponding value for the perpendicular polarization is decreasing significantly with n_m . This means that the coupled TM decays faster than the corresponding LM. This discrepancy originates from the difference in the sensitivity of both modes to the change in the surrounding dielectric medium. The less sensitive the plasmonic mode is to n_m , the faster it will decay with n_m [18]. For the LM, the change in the band position with n_m is more pronounced

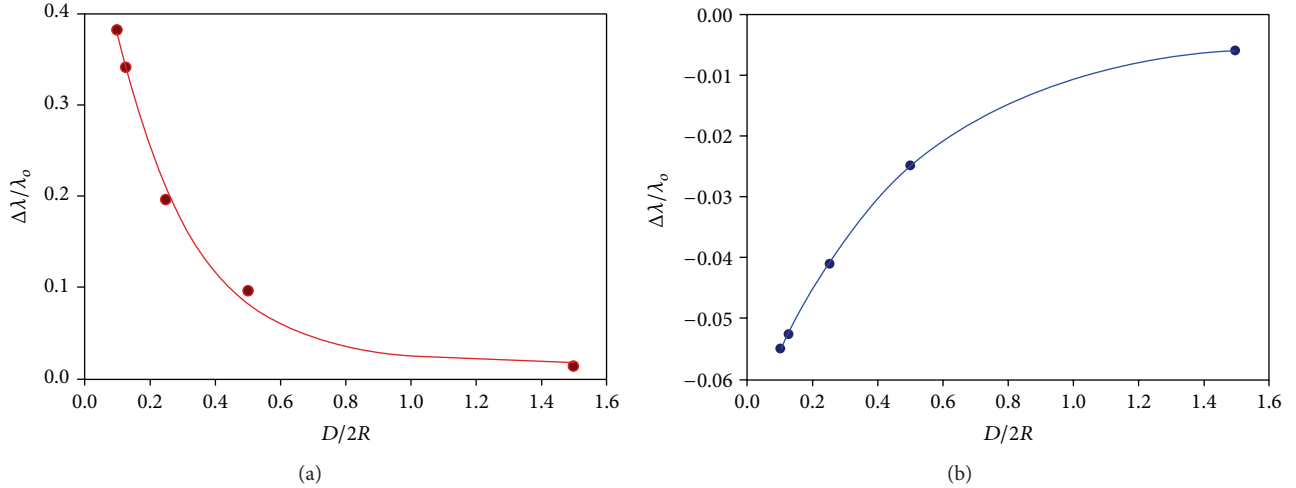


FIGURE 5: Fractional plasmon shift of the silver chains as a function of $D/2R$ at $n_m = 1.66$ for (a) parallel and (b) perpendicular polarizations.

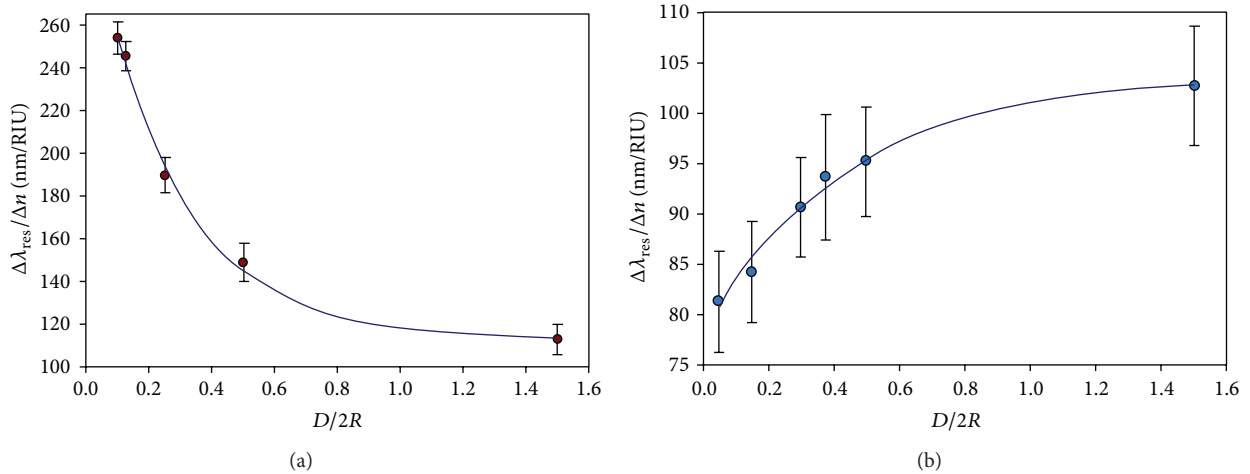


FIGURE 6: Plasmon resonance sensitivity of a silver nanoparticles chain to the surrounding medium as a function of the interparticle separation in units of sphere diameter at (a) parallel and (b) perpendicular polarizations.

compared to that of the TM, which can be indicated by the difference in the k value. While the value of k shows how sensitive the plasmonic mode is to n_m , the sign of k shows the type of the plasmonic shift. A positive value of k indicates the red shift of LM and the negative value shows the blue shift of the TM. Jain and El-Sayed [18] found that the shift in the resonance increases in a denser medium (larger dielectric constant). The previously published results are in an agreement with our current observations.

Jain and El-Sayed also found that the value of b for a system composed of gold nanodisc dimer is approximately equal to 0.2 in units of nanoparticles size for a polarization parallel to the interparticle axis. The b value is independent of the nanoparticle shape, metal type, and the dielectric properties of the surrounding medium. This conclusion does not apply in our case; the value of b is strongly dependent on both the dielectric properties of the surrounding medium and the polarization state of the incident light. The b of the LM

slightly increases showing a linear trend with n_m and it is less than the expected value based on his observations. In the case of the orthogonal polarization, the corresponding value of b shows a more nonlinear (exponential) dependency on n_m .

The coupling resonance wavelength is red-shifted in a linear proportion with increasing n_m at any value of D (data not shown). The slopes of these linear proportions as function of $D/2R$ are plotted in Figure 6. The sensitivity of the plasmonic mode to any change in the surrounding medium is monitored by the shift of its prospective peak position ($\Delta\lambda_{res}$) per Refractive Index Unit (RIU) as shown in Figure 6. The band position of both coupled plasmonic modes is red-shifted linearly in a dense medium as compared to the one in the vacuum. Increasing the value of the dielectric function of the surrounding adjusts the resonance condition and results in the lowering of the restoring force (the coulombic interaction). Hence, the resonance occurs at a lower frequency. The LM exhibits larger magnitudes of red shift at smaller

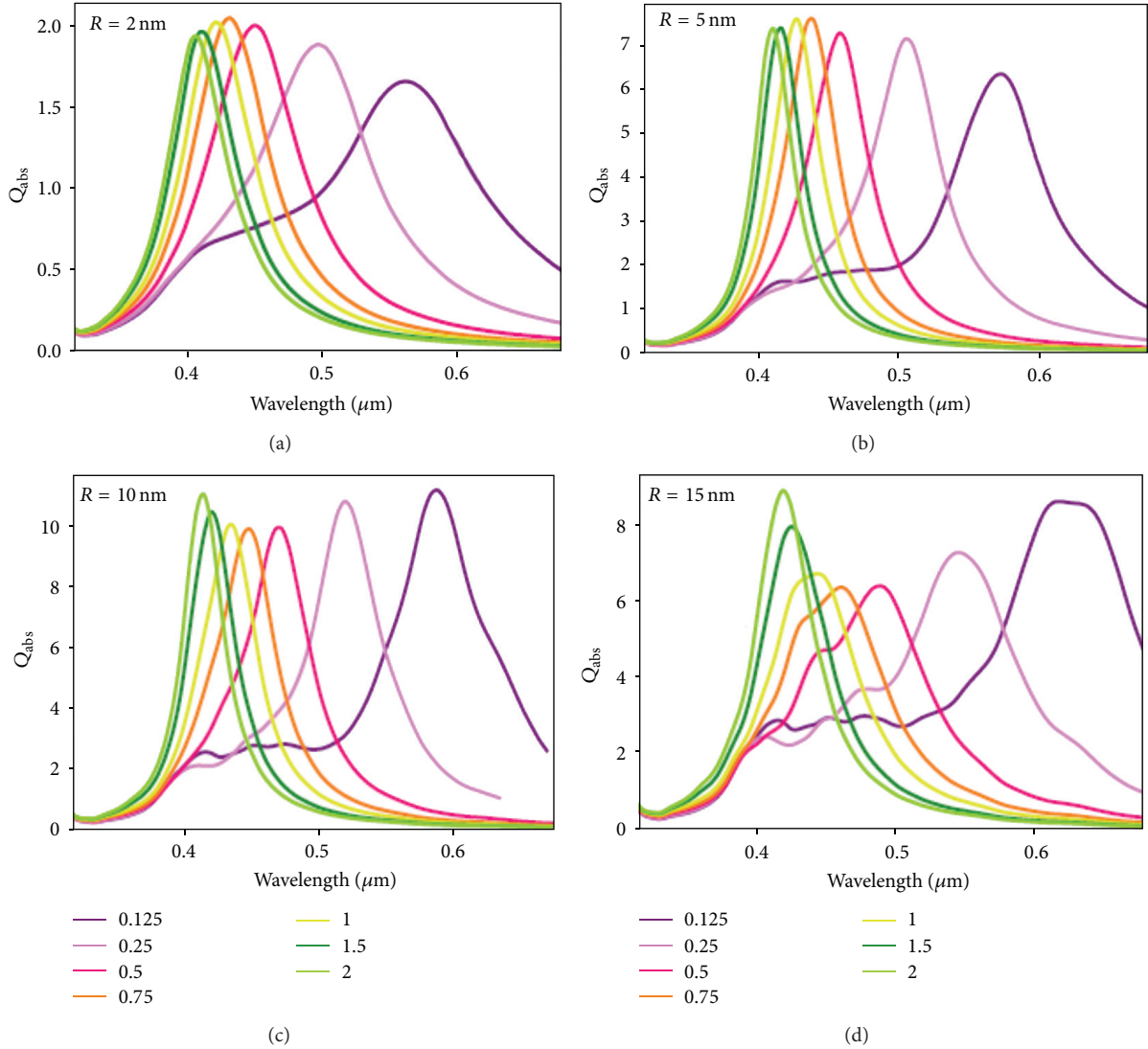


FIGURE 7: Absorption spectra of silver nanoparticles of different sizes arranged in linear chains under parallel polarization at different D s (listed in the legends).

D in response to an increment in the n_m . In other words, the sensitivity of the nanoparticles within the chain can be highly enhanced by decreasing D under parallel polarization. In the case of parallel polarization, we found that the plasmon resonance is shifted exponentially with increasing $D/2R$ with $b = 0.268$. Jain and El-Sayed [18] calculated the sensitivity of a 40 nm diameter gold nanosphere pair and found that it decays exponentially with increasing $2D/R$ with $b = 0.18$. The difference in b originates from the diversity in both the nanoparticles size and the metal type.

On the contrary, at transversal excitation of the plasmonic mode, the sensitivity decays with decreasing $D/2R$ with $b = 0.43$ as shown in Figure 6(b). The decay time (τ) is defined as reciprocal of b and thus the sensitivity of the TM ($b = 0.43$) decays faster than the corresponding one of the LM ($b = 0.268$). The diversity of the sensitivities between both modes is due to the difference in the field couplings. The strong

plasmonic coupling under parallel polarization explains the higher sensitivity of the LM as compared to that of the TM.

4.3. Effect of the Nanoparticles Size on Near-Field Interactions.

To investigate the effect of nanoparticle size on the near-field couplings, a linear chain composed of eight identical spherical silver nanoparticles is simulated under both parallel and perpendicular polarizations. The radius of the spheres ranges between 2 nm and 15 nm, at interparticle separations ranging between $D = R/8$ and $D = 2R$. The n_m is set to that of PDMS. The absorption spectra of silver chains at $\varphi = 0^\circ$ and 90° are plotted, respectively, in Figures 7 and 9.

4.3.1. Parallel Polarization. The profile lines of the absorption spectra are smooth and streamlined as long as the electric field is uniform across the silver nanoparticles. By increasing the particle size and decreasing D , the phase retardation effect

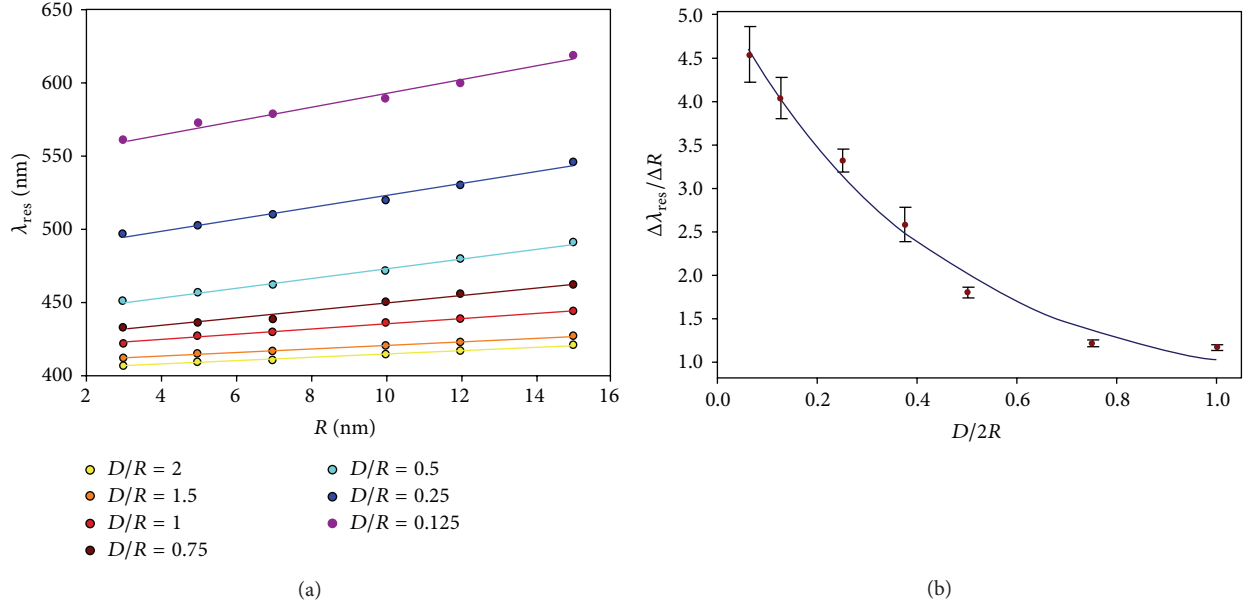


FIGURE 8: (a) LM of linear chains at different D s (listed in the legend) as a function of R . (b) The change in the resonance wavelength of the LM is red-shifted linearly with R at all D s.

becomes significant. Nanoparticles of larger size experience this effect and it yields the excitation of plasmonic modes of quadrupole character. The quadrupole peaks are excited between 450 and 500 nm with relatively small amplitudes as shown in Figures 7(c) and 7(d). As stated earlier, the excited plasmonic band observed at 400 nm represents Mie's resonance of the individual sphere. Eventually, increasing the component particles size, the plasmon coupling absorption bands became deformed and deviated from the Gaussian bell shape.

The coupled resonance wavelength (LM) is linearly red-shifted with R for any value of D as shown in Figure 8(a). The slope of the straight lines represents the sensitivity of the LM to any change of R . To further investigate the sensitivity of the band position of the LM to the D in terms of R , the ratio $\Delta\lambda_{\text{res}}/\Delta R$ has been calculated at various D s. It is found that this ratio decays exponentially ($b = 0.413$ and $a = 4.657$) with D/R as shown in Figure 8(b). As D/R decreases from 1 to 0.12, the sensitivity ($\Delta\lambda_{\text{res}}/\Delta R$) increases up to 4.54 nm per nm change in R . Thus, the dependency of the plasmonic energy of the LM on nanoparticles size is more pronounced at smaller R and, especially, at smaller D . This result is in contradiction with the universality of the plasmon ruler law derived by Jain et al. [17], whereas it agrees with Encina and Coronado's work [26] illustrating that, in a system, composed of silver nanosphere pairs, the fractional plasmon shift depends on the size of the nanoparticle pair.

4.3.2. Perpendicular Polarization. At $\varphi = 90^\circ$, the excited plasmonic band has a transversal character. The resonance wavelength of the TM is blue-shifted with decreasing D at all values of R . The absorption spectra calculated for different R s are plotted in Figure 9.

The result of the simulations shows that the absorption spectrum of an individual nanosphere depends strongly on its size. Upon increasing the size, it is found that the absorption efficiency linearly increases as R increases until it reaches a maximum value at $R = 13$ nm as shown in Figure 10(a). In the case of the nanoparticles arranged in 1D arrays, the coupling energy reduces the optimum size (R_0) corresponding to the maximum absorption. The value of R_0 of an isolated sphere is reduced in the chain from 13 nm to 12 nm, 8 nm for perpendicular and parallel polarizations, respectively. When $R_0 > R$, the extinction efficiency has mainly contributions from the scattering cross-section resulting in decreased absorption amplitude as shown in Figure 10(a). The phase retardation effect is not obvious in the absorption spectra of the TM. It seems that the quadrupole modes are excited in the vicinity of the TM, making them indistinguishable because of their small relative amplitudes to the dominant TM.

The sensitivity of the transversal coupled resonance to R ($\Delta\lambda_{\text{res}}/\Delta R$) as a function of the dimensionless quantity $D/2R$ is shown in Figure 10(b). It is found that $\Delta\lambda_{\text{res}}/\Delta R$ decreases linearly with increasing D and that it does not obey the universal scaling behavior.

5. Conclusion

In summary, we have examined (the generalization of) the universal scaling behavior for spherical silver nanoparticles arranged in finite linear chains (eight nanoparticles) and embedded in different host media. The results of simulation show that the plasmon ruler equation can be successfully extended to represent the fractional plasmon shift of many interacting nanoparticles. The decay length and the amount of the fractional shift of the silver linear chains strongly

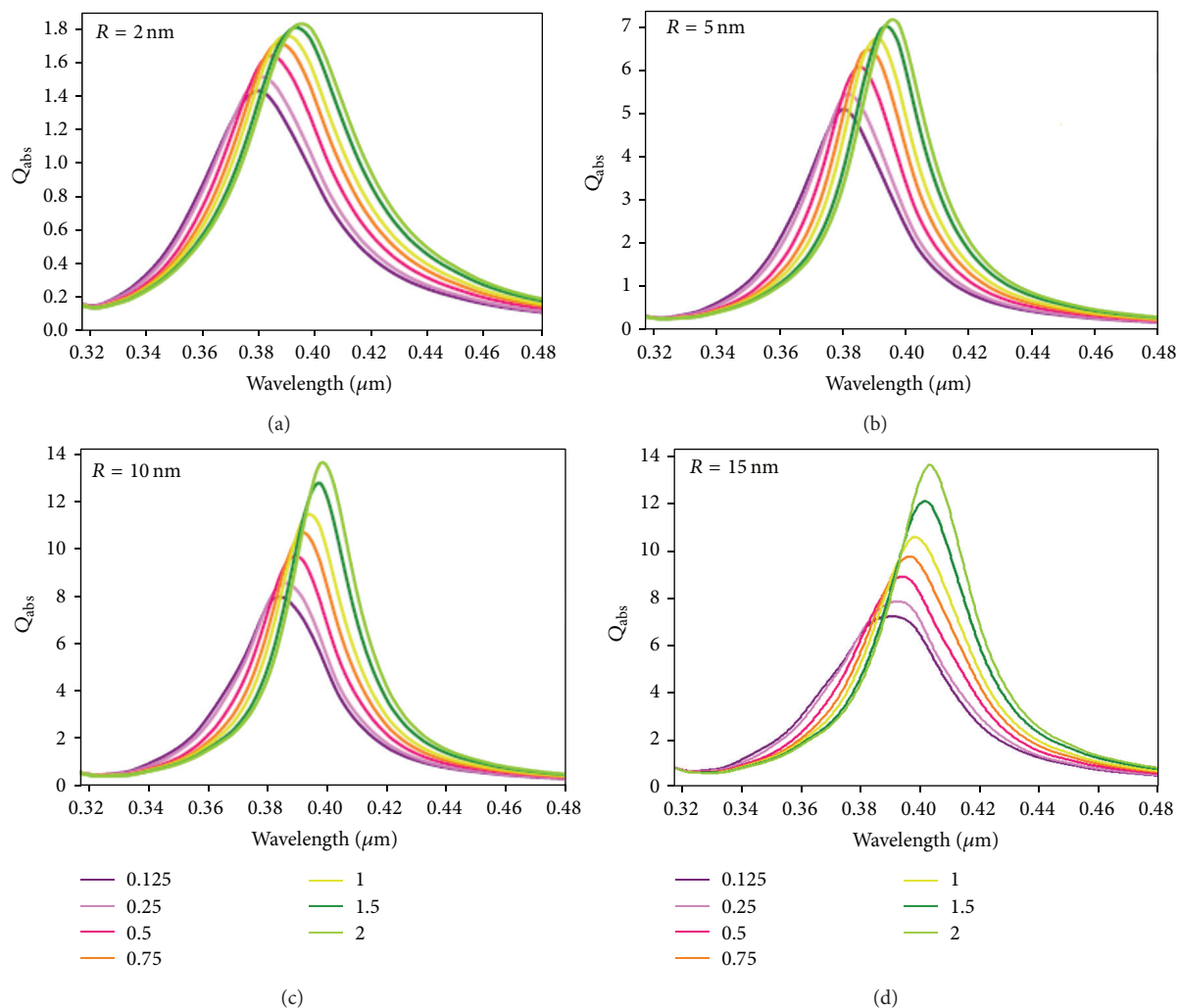


FIGURE 9: Absorption spectra of silver nanoparticles of different sizes and arranged in linear chains under perpendicular polarization at different D s (listed in the legends).

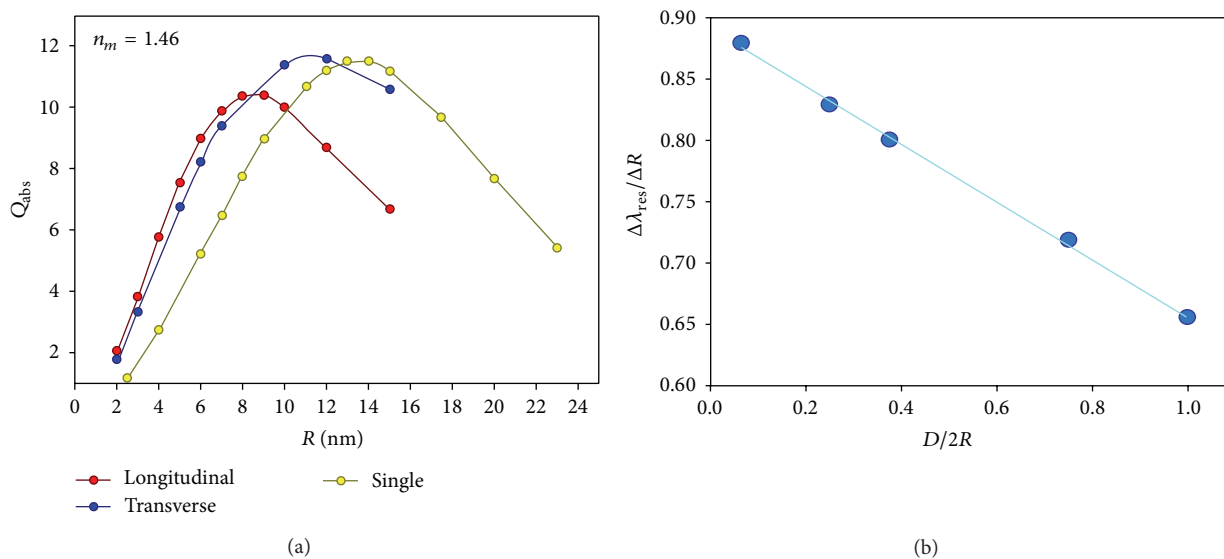


FIGURE 10: (a) Absorption efficiency of the dipole plasmon resonance as a function of R for (i) an individual silver nanoparticles (yellow) and (ii) a linear silver chain at the $D = R$ (under parallel polarization in red and under perpendicular polarization in blue). (b) Sensitivity of the TM to R ($\Delta\lambda_{\text{res}}/\Delta R$) as a function of $D/2R$.

depend on the polarization state of the incident polarization. The LM exhibits a significant shift of the plasmon resonance (indicated by the value of k) as compared to that of the TM. This can be explained by the fact that the enhancement of the local field under parallel polarization is more pronounced. On the other hand, the decay of the TM shows a strong dependency on the dielectric function of the surrounding medium. It decays twice faster than the LM, as the host medium becomes denser.

The dependency of the universal scaling behavior on the nanoparticle size within the linear chains is also examined. The sensitivity of the both the coupled plasmonic modes (LM and TM) shows a strong dependency on the size of the interacting nanoparticles. The change in the longitudinal resonance wavelength with respect to the nanoparticles size ($\Delta\lambda_{\text{res}}/\Delta R$) decays exponentially with D/R and obeys the universal law. The dependency of the longitudinal plasmonic energy on nanoparticles size is more pronounced at smaller values of R and D . The corresponding sensitivity of the TM changes linearly with D/R , which means that the universal law does not apply in this case.

Conflict of Interests

The authors declare that there is no conflict of interests regarding the publication of this paper.

Acknowledgment

This work has been supported by the Natural Sciences and Engineering Research Council of Canada (NSERC) which is gratefully acknowledged.

References

- [1] Y. Fang, "Optical absorption of nanoscale colloidal silver: aggregate band and adsorbate-silver surface band," *The Journal of Chemical Physics*, vol. 108, no. 10, pp. 4315–4318, 1998.
- [2] G. Schmid, *Clusters and Colloids: From Theory to Applications*, vol. 7, VCH, Weinheim, Germany, 1994.
- [3] M. Alsawafta, M. Wahbeh, and V.-V. Truong, "Simulated optical properties of gold nanocubes and nanobars by discrete dipole approximation," *Journal of Nanomaterials*, vol. 2012, Article ID 283230, 9 pages, 2012.
- [4] M. Alsawafta, M. Wahbeh, and V.-V. Truong, "Plasmonic modes and optical properties of gold and silver ellipsoidal nanoparticles by the discrete dipole approximation," *Journal of Nanomaterials*, vol. 2012, Article ID 457968, 10 pages, 2012.
- [5] K. A. Willets and R. P. van Duyne, "Localized surface plasmon resonance spectroscopy and sensing," *Annual Review of Physical Chemistry*, vol. 58, pp. 267–297, 2007.
- [6] E. Hutter and J. H. Fendler, "Exploitation of localized surface plasmon resonance," *Advanced Materials*, vol. 16, no. 19, pp. 1685–1706, 2004.
- [7] J. N. Anker, W. P. Hall, O. Lyandres, N. C. Shah, J. Zhao, and R. P. Van Duyne, "Biosensing with plasmonic nanosensors," *Nature Materials*, vol. 7, no. 6, pp. 442–453, 2008.
- [8] W. J. Galush, S. A. Shelby, M. J. Mulvihill, A. Tao, P. Yang, and J. T. Groves, "A nanocube plasmonic sensor for molecular binding on membrane surfaces," *Nano Letters*, vol. 9, no. 5, pp. 2077–2082, 2009.
- [9] B. Nikoobakht, J. Wang, and M. A. El-Sayed, "Surface-enhanced Raman scattering of molecules adsorbed on gold nanorods: off-surface plasmon resonance condition," *Chemical Physics Letters*, vol. 366, no. 1-2, pp. 17–23, 2002.
- [10] R. F. Aroca, R. A. Alvarez-Puebla, N. Pieczonka, S. Sanchez-Cortez, and J. V. Garcia-Ramos, "Surface-enhanced Raman scattering on colloidal nanostructures," *Advances in Colloid and Interface Science*, vol. 116, no. 1–3, pp. 45–61, 2005.
- [11] A. O. Pinchuk and G. C. Schatz, "Nanoparticle optical properties: far- and near-field electrodynamic coupling in a chain of silver spherical nanoparticles," *Materials Science and Engineering B: Solid-State Materials for Advanced Technology*, vol. 149, no. 3, pp. 251–258, 2008.
- [12] L. Zhao, K. Lance Kelly, and G. C. Schatz, "The extinction spectra of silver nanoparticle arrays: influence of array structure on plasmon resonance wavelength and width," *The Journal of Physical Chemistry B*, vol. 107, no. 30, pp. 7343–7350, 2003.
- [13] Z. B. Wang, B. S. Luk'yanchuk, W. Guo et al., "The influences of particle number on hot spots in strongly coupled metal nanoparticles chain," *The Journal of Chemical Physics*, vol. 128, no. 9, Article ID 094705, 2008.
- [14] B. Willingham and S. Link, "Energy transport in metal nanoparticle chains via sub-radiant plasmon modes," *Optics Express*, vol. 19, no. 7, pp. 6450–6461, 2011.
- [15] T. R. Jensen, M. L. Duval, K. Lance Kelly, A. A. Lazarides, G. C. Schatz, and R. P. Van Duyne, "Nanosphere lithography: effect of the external dielectric medium on the surface plasmon resonance spectrum of a periodic array of silver nanoparticles," *Journal of Physical Chemistry B*, vol. 103, no. 45, pp. 9846–9853, 1999.
- [16] A. J. Haes, S. Zou, G. C. Schatz, and R. P. van Duyne, "A nanoscale optical biosensor: the long range distance dependence of the localized surface plasmon resonance of noble metal nanoparticles," *Journal of Physical Chemistry B*, vol. 108, no. 1, pp. 109–116, 2004.
- [17] P. K. Jain, W. Huang, and M. A. El-Sayed, "On the universal scaling behavior of the distance decay of plasmon coupling in metal nanoparticle pairs: a plasmon ruler equation," *Nano Letters*, vol. 7, no. 7, pp. 2080–2088, 2007.
- [18] P. K. Jain and M. A. El-Sayed, "Noble metal nanoparticle Pairs: effect of medium for enhanced nanosensing," *Nano Letters*, vol. 8, no. 12, pp. 4347–4352, 2008.
- [19] P. K. Jain and M. A. El-Sayed, "Surface plasmon coupling and its universal size scaling in metal nanostructures of complex geometry: elongated particle pairs and nanosphere trimers," *The Journal of Physical Chemistry C*, vol. 112, no. 13, pp. 4954–4960, 2008.
- [20] B. T. Draine and P. J. Flatau, "Discrete-dipole approximation for periodic targets: theory and tests," *The Journal of the Optical Society of America A*, vol. 25, no. 11, pp. 2693–2703, 1994.
- [21] M. J. Collinge and B. T. Draine, "Discrete-dipole approximation with polarizabilities that account for both finite wavelength and target geometry," *Journal of the Optical Society of America A*, vol. 21, no. 10, pp. 2023–2028, 2004.
- [22] J. J. Goodman, B. T. Draine, and P. J. Flatau, "Application of fast-Fourier-transform techniques to the discrete-dipole approximation," *Optics Letters*, vol. 16, no. 15, pp. 1198–1200, 1991.
- [23] P. K. Jain, K. S. Lee, I. H. El-Sayed, and M. A. El-Sayed, "Calculated absorption and scattering properties of gold nanoparticles of different size, shape, and composition: applications in biological imaging and biomedicine," *Journal of Physical Chemistry B*, vol. 110, no. 14, pp. 7238–7248, 2006.

- [24] C. Noguez, "Surface plasmons on metal nanoparticles: the influence of shape and physical environment," *The Journal of Physical Chemistry C*, vol. 111, no. 10, pp. 3806–3819, 2007.
- [25] S. Foteinopoulou, J. P. Vigneron, and C. Vandembem, "Optical near-field excitations on plasmonic nanoparticle-based structures," *Optics Express*, vol. 15, no. 7, pp. 4253–4267, 2007.
- [26] E. R. Encina and E. A. Coronado, "Plasmon coupling in silver nanosphere pairs," *Journal of Physical Chemistry C*, vol. 114, no. 9, pp. 3918–3923, 2010.

Research Article

Immobilization Techniques and Integrated Signal Enhancement for POC Nanocolor Microfluidic Devices

Marlies Schlauf,¹ Saied Assadollahi,¹ Roland Palkovits,^{1,2}
Peter Pointl,¹ and Thomas Gerhard Maria Schalkhammer¹

¹Attophotonics Biosciences GmbH, Viktor Kaplan Straße 2, 2700 Wiener Neustadt, Austria

²Department of Micro- and Nanosystems, University of Applied Sciences, Johannes Gutenberg-Straße 3, 2700 Wiener Neustadt, Austria

Correspondence should be addressed to Marlies Schlauf; marlies.schlauf@attophotonics.com

Received 24 April 2015; Accepted 29 July 2015

Academic Editor: Hyunjong Jin

Copyright © 2015 Marlies Schlauf et al. This is an open access article distributed under the Creative Commons Attribution License, which permits unrestricted use, distribution, and reproduction in any medium, provided the original work is properly cited.

Resonance enhanced absorption (REA) nanocolor microfluidic devices are new promising bioassay platforms, which employ nanoparticle- (NP-) protein conjugates for the immunodetection of medically relevant markers in biologic samples such as blood, urine, and saliva. The core component of a REA test device is a PET chip coated with aluminum and SiO₂ thin layers, onto which biorecognitive molecules are immobilized. Upon addition of a sample containing the analyte of interest, a NP-protein-analyte complex is formed in the test device that is captured on the REA chip, for example, via streptavidin-biotin interaction. Thereby, a colored symbol is generated, which allows optical readout. Silver enhancement of the bound nanoparticles may be used to increase the sensitivity of the assay. Herein, we demonstrate that adsorptive immobilization via a cationic polymeric interlayer is a competitive and fast technique for the binding of the capture protein streptavidin onto planar SiO₂ surfaces such as REA biochips. Moreover, we report the development of a silver enhancement technology that operates even in the presence of high chloride concentrations as may be encountered in biologic samples. The silver enhancement reagents may be integrated into the microfluidic assay platform to be released upon sample addition. Hereby, a highly sensitive one-step assay can be realized.

1. Introduction

Modern point-of-care diagnostics strongly relies on low-cost, portable, easy-to-handle platforms especially in regions with limited resources and medical infrastructure.

Microfluidic devices also called μ TAS (micro total analysis systems) or lab-on-a-chip systems belong to the most promising technologies studied in this context. A major part of the respective research focuses on the combination of microfluidics with immunoassay technology being the most valuable tool for the detection of medically relevant markers. Compared to conventional immunoassays microfluidic systems offer efficient mass transport and a reduced surface to volume ratio. Thus fast analyses can be performed even with small sample volumes and significantly lower amounts of antibodies and reagents are required [1]. Detection strategies currently studied and employed for microfluidic platforms range from fluorimetric over colorimetric to electrochemical techniques (see, e.g., [2]). The selection of the best suited

technology is often a compromise between simplicity and sensitivity. Where quantification is an issue and low detection limits are most critical, electrochemical systems are generally the first choice. For quick tests and screenings, however, a noninstrumental readout may be preferred, which implicates a colorimetric detection strategy.

Resonance enhanced absorption (REA) is an optical phenomenon already described by Leitner et al. [3] in 1993. In 1998, the application of the effect in a bioassay was reported [4]. Its potential as a novel (bio)analytical platform has been studied extensively since then (see [5–7]). In 2009, our group developed a novel microfluidic diagnostic device combining REA technology with an innovative fluidic setup operating by passive capillary force. The manufacture of the device out of PET films by hot embossing or laser micromachining and the physical basics of REA were discussed in detail by Assadollahi et al. [8]. Current research focuses on the optimization of this system as versatile, fast, and sensitive microfluidic POC one-step-immunoassay platform.

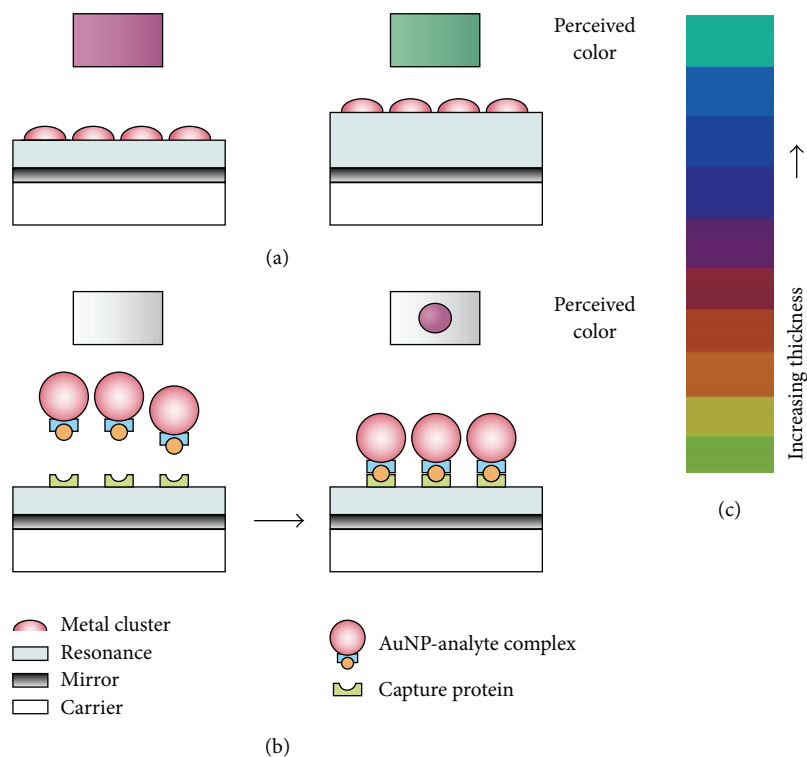


FIGURE 1: Classical REA setup and bioanalytical REA assay. (a) Schematic drawing of the classical 4-layer REA setup with two different resonance layer thicknesses. The colored squares above the metal cluster layers indicate the film color, which varies with resonance layer thickness. (b) Schematic drawing of a bioanalytical REA assay before (left) and after (right) binding of AuNP-analyte complexes to the capture protein layer. (Without top metal cluster REA materials exhibit the color of the base mirror layer, generally silver to gray.) The NP-analyte complex may comprise further mediator proteins, which are not depicted here. (c) *REA color spectrum*. By stepwise increase of the resonance layer thickness from 0 to 300 nm, a broad range of colors can be obtained.

In brief, resonance enhanced absorption requires a four-layer setup as depicted in Figure 1(a). It comprises a metal mirror layer, a transparent distance layer of nanometric thickness (<300 nm), and a (sub)monolayer of metal nanoclusters.

The sandwich of nanocluster layer and mirror layer at a well-defined distance results in optical resonance. Compared to the absorption spectrum of the nanocluster layer alone this resonance effect causes an 8-fold or higher increase in absorption of electromagnetic radiation of certain wavelengths [5]. As a consequence, a color in the visible range of the electromagnetic spectrum is obtained (which is commonly different from the color of the nanoclusters). The absorption maxima shift depending on the distance layer thickness, which allows the fabrication of REA materials of various colors and multicolored surfaces (see Figure 1(c)).

For analytical purposes REA chips without top metal cluster layer are used as platforms for colorimetric sandwich type immunoassays employing metal nanoparticle-conjugated probes (Figure 1(b)). If the antigen of interest is present in a sample, a complex comprising metal nanoparticle probe, analyte, and—if required—additional mediator proteins is formed and binds to the chip surface. Thereby, the REA structure is completed and a colored symbol appears indicating the positive detection of the analyte. The color intensity is proportional to the concentration of the captured

NPs. Like in traditional lateral flow assays (LFAs) all assay reagents are provided in the microfluidic cell in dry form and are released upon sample addition. Such REA immunoassays have already been used for the detection of HSA and IL-6 as reported by Assadollahi et al. [8] and Palkovits et al. [9]. Similar systems based on metal nanoparticle-conjugated probes have been developed by other groups recently (see, e.g., [10–12]). However, those colorimetric tests rely solely on the light absorption of the captured nanoparticle layer. They do not profit from the signal enhancing effect of a REA structure, which may allow reaching even lower detection limits.

In order to provide a flexible platform for a range of analytes, streptavidin should be introduced into the described microfluidic REA technology as capture reagent. Thereby, already established immunoassays employing biotin-tagged antibodies for detection could be combined with the device without the requirement for individual optimization of chip coating procedures.

For low-cost manufacture an efficient and simple technique for streptavidin immobilization must be employed, however. In order to identify a suitable method we performed a screening of published approaches and variations thereof and evaluated their efficiency. The four most successful techniques we identified are described herein. Basically, there are three different approaches that can be taken in protein

immobilization: (1) Adsorption or spotting is a strikingly simple technique but commonly leads to random protein orientation. However, it has proven sufficient for various applications [13]. (2) Covalent immobilization limits the possible orientations of the immobilized protein and thereby can increase or at least homogenize the reactivity of the protein layer. It may, however, also decrease the reactivity if the employed technique entails molecule orientations that hide active sites from potential interaction partners. The choice of the immobilization chemistry depends on the reactive groups that are available or can be created on the protein and the substrate [14]. Recent developments even allow highly selective, oriented conjugation combining the advantages of protein tags with covalent methods [15]. (3) By immobilization via tags (e.g., myc, streptavidin-biotin interaction) highly oriented protein layers can be prepared, even from impure lysates or solutions with low concentration. [14]. However, employing tags for immobilization was not considered in this study as the streptavidin functionalities were required for antibody-antigen capture. Each streptavidin molecule provides four binding sites. The orientation of streptavidin after immobilization should therefore have only minor influence on its binding capacity. Thus, adsorptive as well as covalent immobilization techniques were considered suited for the preparation of streptavidin coatings on the SiO₂ surface of REA chips.

A major drawback of microfluidic systems is the limited number of binding sites that can be created on the commonly flat detection area compared to the generally porous substrates of LFAs. Recent publications suggest that a pronounced 3D structure of the chemical linkers that are used to bind the immobilized molecules to the substrate can be helpful to obtain a high density of binding sites (as reviewed in [16]). Polyethylenimine (PEI) and carboxymethylcellulose (CMC) are two high molecular weight polymers that have been described previously as substrates for protein immobilization [17–19]. Due to its strong positive charge PEI was selected for adsorptive immobilization of streptavidin, which is, with a pI of ~5, negatively charged in the pH-neutral buffers used for chip preparation. CMC was tested as platform for carbodiimide-mediated covalent streptavidin immobilization. As there are several protocols available for the respective conjugation reaction, a screening was performed to identify suitable approaches. To determine the efficiency of the individual immobilization methods and the functionality of the generated streptavidin layers, all chips were tested in a standardized microfluidic immunoassay at defined analyte concentration. As depicted in Figure 1(b) the assay is based on the binding of a nanoparticle-conjugated probe to the analyte in solution and the subsequent capture of this complex on the REA chip surface. However, in contrast to the illustration, a second biotin-tagged probe is required to mediate the binding of the analyte-NP complex to the streptavidin layer on the chip. Two of the most competitive immobilization approaches that could be established are described herein. Chips prepared using CMC or PEI were compared with chips coated via adsorption of streptavidin to 3-APTES. Thereby, it was evaluated whether polymer interlayers actually confer higher biorecognitive capacity to REA bioassay chips.

The limited number of binding sites in microfluidic systems may also be compensated by secondary signal enhancement reactions. Assadollahi et al. described how nanoparticle-catalyzed electroless deposition of metallic silver from solution can be used to boost sensitivity and signal intensity. Even layers of particles so sparsely bound that they are invisible to the eye may provide sufficient catalytic activity for this enhancement method. Optimally the deposited silver, which is generated by in situ reduction of a precursor salt, forms a continuous film and closes the gaps between the captured antigen-antibody-nanoparticle complexes. An increase in signal intensity of up to 13-fold may be achieved thereby. Comparable strategies were employed by, for example, [20, 21]. However, in all three cases, the respective reaction was performed after the actual analyte detection in a secondary step. The silver enhancement solution had to be mixed freshly. Efforts to integrate the enhancement reagents in the assay platform to develop a true one-step device showed that the formulation of Assadollahi et al. was not compatible with the high chloride concentrations often occurring in biologic samples. Silver chloride precipitates formed, which prevented the reduction and precipitation reaction. Accordingly, integrated silver staining demands, first of all, the stabilization of ionic silver in chloride-containing solutions. Furthermore, it must be possible to provide the enhancement reagents, just like the immunoreagents, within the assay platform and store them over a prolonged period of time in this form. Their release, which induces the enhancement reaction, should at best not require additional manipulation by the person performing the assay. It should occur upon or shortly after introduction of the sample into the device. Considering these points a screening of complexing agents and silver staining protocols was performed. Eventually a formulation could be established, which operates stably in the presence of urine. It is entirely based on solid, water-soluble precursors and additives well suited for long-term storage and one-step release. Their performance in the already described REA bioassay system was tested and efficiency and morphology of the respective silver stainings were characterized, as reported herein. It could be demonstrated that the developed formulation is a promising first step towards an integrated enhancement system for nanoparticle-based microfluidic devices.

2. Materials and Methods

2.1. Preparation of REA Chips. A 100 μm thick, aluminum-metalized polyester film (Mitsubishi) was coated with a ~180–220 nm layer of SiO₂ as previously described [8]. (After addition of a metal cluster layer, films of this resonance layer thickness exhibit a pink-violet resonance color, which provides optimal visibility.)

2.2. Streptavidin and Bioassay Reagents. Streptavidin and all reagents required for the bioassay part of the setup (i.e., purified analyte, gold nanoparticle- (AuNP-) conjugated probe, and biotin-tagged analyte binding protein) were kindly provided as a gift. Similar biotin-tagged mediator proteins and AuNP conjugates are available from Sigma-Aldrich (e.g., product number G-0911 or P-6855). For bioassay experiments

AuNP-mediator protein conjugate was used at an OD of ~10.9–11.8 in the final assay mix.

2.3. Streptavidin Coating

2.3.1. Protocol 1 (3-APTES/Streptavidin). A droplet of 3 μL of 2 mg/mL streptavidin in 0.01 M Na-K-phosphate buffer, pH 7.0, was spotted in the middle of a 3-APTES (Sigma-Aldrich) coated chip. The chip was incubated in a wet chamber at RT for 1 h. The chip was washed by shaking in 1x PBS + 0.1% Tween 20 for 3 min. For blocking, the chip was incubated in 2% BSA in 1x PBS + 0.5% Tween 20 for 1 h. The chip was again washed by shaking in 1x PBS + 0.1% Tween 20 for 3 min, rinsed with dH_2O , and used directly for immunodetection.

2.3.2. Protocol 2 (PEI/Streptavidin). A REA chip was coated with PEI (1.6 MDa) by incubation in 10% aqueous PEI solution. A 3 μL droplet of 2 mg/mL streptavidin in 0.01 M Na-K-phosphate buffer, pH 7.0, was spotted in the middle of the PEI-coated chip. The chip was incubated in a wet chamber at RT for 1 h. Washing and blocking were performed as described in protocol 1.

2.3.3. Protocol 3 (3-APTES/Activated CMC Na-Salt/Strep-tavidin). CMC sodium salt (~700 kDa), carbodiimide, and NHS were all purchased from Sigma-Aldrich. 0.45% (w/v) CMC Na-salt in 0.01 M Na-K-phosphate buffer, pH 7.0, was activated with 200 μM carbodiimide and 50 μM NHS end-to-end rotating at RT for 2 h. ~100–200 μL of the solution was spread on the surface of a 3-APTES-coated chip. The chip was incubated for 30 min in a wet chamber, rinsed with dH_2O , and dried. A 3 μL droplet of 2 mg/mL streptavidin in 0.01 M Na-K-phosphate buffer, pH 7.0, was spotted in the middle of the CMC-coated chip. The chip was incubated in a wet chamber at RT for 17–17.5 h. Washing and blocking were performed as described in protocol 1.

2.3.4. Protocol 4 (3-APTES/CMC Na-Salt-Streptavidin Conju-gate). 0.45% (w/v) CMC Na-salt in 0.01 M Na-K-phosphate buffer, pH 7.0, was activated with 200 μM carbodiimide and 50 μM NHS end-to-end rotating at RT for 2 h. Activated CMC was diluted in 0.01 M Na-K-phosphate buffer, pH 7.0, and mixed with streptavidin solution to yield final concentrations of 0.225% (w/v) CMC Na-salt and 2 mg/mL streptavidin. The solution was incubated at RT for 17–17.5 h. 3 μL of the solution was spotted onto a 3-APTES-coated chip. The chip was incubated in a wet chamber for 30 min. Washing and blocking were performed as described in protocol 1.

2.4. Analyte Detection via Microfluidic Assay. Instead of biological samples a standard solution of purified analyte was used. To exclude artifacts that could have resulted from incomplete dissolution of and mixing with the assay reagents (AuNP-conjugated probe, biotin-tagged analyte binding protein, and further additives) the analyte solution was premixed with the respective reagents and incubated briefly before application to the microfluidic cell. Experiments were performed with such assay reagent mixes with an analyte

concentration of 342 ng/mL since this was close to the detection limit of the most sensitive chip variants tested. Thus, it allowed distinguishing competitive from less successful immobilization approaches. The chip was placed in a microfluidic cell, the streptavidin-coated side facing a single channel of a width of 6–7 mm and a height of 5–15 μm . The analyte was premixed with the assay reagents, incubated at RT for 1 min, and applied to the microfluidic cell. After 3 min reaction time the assay was stopped by rinsing the chip with dH_2O . The chip was dried and the NP binding density was characterized.

2.5. Silver (Ag) Enhancement. PdNP-conjugated probe and standard human urine were kindly provided as a gift. For grafting the PdNP conjugate was used at an OD of ~30. L-Ascorbic acid (Ph. Eur.) and sodium hydroxide were purchased from Sigma-Aldrich, sodium thiosulfate pentahydrate was purchased from Carl Roth, citric acid was purchased from Merck Chemicals, and silver nitrate was purchased from Ögussa. Ag enhancement tests were performed with the same microfluidic setup as used for the analyte detection experiments described in Section 2.4.

For determination of the maximum enhancement factor of the established formulation the silver enhancement solution was freshly prepared for each test from stock solutions. Standard human urine was used as solvent. The working concentrations in the enhancement solution were 7.5 mM citric acid, 3 mg/mL NaOH, 2.5 mg/mL sodium thiosulfate, 2.25 mg/mL AgNO_3 , and 6 mg/mL ascorbic acid. Pictures of PdNP-grafted REA chips were taken before Ag enhancement. Then the chips were cut in two in the middle of the grafted area and one half of each chip was subjected to silver enhancement for 2 min. Pictures were taken and the efficiency of the silver enhancement was determined as described in Section 2.7.

2.6. Grafting of REA Chips with PdNP Conjugate. REA chips were coated with PEI using 1%, 10%, or 50% PEI solution in dH_2O to control PdNP-conjugate surface coverage. (Higher PEI concentration in the coating solution results in a higher capacity of the PEI coating to bind the NP conjugate.) PEI-coated REA chips were spotted with 2 μL PdNP-mediator protein conjugate solution and incubated for 1.5 min in a wet chamber. Excess PdNP conjugate was removed by rinsing with dH_2O .

2.7. Image Acquisition, Image Processing, and Quantification of Signal Intensity. To investigate immobilization homogeneity, NP-analyte complex binding capacity, and extent of silver enhancement, it was necessary to measure VIS-light absorption at individual spots of the prepared chips. We found that conventional spectrophotometry was not suited for this purpose. Instead, photos of all chips were taken with a digital camera at constant angle, constant distance, and constant illumination. Image processing software was used to subject all photos to a white correction. For quantification the color profile of the photos was converted to grayscale (8-bit). To evaluate the efficiency of the screened streptavidin immobilization protocols the gray value (in % black, i.e., black =

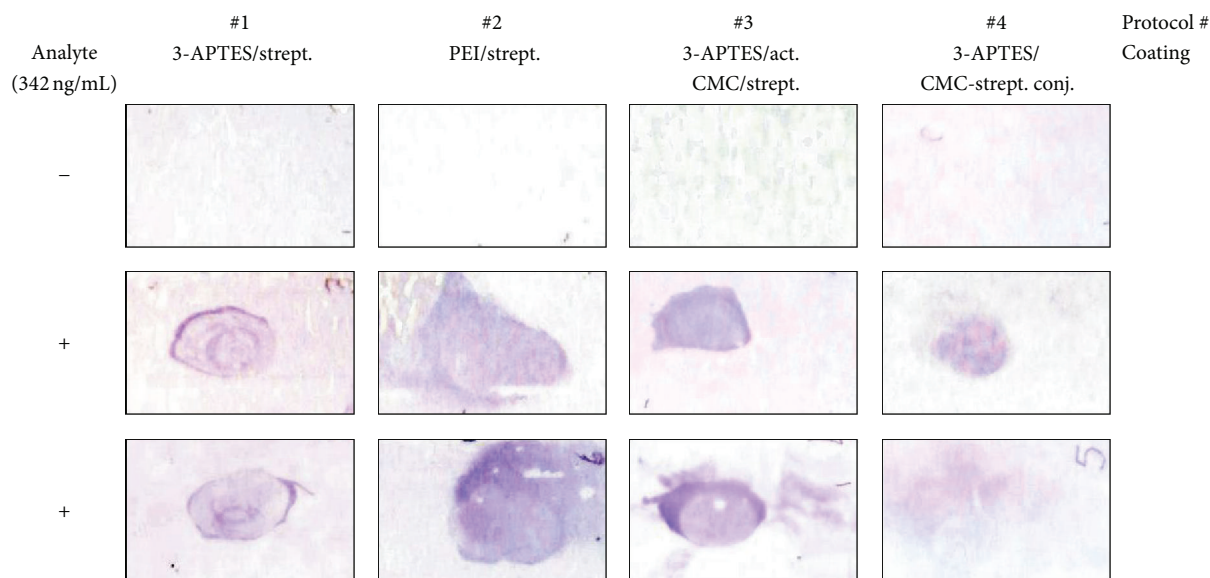


FIGURE 2: Streptavidin immobilization: protocols 1–4. After coating REA chips according to protocols 1–4, the chips were tested in a microfluidic cell with premixed assay reagent solution of constant analyte concentration (342 ng/mL, indicated by “+”). To analyze whether chips exhibited unspecific binding, instead of analyte solution the corresponding pure buffer was added to the assay reagent mix (–).

100%, white = 0%) of 4 spots in the center and 4 spots in the rim of the spotted area and 4 spots in the noncoated area (= background) was determined for each chip. The term “rim” herein refers to the more or less continuous, ring shaped structure at the outline of the spotted area of some chips, which clearly differed from the central region (= center) due to higher signal intensity (see, e.g., Figure 3(a), top row). Such ring structures were typically encountered on chips coated according to protocol 1. If no such structure was present or if it could not be clearly distinguished from the central area (see, e.g., Figure 3(a), second row), the outmost region of the spotted area within 0.5 mm from the outline was considered as rim instead. (The typical diameter of the spotted area ranged from 5 to 8 mm.) Smear patterns, as described in Section 3.1., were not considered in the quantification if they could be clearly distinguished (due to position, shape, and color intensity) from the spotted area, the rim, and the background. Average values for REA color intensity at rim, center, and background were calculated for each chip individually. The background gray intensity was subtracted from the values calculated for rim and center. Then the average values of all chips of one protocol were used to calculate overall average signal intensities and corresponding standard deviations for the individual protocols. For the determination of the enhancement factor of the developed silver enhancement protocol, the gray value (in % black) at two positions in the PdNP-spotted area of each chip was determined before Ag enhancement. The background signal was determined as described for the streptavidin immobilization tests. After Ag enhancement the gray value at the same two positions and the background signal were determined. After background subtraction the enhancement factor (EF), that is, the ratio of the gray values before and after Ag enhancement, was calculated.

2.8. *AFM Imaging.* AFM imaging of bare polymer-coated REA chips, chips grafted with PdNP conjugate, and PdNP-conjugate grafted chips after Ag enhancement was performed using a TT-AFM WORKSHOP system with a 15 μm scanner and a Minus-K-vibration-isolation table in contact mode (SICONA-10 cantilevers).

3. Results and Discussion

3.1. *Streptavidin Immobilization.* Coating protocol 1, that is, adsorption of streptavidin to a 3-APTES-coated surface, resulted in high NP-analyte complex binding capacity at the outer rim of the spotted area (see Figures 2 and 3). In contrast, the spot center showed weak REA signal intensity suggesting a low streptavidin surface density. The phenomenon was described earlier in the context of protein microarrays and is supposed to be caused by the selective diffusion of proteins in droplets of protein solutions to the air-solvent interface [22]. In experiments with other capture proteins we observed that the effect decreased with increasing protein concentrations (>4 mg/mL) and was practically abolished at a protein concentration of 8 mg/mL (unpublished data). Deng et al. [22] reported that the addition of detergent to the spotting solution could suppress ring formation in a covalent immobilization approach. However, there are concerns that such additives may interfere with adsorption processes and may thereby reduce the overall immobilization efficiency of adsorptive methods.

Chips coated by adsorption of streptavidin to a monolayer of high molecular weight PEI (protocol 2) exhibited a significantly higher NP-analyte complex binding capacity in the center of the spotted area (Figures 2 and 3) than protocol 1 chips, but weak ring formation was also observed. Additionally, at one side of the spotted area the chips generally showed

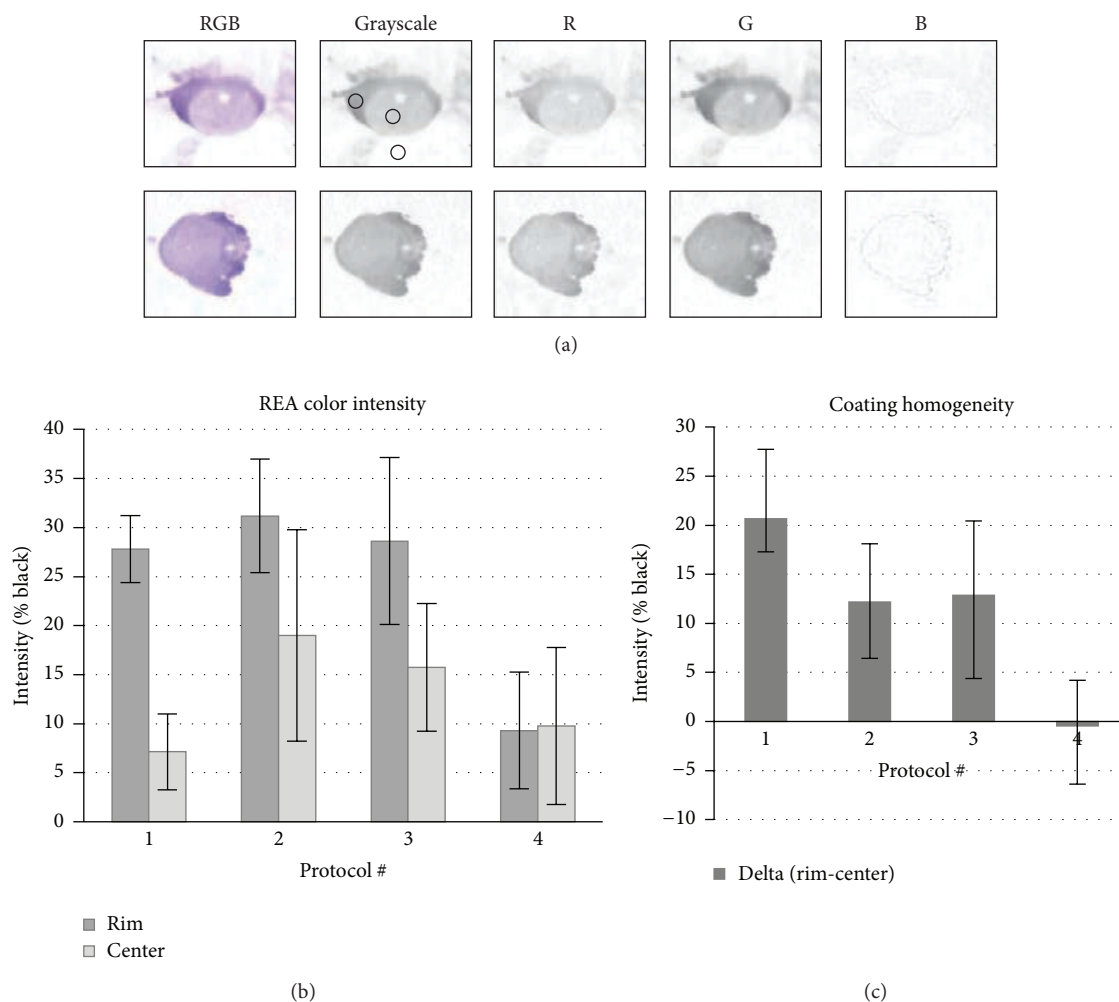


FIGURE 3: Quantification of REA signal intensity. (a) Photos of REA chips after analyte detection are shown. For quantification the color profile of the images was converted to grayscale (8-bit) and the gray values at rim and center of the spotted area as well as the value of the background were determined (indicated by black circles; for more details, see Section 2). Quantification of the grayscale image was considered to correspond best with the actual REA color intensity and thus was preferred over measuring the contribution of one of the three channels: red (= R), green (= G), and blue (= B). (b) REA color intensities at the rim and center of the spots on the tested chips prepared by protocols 1-4 are shown in % black (black = 100%, white = 0%) (protocols 1 and 2: $n = 4$; protocols 3 and 4: $n = 6$). (c) The differences (delta) of average REA color intensities at rim and center [delta = intensity (rim) – intensity (center)] are shown in % black.

a smear pattern with high signal intensity. Such patterns resulted from the adsorption of streptavidin within the seconds when the spotting solution was washed off the chip. This very brief (unintended) dynamic “application of protein” was apparently more efficient than half an hour of incubation. The effect may be used for other coating techniques but unfortunately complicates spotting methods. Localized spotting of PEI instead of coating the complete chip cannot be employed to yield cleaner spot shapes either, because smearing is also observed here. Thus, when using coating protocol 2 clean circular spots may currently be achieved best by the use of masks. Preliminary experiments on lamination and lacquering techniques for mask application were

performed. The suitability of precut commercial self-adhesive films and a variety of polymer lacquers was investigated. Masking could have improved the reproducibility of the spotting experiments as it would have allowed controlling the size of the contact area between chip and spotted protein solution. However, the tests suggested that components of the analyzed masks could interfere with structure or adsorptive properties of the polymer coatings used for immobilization herein. As such effects could not be excluded for any of the examined masking techniques we refrained from using masking in the present study. Structuring of the chip surface to create physical borders for the spotted solution, that is, by laser engraving, was also considered. But any kind of

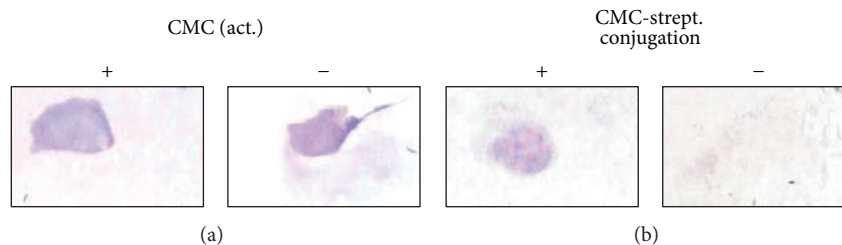


FIGURE 4: Control experiments: protocols 3 and 4. (a) REA chip coated with streptavidin according to protocol 3 (left). 3-APTES-coated REA chip spotted with 2 mg/mL streptavidin solution and incubated at RT in a wet chamber for 17.5 h (right). Analyte detection was performed on both chips. AuNP-analyte complex binding capacity and the homogeneity of the binding were comparable. (b) REA chip coated with streptavidin according to protocol 4 (left). 3-APTES-coated REA chip spotted with 2 mg/mL streptavidin + 0.225% CMC in 0.01% Na-K-phosphate buffer, pH 7.0, and incubated at RT in a wet chamber for 30 min (right). Analyte detection was performed on both chips. The chip coated according to protocol 4 exhibited significantly higher AuNP-analyte complex binding.

chip surface structuring also affects the flow of the detection solution in the microfluidic test setup. This generally strongly interferes with the performance of the assay leading to artifacts. It must therefore be stated that there is currently no means to control the spot size in the studied immobilization techniques. However, spotting experiments were performed as reproducibly as possible. A defined volume of protein solution was spotted on each chip in the same way and the same area was covered during spotting. In the course of the subsequent incubation, the spotted solution tended to spread over the surface as a result of the hydrophilic properties of the chip surface. However, the extent of spreading was always comparable on chips of the same type (i.e., either pronounced (on PEI) or insignificant (e.g., on 3-APTES)). Thus, the sizes of spots created with the same immobilization technique were not significantly different. The conformation of PEI and PEI derivative molecules in SAMs may be determined by adjusting pH and salt concentration of the employed PEI solutions [23]. However, coating with 10% high molecular weight PEI in dH₂O already allows creating layers of highly globular molecules. Therefore we doubt that the structure or the charge density of the PEI base layer can be significantly optimized further. Solutions of much higher PEI concentrations are not useful for monolayer self-assembly, because their viscosity makes intense washing necessary. It has been observed that this can inflict considerable washing defects to the monolayer.

Layer-by-layer coating of 3-APTES and CMC followed by carbodiimide-mediated covalent protein immobilization (protocol 3) yielded spots with considerably high NP-analyte complex binding capacity. Ring formation was occasionally observed but was in general less pronounced than on chips coated according to protocol 1. However, the requirement of the CMC interlayer is doubtful. By incubation of streptavidin on 3-APTES-coated chips without CMC interlayer for 17.5 h protein coatings with very good NP-analyte capture ability could be created. The results were practically indistinguishable from the chips coated according to protocol 3 (see Figure 4(a)). In both approaches commonly thickening of the spotted coating solution occurred due to evaporation during incubation and in some cases even gel formation was

observed. Most probably this led to increased protein concentrations in the coating solutions allowing more homogeneous immobilization, supposedly by unspecific adsorption rather than by covalent binding. However, protein immobilization via drying is generally not recommended. On the one hand, it bears the risk of protein denaturation. On the other hand, experiments with nitrocellulose coated chips showed that fast drying of the spotted solution entails deposition of salts (buffer components), which interferes with adsorptive immobilization and thus prevents homogeneous protein coating.

Protein immobilization protocol 4, conjugation of streptavidin to CMC in solution followed by monolayer self-assembly of the conjugate, is significantly less efficient and less reproducible than the three previously discussed approaches. Streptavidin immobilization is occasionally highly localized but sometimes the streptavidin binding sites appear to be distributed over large areas of the chip in a smear pattern. In a control experiment the CMC-streptavidin conjugate solution was replaced by a mix of nonconjugated CMC and streptavidin at the same concentrations and coating according to protocol 4 was performed. The resulting chips exhibited no visible NP-analyte complex binding capacity (see Figure 4(b)). Adsorption of free streptavidin molecules was obviously prevented by competition with CMC for positively charged groups on the chip surface. It can be concluded that streptavidin immobilization via protocol 4 is not the result of mere adsorption of streptavidin molecules. Efficient CMC-streptavidin cross-linking is critical for this approach and variations in the extent of CMC-streptavidin cross-linking in solution might be the reason for the poor reproducibility of this method.

3.2. Chloride-Resistant In Situ Silver Enhancement. In search of silver staining reagents with good performance in chloride-containing solutions several established protocols and known complexing agents for silver salts were screened including Tris base and histidine. Primarily, reagents were considered, which exhibit good solubility in aqueous solutions. This is most critical for the establishment of a robust in situ enhancement technology as all reagents have to be provided

in the assay platform in a stable form (preferably dry) and it must be possible to release them by addition of the sample without significant further manipulation of the test device. Regarding the stabilization of silver ions against precipitation with chloride, most promising results were achieved by the use of sodium thiosulfate. It was found that silver nitrate could be dissolved in a human urine sample (with a typical chloride concentration of 20 mM) by buffering it with citrate and addition of sodium thiosulfate to a concentration roughly equivalent to the desired molar silver nitrate content. At $\text{pH} < 7$ such a solution was found to be stable for at least 1 h. For Ag enhancement the mixture had to be activated by addition of a reducing agent. Glucose and ascorbic acid were considered as potential candidates here because both easily and quickly dissolve in water. Finally ascorbic acid was selected for it allowed good control of the reduction reaction. It was further observed that the efficiency and speed of the silver enhancement process and the stability of the solution strongly depended on the pH value. We were interested in a fast enhancement process and therefore optimized an alkaline formulation (see Section 2). Eventually, a silver enhancement protocol could be established, which employs exclusively highly water-soluble reagents that can all be provided in an assay device in dry form: thiosulfate, citric acid, and sodium hydroxide for stabilization and buffering and ascorbic acid as reducer. The efficiency of the developed formulation should be characterized on REA chips sparsely grafted with catalytic metal nanoparticles. Already at the start of the screening it had turned out that the AuNP-conjugated probe employed for the screening of streptavidin immobilization techniques did not act as good catalyst for silver reduction (independent of the tested enhancement protocol). The AuNP conjugate was strongly stabilized against precipitation and unspecific binding (by inert proteins and polymers) which might have suppressed its interaction with the silver enhancement reagents. Therefore a less shielded PdNP conjugate was used instead, which exhibited significantly higher catalytic activity but equivalent performance in bioassay applications. REA chips were precoated with PEI and grafted with PdNP conjugate by spotting. Chips with low, medium, and high PdNP density were created. The silver enhancement reagents were dissolved in urine and the PdNP-grafted REA chips were treated with this solution in a microfluidic cell for 2 min. The enhancement efficiency was determined by comparing REA color intensities before and after silver staining. (Only chips exhibiting a visible REA color spot before enhancement were considered in the quantification.) It could be demonstrated that the enhancement factor was especially high for weak signals, that is, if the PdNP density on the chip was low. Even very sparse and therefore invisible PdNP coatings exhibited a clearly visible REA color after treatment of the corresponding chip with the enhancement solution (Figure 5(a)). At low PdNP surface coverage an enhancement factor of up to 13 was observed (Figure 5(b)). With increasing PdNP density the signal enhancing effect decreased logarithmically. However, this is not considered too critical because visibility of the REA signal was already good for those PdNP coatings even before enhancement. AFM imaging revealed that the precipitated silver layer is not smooth but rather crystalline.

This also resulted in increased light scattering under very bright illumination, which was not observed in the PdNP-grafted areas before enhancement. Generally the crystalline morphology is not problematic and does not diminish the signal enhancing effect of the silver coating. However, it is an indication that the enhancement reaction still requires fine tuning. Optimally stabilized silver enhancement yields slightly granular to smooth surfaces. Nevertheless, the performance of the developed silver enhancement formulation is competitive and, most importantly, it fulfills all requirements for the integration into microfluidic devices.

4. Conclusions

4.1. Streptavidin Immobilization. Four different protocols for streptavidin immobilization on REA chips could be established and optimized. The techniques employ different chemistry and are based on two different immobilization approaches: adsorption and covalent immobilization, respectively. They were compared regarding coating homogeneity and analyte capture capacity of the prepared protein layers. It was found that by adsorption to a monolayer of high molecular weight PEI the most homogeneous coatings could be generated within a short time. Thus, this method may be best suited for large scale chip manufacture. The only drawback of the approach was smear formation, which prevented the grafting of well-shaped protein spots. By addition of blocking agents to the washing solutions or by use of a mask such random adsorption during the washing step effect may possibly be suppressed. Covalent immobilization to CMC monolayers (protocol 3) also yielded good results but turned out to be much more time consuming. Furthermore, control experiments suggested that immobilization was achieved at least in part by unspecific adsorption rather than by covalent binding and that the CMC base layer was not strictly required. In general, it was observed that linkers with pronounced 3D structure are not absolutely necessary to generate protein layers with occasionally high analyte binding capacity. However, precoating with charged polymers significantly accelerated adsorption of proteins with opposite charge and has the potential to significantly improve capture protein density and coating homogeneity if short immobilization times are required.

4.2. Chloride-Resistant In Situ Silver Enhancement. Silver enhancement reagents could be identified, which operate even in the presence of chloride and can thus be employed for silver staining in samples such as urine, blood, or saliva. All required reagents are water soluble and can be provided in dry form in a microfluidic cell. They can be released upon sample addition (preferably with delay) to react with the captured analyte-nanoparticle complexes on the REA chip and enhance the assay signal. Initial tests in this context have already been performed. For this purpose the enhancement reagents were dried on hydrophilized polymer fleeces and integrated into a laser-structured microfluidic cell as described in Assadollahi et al. [8]. Although mixing of the reagents was not optimal, good signal enhancement could

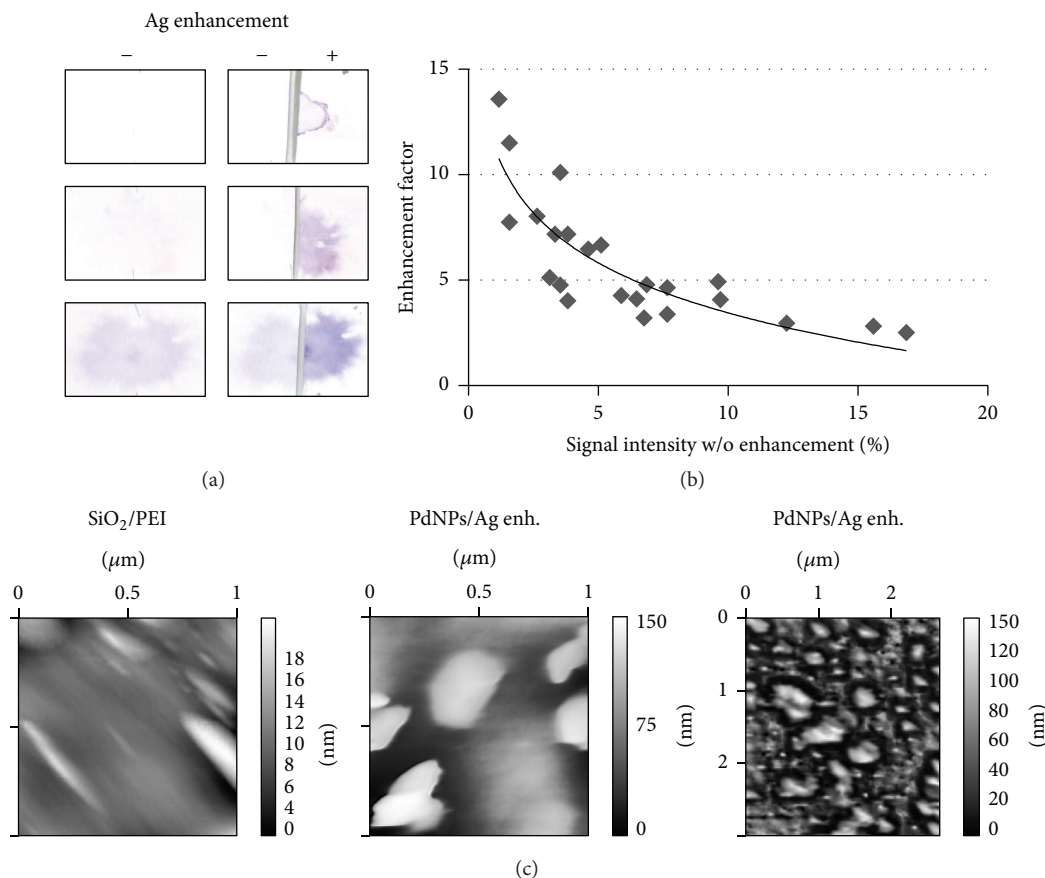


FIGURE 5: Thiosulfate-stabilized silver enhancement. (a) PEI-coated REA chips grafted with PdNP-conjugated probe (low, medium, and high surface coverage) before Ag enhancement (–) (left). The chips were cut in two and one half of each chip was subjected to Ag enhancement (+) (right). (b) The enhancement factor (EF) strongly depended on the signal intensity before silver enhancement (i.e., the PdNP coverage density) ($EF = [\text{signal after Ag enhancement in \% black}]/[\text{signal before Ag enhancement in \% black}]$). (c) AFM scans of REA chips before PdNP grafting (left) and after PdNP grafting and Ag enhancement (middle and right) (the grafted PdNP conjugate could not be imaged due to the inherent roughness of the chip surface and the polymer layer and the small size of the PdNPs of ≤ 20 nm.).

be achieved. Thus, optimization of release and mixing of the reagents will be the focus of future efforts towards this kind of integrated enhancement system.

Conflict of Interests

The authors declare that there is no conflict of interests regarding the publication of this paper.

Acknowledgment

The authors want to thank the Austrian government for supporting part of this work by a scientific grant of the FFG-Bridge program.

References

- [1] K. N. Han, C. A. Li, and G. H. Seong, "Microfluidic chips for immunoassays," *Annual Review of Analytical Chemistry*, vol. 6, pp. 119–141, 2013.
- [2] C. A. Baker, C. T. Duong, A. Grimley, and M. G. Roper, "Recent advances in microfluidic detection systems," *Bioanalysis*, vol. 1, no. 5, pp. 967–975, 2009.
- [3] A. Leitner, Z. Zhao, H. Brunner, F. R. Aussenegg, and A. Wokaun, "Optical properties of a metal island film close to a smooth metal surface," *Applied Optics*, vol. 32, no. 1, pp. 102–110, 1993.
- [4] T. Schalkhammer, "Metal nano clusters as transducers for bioaffinity interactions," *Monatshefte für Chemie*, vol. 129, no. 10, pp. 1067–1092, 1998.
- [5] G. Bauer, F. Pittner, and T. Schalkhammer, "Metal-nano-cluster biosensors," *Mikrochimica Acta*, vol. 131, no. 1-2, pp. 107–114, 1999.
- [6] C. Mayer, N. Stich, R. Palkovits, G. Bauer, F. Pittner, and T. Schalkhammer, "High-throughput assays on the chip based on metal nano-cluster resonance transducers," *Journal of Pharmaceutical and Biomedical Analysis*, vol. 24, no. 5-6, pp. 773–783, 2001.
- [7] M. Bauer, J. Haglmüller, F. Pittner, and T. Schalkhammer, "Direct optical visualization of DNA–DNA interaction by nanoparticle-capture on resonant PET-films," *Journal of*

- Nanoscience and Nanotechnology*, vol. 6, no. 12, pp. 3671–3676, 2006.
- [8] S. Assadollahi, C. Reininger, R. Palkovits, P. Pointl, and T. Schalkhammer, “From lateral flow devices to a novel nano-color microfluidic assay,” *Sensors*, vol. 9, no. 8, pp. 6084–6100, 2009.
- [9] R. Palkovits, M. Schlauf, S. Assadollahi, P. Pointl, T. Trapichler, and T. Schalkhammer, “Development of a microfluidic-based lateral flow immunoassay for the detection of human serum albumin,” in *Proceedings of the 9th International Conference on Multi-Material Micro Manufacture*, pp. 159–162, Vienna, Austria, October 2012.
- [10] C.-H. Yeh, C.-Y. Hung, T. C. Chang, H.-P. Lin, and Y.-C. Lin, “An immunoassay using antibody-gold nanoparticle conjugate, silver enhancement and flatbed scanner,” *Microfluidics and Nanofluidics*, vol. 6, no. 1, pp. 85–91, 2009.
- [11] H.-C. Lin, I.-L. Wang, H.-P. Lin, T. C. Chang, and Y.-C. Lin, “Enhancement of an immunoassay using platinum nanoparticles and an optical detection,” *Sensors and Actuators B: Chemical*, vol. 154, no. 2, pp. 185–190, 2011.
- [12] J. Wen, X. Shi, Y. He, J. Zhou, and Y. Li, “Novel plastic biochips for colorimetric detection of biomolecules,” *Analytical and Bioanalytical Chemistry*, vol. 404, no. 6-7, pp. 1935–1944, 2012.
- [13] J.-G. Walter, F. Stahl, M. Reck et al., “Protein microarrays: reduced autofluorescence and improved LOD,” *Engineering in Life Sciences*, vol. 10, no. 2, pp. 103–108, 2010.
- [14] P. Jonkheijm, D. Weinrich, H. Schröder, C. M. Niemeyer, and H. Waldmann, “Chemical strategies for generating protein biochips,” *Angewandte Chemie—International Edition*, vol. 47, no. 50, pp. 9618–9647, 2008.
- [15] C. D. Hodneland, Y.-S. Lee, D.-H. Min, and M. Mrksich, “Selective immobilization of proteins to self-assembled monolayers presenting active site-directed capture ligands,” *Proceedings of the National Academy of Sciences of the United States of America*, vol. 99, no. 8, pp. 5048–5052, 2002.
- [16] V. Dugas, A. Elaissari, and Y. Chevalier, “Surface sensitization techniques and recognition receptors immobilization on biosensors and microarrays,” in *Recognition Receptors in Biosensors*, M. Zourob, Ed., pp. 47–134, Springer, New York, NY, USA, 2010.
- [17] B. C. C. Pessela, L. Betancor, F. Lopez-Gallego et al., “Increasing the binding strength of proteins to PEI coated supports by immobilizing at high ionic strength,” *Enzyme and Microbial Technology*, vol. 37, no. 3, pp. 295–299, 2005.
- [18] E. O. V. Fundador, V. C. Sabularse, and M. A. J. R. Revilleza, “Immobilization of invertase on carboxymethylcellulose prepared from nata de coco for the inversion of sucrose,” *ASEAN Journal for Science and Technology Development*, vol. 20, no. 1, pp. 37–47, 2003.
- [19] S. K. Kufer, H. Dietz, C. Albrecht et al., “Covalent immobilization of recombinant fusion proteins with hAGT for single molecule force spectroscopy,” *European Biophysics Journal*, vol. 35, no. 1, pp. 72–78, 2005.
- [20] Y. Lu, W. Shi, J. Qin, and B. Lin, “Low cost, portable detection of gold nanoparticle-labeled microfluidic immunoassay with camera cell phone,” *Electrophoresis*, vol. 30, no. 4, pp. 579–582, 2009.
- [21] H. Schroeder, M. Adler, K. Gerigk, B. Müller-Chorus, F. Götz, and C. M. Niemeyer, “User configurable microfluidic device for multiplexed immunoassays based on DNA-directed assembly,” *Analytical Chemistry*, vol. 81, no. 3, pp. 1275–1279, 2009.
- [22] Y. Deng, X.-Y. Zhu, T. Kienlen, and A. Guo, “Transport at the air/water interface is the reason for rings in protein microarrays,” *Journal of the American Chemical Society*, vol. 128, no. 9, pp. 2768–2769, 2006.
- [23] T. Trimaille, C. Pichot, and T. Delair, “Surface functionalization of poly(D,L-lactic acid) nanoparticles with poly(ethylenimine) and plasmid DNA by the layer-by-layer approach,” *Colloids and Surfaces A: Physicochemical and Engineering Aspects*, vol. 221, no. 1–3, pp. 39–48, 2003.

Research Article

Focused Ion Beam Assisted Interface Detection for Fabricating Functional Plasmonic Nanostructures

Houxiao Wang,^{1,2,3} Wei Zhou,^{2,3} and Er Ping Li³

¹School of Mechanical Engineering, Jiangsu University, 301 Xuefu Road, Zhenjiang 212013, Jiangsu, China

²School of Mechanical and Aerospace Engineering, Nanyang Technological University, 50 Nanyang Avenue, Singapore 639798

³Advanced Photonics and Plasmonics Division, A*STAR Institute of High Performance Computing,
1 Fusionopolis Way, No. 16-16 Connexis, Singapore 138632

Correspondence should be addressed to Houxiao Wang; wanghx@ujs.edu.cn and Wei Zhou; mwzhou@ntu.edu.sg

Received 24 January 2015; Accepted 8 April 2015

Academic Editor: Zhida Xu

Copyright © 2015 Houxiao Wang et al. This is an open access article distributed under the Creative Commons Attribution License, which permits unrestricted use, distribution, and reproduction in any medium, provided the original work is properly cited.

Plasmonic nanoscale devices/structures have gained more attention from researchers due to their promising functions and/or applications. One important technical focus on this rapidly growing optical device technology is how to precisely control and fabricate nanostructures for different functions or applications (i.e., patterning end points should locate at/near the interface while fabricating these plasmonic nanostructures), which needs a systematic methodology for nanoscale machining, patterning, and fabrication when using the versatile nanoprecision tool focused ion beam (FIB), that is, the FIB-assisted interface detection for fabricating functional plasmonic nanostructures. Accordingly, in this work, the FIB-assisted interface detection was proposed and then successfully carried out using the sample-absorbed current as the detection signal, and the real-time patterning depth control for plasmonic structure fabrication was achieved via controlling machining time. Besides, quantitative models for the sample-absorbed currents and the ion beam current were also established. In addition, some nanostructures for localized surface plasmon resonance biosensing applications were developed based on the proposed interface detection methodology for FIB nanofabrication of functional plasmonic nanostructures. It was shown that the achieved methodology can be conveniently used for real-time control and precise fabrication of different functional plasmonic nanostructures with different geometries and dimensions.

1. Introduction

Some methods and systems, for example, nanoimprinting lithography [1, 2], electron beam lithography [3–5], etching (reactive ion etching and dry etching) [6–10], femtosecond laser [11], interference lithography [12], and focused ion beam (FIB) [13–16], have been reported to develop optical structures or devices (e.g., specific functional plasmonic nanostructures). Compared with these reported methods and systems, despite the potential drawbacks of surface damage caused by high-energy ion beam irradiation and relatively limited processing speed for large-area high-density structural patterns [6, 13], the FIB has its strength in one-step maskless simpler, more flexible, and better-controlled nanoprecision machining, patterning, and fabrication especially for submicron, nanoscale, or subwavelength various functional samples or structures via ion beam induced

milling, etching, and deposition due to its advantages of large depth of focus, high resolution, patterning flexibility, and direct-writing capability [6, 13–17]. The FIB system has been widely used in the fields of semiconductor, micro- and nanoelectronics including integrated-circuit modification and failure analysis, mask repairing, sample preparation for transmission electron microscopy (TEM), biomedicine, and micromachining [18]. Recently, the FIB nanoprecision machining, patterning, and fabrication for specific nanoscale applications have attracted more interest to realize more diversity for nanoconstruction [6, 13–16, 19].

Some metals (e.g., Au, Ag, and Cu) can be deposited on the dielectric substrate (e.g., SiO₂) to develop different functional plasmonic structures/devices, which have gained more and more attention from the researchers due to their promising functions and/or applications because the interface between metal coating and dielectric substrate may

support surface plasmon polaritons (SPPs) [20–22]. Accordingly, the patterning end points should locate at or near the interface while fabricating/developing these plasmonic structures/devices, which requires the interface detection to realize real-time patterning control and precise structure fabrication. However, this rapidly growing optical device technology requires a systematic methodology to precisely control and fabricate the designed nanoscale devices or structures for various industrial and commercial applications even while using the advanced nanoprecision tool FIB. Thus, it is necessary to carry out a systematic study on the FIB-assisted interface detection for nanofabrication of different functional plasmonic nanostructures. Moreover, the rapidly growing applications of FIB in the field of nanomachining, nanopatterning, or nanofabrication especially for the plasmonic device development also require the capability to reliably detect the interfaces between different material layered structures, that is, the end point detection (EPD) for the accurate transition signal from one layer to the next [23, 24]. The EPD technique allowed interaction of ions with sample surface to be monitored through a plot of stage grounding current as a function of ion milling time [25].

During ion milling, the sample-absorbed current, which depends on the beam current and the material-dependent number of the generated secondary electrons and ions, flows to the ground if the specimen is grounded, and it linearly increases with the beam current for the same material and changes with materials for the same beam current used [23, 24]. Because different materials have different characteristic secondary ion yields, it is possible to distinguish the interfaces between different material layers [26]. Thus, various materials can be identified while milling the multilayered structure made up of different materials via monitoring the current flow to the ground and then providing indications of the end points [23, 24, 26–30].

For the plasmonic or multilayered nanostructures, it is important to know whether nanopatterns are formed at or near the interface between different material layers [27]. The end point monitor (EPM) in the FIB system may solve this problem by measuring the sample-absorbed current during the machining process, and the sudden current alteration indicates machining transition from one material layer to another [23, 24, 26–30]. The EPM-detected current signal alters as various material layers for a complex specimen are exposed for removal via the ion beam, and it can be real-time monitored (sample-absorbed current may be continuously monitored during FIB machining or fabrication process through connecting the sample to an electrometer amplifier, and the endpoint detection can be achieved via the detected current signal curve based on the real-time monitor) [23–25]. The real-time EPM current signal curve presents the sample-absorbed current as a function of the machining time [23].

Among the functional plasmonic nanoscale structures or devices, the plasmonic nanobiosensors based on the localized surface plasmon resonance (LSPR) have become more and more important/interesting resulting from their promising functions and wide applications. The LSPR is sensitive to geometric parameters [31]. It is reported that

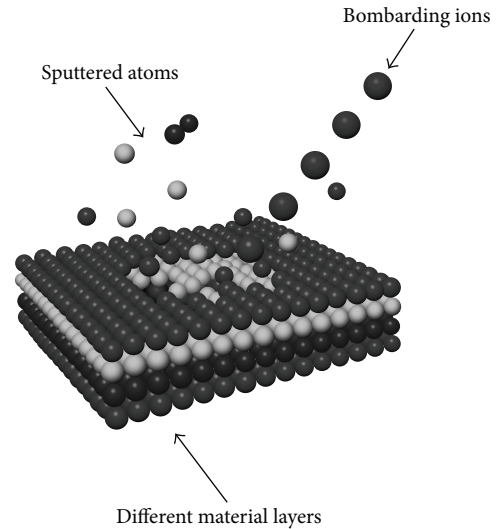


FIGURE 1: Schematic process for focused ion beam nanomachining.

many similar plasmonic nanohole/particle structures (e.g., the rhombic hybrid Au-Ag nanostructures [31], the nanohole array on a Au-deposited glass substrate [32], the Au/Ag nanoparticles [19], the square nanohole array [33], and nanostars [34]) have been applied for LSPR biosensing (e.g., a plasmonic square nanohole array can be used for the real-time sensing/monitoring of protein-protein specific binding interaction using a LSPR nanohole sensor integrated with microfluidic delivery, and the sensitivity of this nanohole sensor depended on the periodicity of the array and the order of the surface plasmon resonance modes) [19, 31–35], and they have been applied for sensing of localized transmission/reflection field intensity distribution [32], refractive index (e.g., sensing of the analytes of glucose water solutions with refractive indexes ranging from 1 to 1.38) [31, 34], and optical spectra (e.g., scattering spectra) [33, 34], and so forth.

So far, few literatures regarding investigation for the interface between different materials during FIB machining or fabrication process have been found, without mentioning the investigation of the interface detection between different materials during FIB machining for nanofabricating the functional plasmonic nanostructures. Different from the previous work regarding the interface detection using the EPD technique, this work has proposed and achieved a systematic methodology and detailed analysis regarding the interface detection for FIB nanofabrication of functional plasmonic nanostructures for biosensing applications through real-time patterning control using the EPM.

2. Materials and Methods

The specimen used consists of a quartz substrate and a very thin silver film layer deposited on the substrate. Figure 1 shows the sketch for the FIB nanomachining, and the material can be removed layer by layer using the high energetic bombarding ions from the focused ion beam.

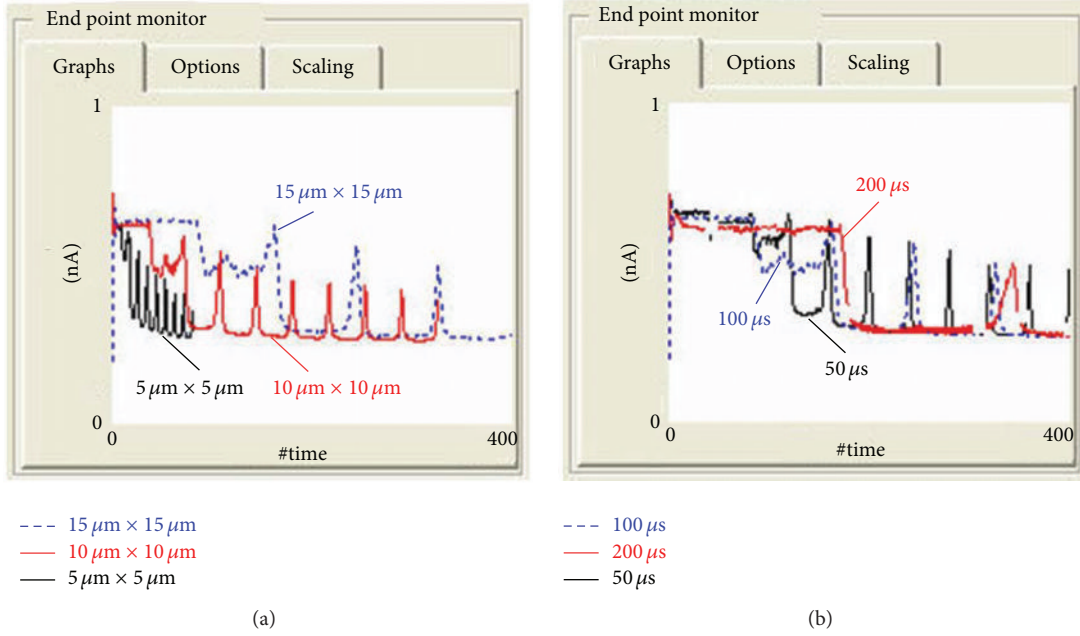


FIGURE 2: Sample-absorbed current versus machining time detected at different (a) milling area and (b) beam dwell time for the interface detection using the EPM.

As shown in Figure 2, the EPM in the FIB system, which collects the specimen-absorbed current as the EPD signal through a real-time monitor and an EPM plot (the sample inside the chamber of FIB system is connected to an electrometer amplifier to monitor the real-time current signal), was used to detect the sample-absorbed current signal for the interface detection assisted by the FIB cross sectioning. Using the EPD technique, the real-time patterning depth control for the plasmonic structure fabrication can be achieved via controlling machining time using the EPM. Table 1 gives the parameters used for the Ag/SiO₂ interface detection.

As shown in Table 1, the defined milling area for the EPM-assisted current signal detection should be relatively large if the machining efficiency is allowed, and 15 μm by 15 μm is selected for a better EPM control (Figure 2). Besides, a relatively high ion beam current (e.g., 0.3 nA) is used to obtain a strong detection signal and increase nanomachining efficiency. Accordingly, the machining time control has been achieved via interface detection using an ion beam current of 0.3 nA, and the ion doses used can be also obtained through the following:

$$\text{Ion dose} = \text{Ion flux} * \text{Milling time},$$

$$\text{Ion flux} = 6.24 \times 10^{18} * \frac{\text{Ion beam current}}{\text{Milling area}}, \quad (1)$$

$$\text{Milling area} = \frac{\text{Defined frame area}}{\cos(\theta)},$$

where θ is the angle between the normal line of the sample surface and the axis of the ion beam (θ can alter when the sample stage tilts).

TABLE 1: Parameters used for Ag/SiO₂ interface detection.

Milling area (μm × μm)	Dwell time (μs)	Current (nA)	Overlap	Ion flux (ions cm ⁻² s ⁻¹)
15 × 15	100	0.3	50%	8.32 × 10 ¹⁴

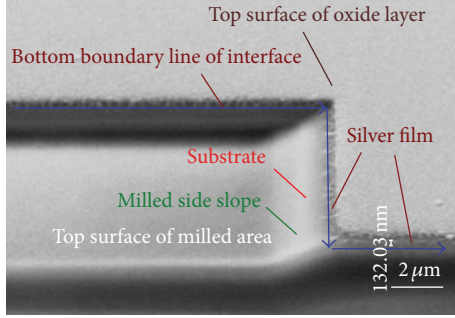
If patterning at or near an interface for a very thin film layer occurs, the ion beam current should be smaller to avoid seriously damaging the film layer surface or the adjacent area. Thus, in this work, the real-time sputtering depth control for the FIB-based actual nanopatterning can be achieved simply and conveniently just through calculation and transformation into sputtering time via selecting a small ion beam current (e.g., 10–100 pA) and calculating the required milling area given a normal incident angle of the ion beam (i.e., $\theta = 0^\circ$) together with the other fixed milling parameters (e.g., overlap and dwell time). Consequently, a better control for the actual nanostructure fabrication can be achieved using this method assisted by the scanning electron microscopy (SEM) and atomic force microscopy (AFM) measurements.

3. FIB-Assisted Interface Detection

It is necessary to measure the thin film thickness and detect the interface between film layer and substrate in order to control patterning formation at/near the interface via the EPM control of the required milling time which may be calculated through the required ion dose. However, it is difficult to measure the film thickness by traditional methods (e.g., optical method based on thin film interference using fiber optics coupled microscope, AFM, ultrasonic pulse-echo technique of ultrasonic gages for measuring the thickness of

TABLE 2: Material-dependent currents measured using the EPM for the same sample.

Beam current (nA)	Ion flux (ions cm ⁻² s ⁻¹)	Material-dependent current (nA)		
		Ag oxide	Ag film	SiO ₂ substrate
0.3	8.32×10^{14}	0.76	0.70	0.3
1.0	3.12×10^{15}	2.73	2.50	1.0

FIGURE 3: The Ag/SiO₂ interface cross section measured using SEM.

coatings on nonmetal substrates, etc.) if the deposited film is too thin (e.g., for the cases less than 100 nm thick). Thus, in this work, the EPM current curve was used as the end point detection signal (i.e., the abrupt transition point of the detected signal curve for the sample-absorbed current versus the milling time during the milling process) to obtain the required ion dose and milling time for the interface detection. The operation procedures related to FIB cross sectioning include rectangle milling, regular cross section, cleaning cross section, and measurement for thin film thickness via SEM imaging for the interface cross section.

Figure 3 shows the Ag/substrate interface cross section detected using the FIB/SEM dual beam system. As shown in Figure 3, the sidewalls of the milled zones are approximately V-shaped due to the Gaussian beam and the redeposition of the sputtered material debris on the sidewalls (the V-shape sidewall formation after FIB milling can be also verified in Figure 4), and the thickness of the Ag film deposited on the glass substrate is around 132 nm.

As shown in Figure 5, there are 9 raster passes in all: the first pass is for sputtering the oxide layer and silver film (see Figure 5(a)); the second pass is for milling transition from Ag film to SiO₂ substrate (see Figure 5(b)); the left passes, as shown in Figure 5(c), are used to mill deep into SiO₂ substrate. Time used for sputtering oxide layer is 3 s. Milling stops in the deposited film material from 3 s to 85 s; at 85 s (ion dose used is 7.07×10^{16} ions cm⁻²), milling just occurs at the Ag/SiO₂ interface boundary, that is, just starting to sputter the substrate material; subsequently, milling occurs in both Ag layer and SiO₂ substrate until 163 s, which is a transition process from film machining to substrate machining. Almost all film material is removed at 163 s when a relatively clean interface (a clean plane interface could be theoretically achieved at this moment if under ideal conditions; however, in this case, the film layer subjected to ion beam irradiation was not absolutely removed evenly, resulting in some nanoscale residues at the

Ag/SiO₂ interface) between the film layer and the substrate is obtained (Figure 6). Afterwards, as shown in Figure 5, milling continues to occur deep into the substrate until 745 s (ion dose used is 6.20×10^{17} ions cm⁻²).

As shown in Figure 6, the deposited film material was not completely sputtered at the “exact” interface; that is, some silver residues may remain at the interface (it should be indicated that the reported EPD accuracy is in the range of a few tens of nanometers which results from the complex interfacial mixing with the ion bombardment depending on beam energy, material properties, crystallographic orientation, substrate surface roughness, and quality of deposited thin films, etc. [23, 24]). Thus, the machining end point could be normally below the “exact” interface to completely sputter the deposited film material. As a result, the sample-absorbed current drops due to dielectric substrate machining (see Figure 5(c)).

4. Material-Dependent Currents Measured during Interface Detection

Material-dependent currents in Table 2 are measured via the EPM signal curves. The detected substrate-absorbed current is equal to the ion beam current used, and the strength of sample-absorbed current signal increases with the ion flux. Under the same machining conditions, compared with the Ag-absorbed current signal, the Ag₂O-absorbed current signal is the strongest and the SiO₂-absorbed current signal is the weakest, resulting from different material-dependent average atomic numbers (material with higher average atomic number can emit more secondary ions/electrons; the atomic numbers for Ag₂O, Ag, and SiO₂ are 232, 108, and 60, resp.), material conductivity, and material sputtering yield for the secondary ions (sputtering yield $Y = \text{ejected atom number/incident ion number}$, i.e., $Y = \rho d/\sigma$, where ρ is the density (atoms cm⁻³), d is the sputtering depth (cm), and σ is the ion dose (ions cm⁻²)).

The detected current signal ratios for $I_{\text{Oxide}}/I_{\text{Film}}$ and $I_{\text{Substrate}}/I_{\text{Film}}$ are approximately constant (Table 3) despite encountering significant changes of ion fluxes and ion beam currents, which actually indicates that the material-dependent current signal ratio detected via the EPM is independent of processing conditions.

The quantitative correlation between the sample-absorbed current I_S and the ion beam current I_B can be approximately expressed as a linear function for the same material which is given as

$$I_S = (1 + K_E - K_I) \times I_B = K \times I_B, \quad (2)$$

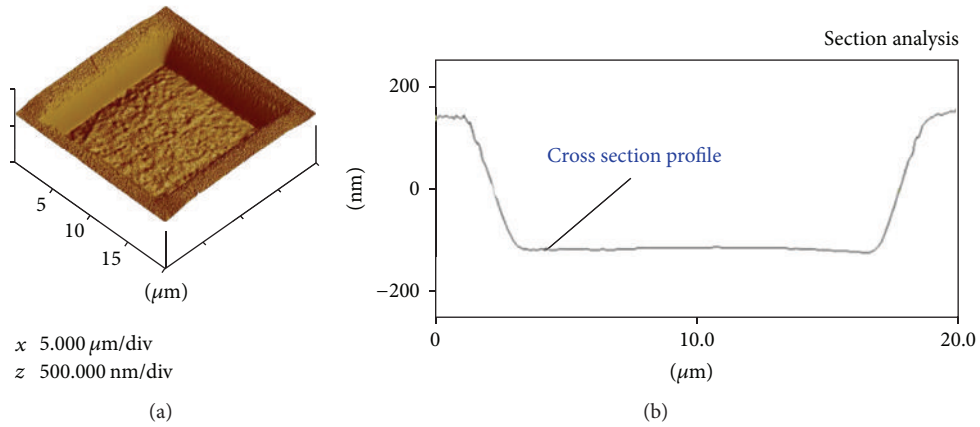


FIGURE 4: (a) 3D view and (b) 2D cross section analysis for the FIB-induced V-shape sidewall measured using AFM.

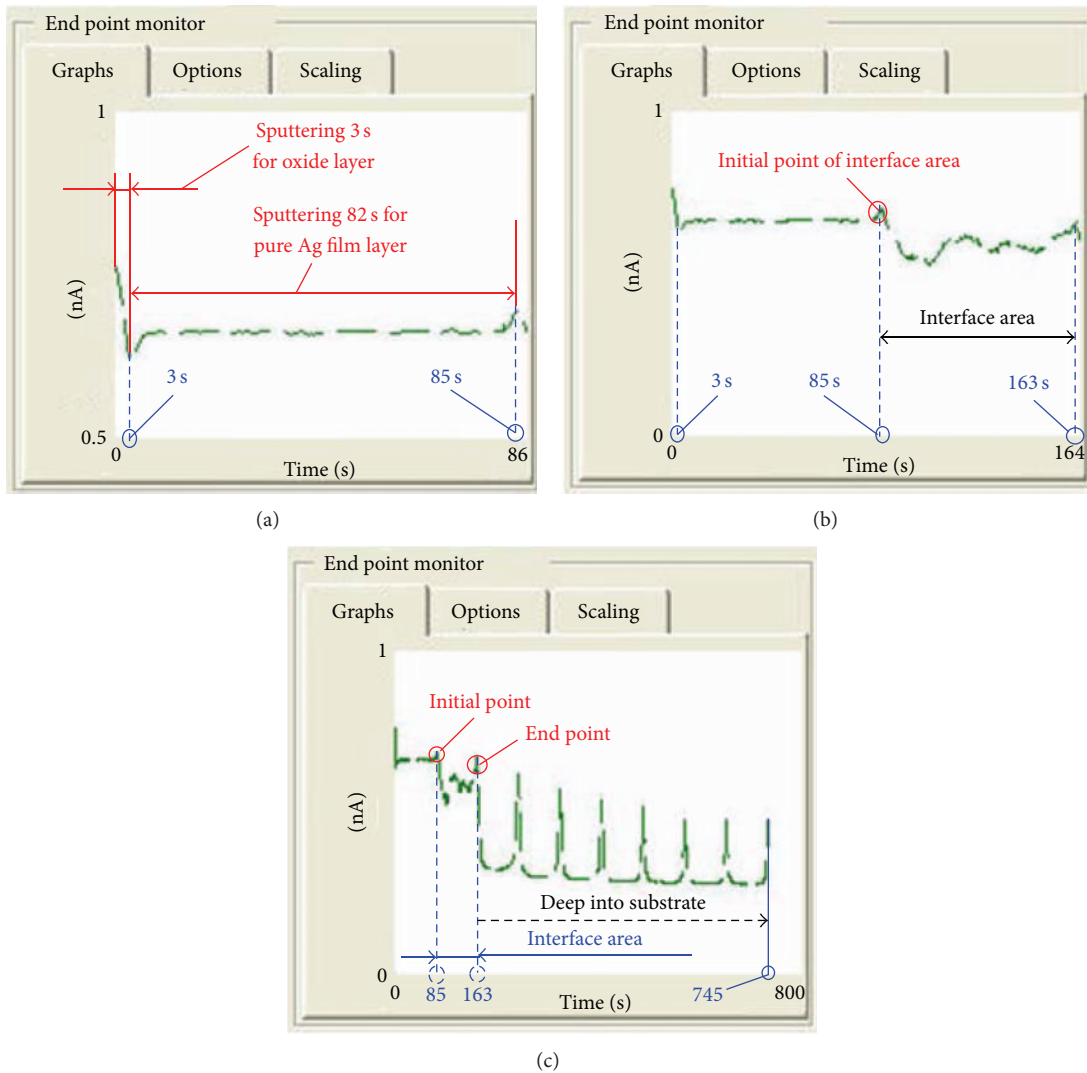


FIGURE 5: Patterning depth control via controlling machining time using the EPM for sputtering the (a) oxide layer and Ag film, (b) Ag/SiO₂ interface, and (c) SiO₂ substrate.

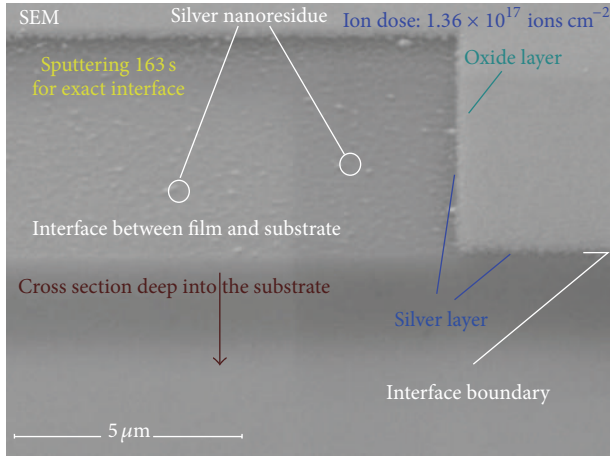


FIGURE 6: The interface detected using FIB/SEM dual beam system after FIB milling 163 s.

TABLE 3: Material-dependent current ratios detected for the same sample.

Ion flux (ions $\text{cm}^{-2} \text{s}^{-1}$)	Material-dependent current signal ratio	
	Oxide/film	Substrate/film
8.32×10^{14}	1.09	0.43
3.12×10^{15}	1.09	0.40

TABLE 4: Linear coefficients for sample-absorbed current and ion beam current.

Ion flux (ions $\text{cm}^{-2} \text{s}^{-1}$)	K		
	Ag oxide	Ag film	SiO ₂ substrate
8.32×10^{14}	2.53	2.33	1.0
3.12×10^{15}	2.73	2.50	1.0

TABLE 5: Linear coefficients for sample-absorbed current and ion beam current.

Sample materials	Ag oxide	Ag film	SiO ₂ substrate
Average value of K	2.63	2.42	1.0

where K_E and K_I denote the coefficients for electrons and ions, respectively, and $K = 1 + K_E - K_I$.

The values of K for Ag oxide, Ag film, and SiO₂ substrate can be determined through the detected sample-absorbed currents (Tables 2 and 4). Table 5 lists the average values of K for Ag oxide, Ag film, and SiO₂ substrate, which is achieved through the data in Table 4. Thus, for the case of FIB milling the quartz substrate with the deposited Ag film, the quantitative expressions for the sample-absorbed currents and ion beam current can be given as

$$\begin{aligned}
 I_{\text{Ag}_2\text{O}} &= 2.63 \times I_B, \\
 I_{\text{Ag}} &= 2.42 \times I_B, \\
 I_{\text{SiO}_2} &= I_B.
 \end{aligned} \tag{3}$$

5. Plasmonic Nanostructure Development Based on Interface Detection

The successful detection for the interface between coated metal and dielectric substrate is important to the next step to fabricate functional plasmonic structures, and the real-time patterning depth control of functional plasmonic structure fabrication using relatively small ion beam currents has also been achieved through controlling milling time when the ion dose for fabricating the plasmonic structure is obtained after the interface detection; that is, through interface detection for the Ag-deposited substrate with a multilayer structure, the end point detection technique can be further employed to achieve the real-time control of the patterning depth via controlling the ion dose or milling time during the process of plasmonic structure fabrication. Accordingly, the patterning geometries and dimensions can be changed after determining the ion dose required for patterning at or near the interface via interface detection for the Ag-coated substrate with a multilayer structure based on (1).

As shown in Figures 7 and 8, some Ag-coated plasmonic nanostructures have been fabricated and measured using the FIB/SEM system and AFM based on the achieved methodology of the interface detection for FIB nanofabrication of the plasmonic structures, including nanoscale pentagram hole/particle arrays and square nanohole arrays. The primary concern for FIB nanofabrication of these plasmonic structures is the precise dimension and patterning control for fabricating the nanoscale hole/particle arrays; for example, the concern for angle fabrication requires high machining resolution and small beam spot diameter, which requires relatively small ion beam currents (e.g., 10–50 pA) although the fabrication efficiency is low. In addition, the AFM-measured depth of the fabricated nanoholes is around 135 nm (Figure 7), which nearly agrees with the film thickness 132 nm measured through the interface detection (Figure 3), demonstrating the feasibility and reliability of the achieved methodology for the real-time precise patterning depth control during the plasmonic nanostructure fabrication process based on the FIB-assisted interface detection.

The developed nanoscale hole/particle arrays can find potential plasmonic device applications (e.g., biosensors) through detecting the LSPR signals of the optical field intensity distribution, optical spectra, and/or refractive indices for the analytes via transmission and/or reflection mode sensing [32, 36–42]. It is reported that the plasmonic pentagram nanoholes can significantly enhance transmission and E-field, and the plasmonic pentagram nanohole array can enhance the LSPR. Thus, the plasmonic pentagram nanoholes have potential applications in the fields of imaging, focusing, and biosensing [41].

Figure 9 is a schematic example to illustrate the application for transmission mode sensing using a plasmonic nanohole array, where the transmitted optical field intensity for the analytes can be detected by the scanning near-field optical microscope (SNOM) tip for the sensing signal. The transmission (reflection) mode means that the light illuminates the plasmonic structure from the substrate (analyte) side, and the detection is at the analyte side.

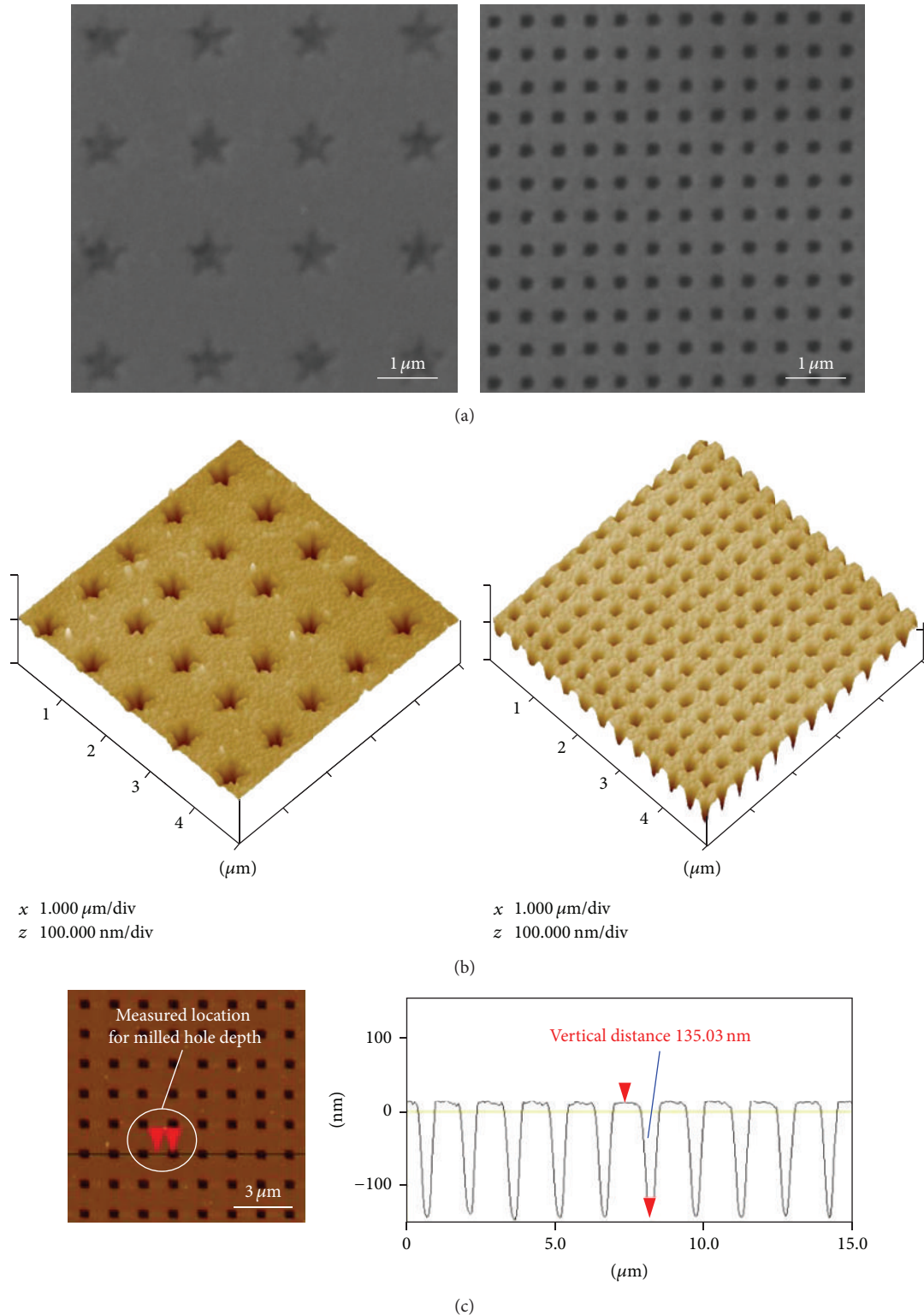


FIGURE 7: FIB-fabricated pentagram and square plasmonic nanohole arrays measured using the (a) SEM and ((b)-(c)) AFM.

6. Conclusion

The FIB-assisted interface detection was proposed and successfully carried out using the sample-absorbed current as

the detection signal, and the patterning depth control for the plasmonic structure fabrication was achieved through controlling machining time or ion dose using the EPM. Material-dependent currents were measured through the EPM signal

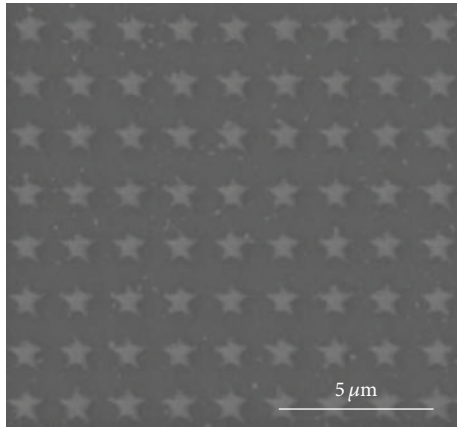


FIGURE 8: FIB-fabricated pentagram plasmonic nanostar array measured using the SEM.

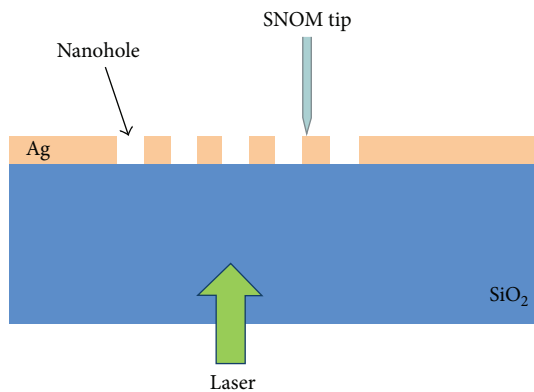


FIGURE 9: Sketch for illustrating the principle of transmission mode sensing based on a plasmonic nanohole array.

curves, and the quantitative models for the sample-absorbed currents and the ion beam current were also developed. The functional plasmonic nanostructures (pentagram nanoscale hole/particle arrays and square nanohole arrays for the potential LSPR biosensing applications) were fabricated and measured based on the achieved systematic methodology of the interface detection for FIB nanofabrication of patterned nanostructures for potential plasmonic device applications (e.g., LSPR biosensors). It was shown that the proposed methodology on the FIB-assisted interface detection can be conveniently used for the real-time control and precise fabrication of different functional plasmonic nanostructures with different geometries and dimensions.

Conflict of Interests

The authors declare that there is no conflict of interests regarding the publication of this paper.

Acknowledgments

The work is supported by the Research Foundation for Advanced Talents of Jiangsu University under Grant no.

14JDG020, China, and the A*STAR (Agency for Science, Technology and Research) under SERC Grant no. 072 101 0023, Singapore.

References

- [1] Z. Yu, H. Gao, W. Wu, H. Ge, and S. Y. Chou, "Fabrication of large area subwavelength antireflection structures on Si using trilayer resist nanoimprint lithography and liftoff," *Journal of Vacuum Science and Technology B*, vol. 21, no. 6, p. 2874, 2003.
- [2] G. Kostovski, D. J. White, A. Mitchell, and P. R. Stoddart, "Nanoimprinting on optical fiber end faces for chemical sensing," in *19th International Conference on Optical Fibre Sensors*, vol. 7004 of *Proceedings of SPIE*, April 2008.
- [3] S. A. Boden and D. M. Bagnall, "Tunable reflection minima of nanostructured antireflective surfaces," *Applied Physics Letters*, vol. 93, no. 13, Article ID 133108, 2008.
- [4] Y. Lin, Y. Zou, Y. Mo, J. Guo, and R. G. Lindquist, "E-beam patterned gold nanodot arrays on optical fiber tips for localized surface plasmon resonance biochemical sensing," *Sensors*, vol. 10, no. 10, pp. 9397–9406, 2010.
- [5] Y. Lin, Y. Zou, and R. G. Lindquist, "A reflection-based localized surface plasmon resonance fiber-optic probe for biochemical sensing," *Biomedical Optics Express*, vol. 2, no. 3, pp. 478–484, 2011.
- [6] N. Chekurov, K. Grigoras, A. Peltonen, S. Franssila, and I. Tittonen, "The fabrication of silicon nanostructures by local gallium implantation and cryogenic deep reactive ion etching," *Nanotechnology*, vol. 20, no. 6, Article ID 065307, 2009.
- [7] Y. F. Chang, Q. R. Chou, I. Y. Lin, and C. H. Lee, "Fabrication of high-aspect-ratio silicon nanopillar arrays with the conventional reactive ion etching technique," *Applied Physics A*, vol. 86, pp. 193–196, 2007.
- [8] S. H. G. Teo, A. Q. Liu, G. L. Sia, C. Lu, J. Singh, and M. B. Yu, "Deep reactive ion etching for pillar type nanophotonic crystal," *International Journal of Nanoscience*, vol. 4, no. 4, pp. 567–574, 2005.
- [9] N. A. Kouklin and J. Liang, "Ultradense GaN nanopillar and nanopore arrays by self-assembly nanopatterning," *Journal of Electronic Materials*, vol. 35, no. 5, pp. 1133–1137, 2006.
- [10] S. W. Kim, "High-temperature fiber optic sensor using a grating on an angled fiber tip," *Japanese Journal of Applied Physics*, vol. 41, no. 3, p. 1431, 2002.
- [11] X. Ma, H. Huo, W. Wang et al., "Surface-enhanced Raman scattering sensor on an optical fiber probe fabricated with a femtosecond laser," *Sensors*, vol. 10, no. 12, pp. 11064–11071, 2010.
- [12] J. W. Menezes, J. Ferreira, M. J. L. Santos, L. Cescato, and A. G. Brolo, "Large-area fabrication of periodic arrays of nanoholes in metal films and their application in biosensing and plasmonic-enhanced photovoltaics," *Advanced Functional Materials*, vol. 20, no. 22, pp. 3918–3924, 2010.
- [13] S. E. Wu, C. P. Liu, T. H. Hsueh, H. C. Chung, C. C. Wang, and C. Y. Wang, "Anomalous formation of InGaN/GaN multiple-quantum-well nanopillar arrays by focused ion beam milling," *Nanotechnology*, vol. 18, no. 44, Article ID 445301, 2007.
- [14] I. Utke, P. Hoffmann, and J. Melngailis, "Gas-assisted focused electron beam and ion beam processing and fabrication," *Journal of Vacuum Science and Technology B*, vol. 26, no. 4, pp. 1197–1276, 2008.
- [15] M. Kolibal, T. Matlocha, T. Vystavěl, and T. Šikola, "Low energy focused ion beam milling of silicon and germanium

- nanostructures," *Nanotechnology*, vol. 22, no. 10, Article ID 105304, 2011.
- [16] H. X. Wang, W. Zhou, Y. Cui, G. H. Wang, and P. P. Shum, "Focused ion beam nanoscale patterned transmission-enhanced fiber-optic tips," *Journal of Nanoscience and Nanotechnology*, vol. 13, no. 7, pp. 4581–4586, 2013.
- [17] H. X. Wang and W. Zhou, "Focused ion beam nanomachining for analyzing effects of light-structure interaction on hair color," *Journal of Biomaterials and Tissue Engineering*, vol. 4, no. 5, pp. 411–415, 2014.
- [18] W. Zhou, H. X. Qian, and L. M. Wang, "Maskless fabrication of highly-ordered periodic nanopillars using FIB and Bitmap control," *Microscopy and Microanalysis*, vol. 11, supplement 2, pp. 822–823, 2005.
- [19] S. Zhu and W. Zhou, "Optical properties and immunoassay applications of noble metal nanoparticles," *Journal of Nanomaterials*, vol. 2010, Article ID 562035, 12 pages, 2010.
- [20] O. Kvítek, J. Siegel, V. Hnatowicz, and V. Švorčík, "Noble metal nanostructures influence of structure and environment on their optical properties," *Journal of Nanomaterials*, vol. 2013, Article ID 743684, 15 pages, 2013.
- [21] M. G. Sreenivasan, S. Malik, S. Thigulla, and B. R. Mehta, "Dependence of plasmonic properties of silver island films on nanoparticle size and substrate coverage," *Journal of Nanomaterials*, vol. 2013, Article ID 247045, 8 pages, 2013.
- [22] T. Zhang and F. Shan, "Development and application of surface plasmon polaritons on optical amplification," *Journal of Nanomaterials*, vol. 2014, Article ID 495381, 16 pages, 2014.
- [23] H. X. Qian, W. Zhou, X. M. Li, J. M. Miao, and L. E. N. Lim, "Accurate detection of interface between SiO₂ film and Si substrate," *Applied Surface Science*, vol. 253, no. 12, pp. 5511–5515, 2007.
- [24] S. T. Davies and B. Khamsehpour, "End-point detection using absorbed current, secondary electron, and secondary ion signals during milling of multilayer structures by focused ion beam," *Journal of Vacuum Science & Technology B*, vol. 11, no. 2, pp. 263–267, 1993.
- [25] Y. Z. Huang and D. Cockayne, "Control of nanostructures induced by ion sputtering," *Nanotechnology*, vol. 18, no. 2, Article ID 025305, 2007.
- [26] R. Hill, J. C. Morgan, R. G. Lee, and T. Olson, "FIB endpoint detection and depth resolution," *Microelectronic Engineering*, vol. 21, no. 1–4, pp. 201–204, 1993.
- [27] H. X. Qian and W. Zhou, "Focused ion beam irradiation of ZnO film: an atomic force microscopy study," *Journal of Physics D: Applied Physics*, vol. 42, no. 10, Article ID 105304, 2009.
- [28] B. Khamsehpour and S. T. Davies, "Micromachining of semiconductor materials by focused ion beams," *Vacuum*, vol. 45, no. 12, pp. 1169–1173, 1994.
- [29] L. R. Harriott, A. Wagner, and F. Fritz, "Integrated circuit repair using focused ion beam milling," *Journal of Vacuum Science & Technology B*, vol. 4, p. 181, 1986.
- [30] P. J. Heard, J. R. A. Cleaver, and H. Ahmed, "Application of a focused ion beam system to defect repair of VLSI masks," *Journal of Vacuum Science and Technology B*, vol. 3, no. 1, p. 87, 1985.
- [31] S. L. Zhu, W. Zhou, G.-H. Park, and E. P. Li, "Numerical design methods of nanostructure array for nanobiosensing," *Plasmonics*, vol. 5, no. 3, pp. 267–271, 2010.
- [32] L. Wu, P. Bai, X. Zhou, and E. P. Li, "Reflection and transmission modes in nanohole-array-based plasmonic sensors," *IEEE Photonics Journal*, vol. 4, no. 1, pp. 26–33, 2012.
- [33] L. Pang, G. M. Hwang, B. Slutsky, and Y. Fainman, "Spectral sensitivity of two-dimensional nanohole array surface plasmon polariton resonance sensor," *Applied Physics Letters*, vol. 91, no. 12, Article ID 123112, 2007.
- [34] T. Chung, S.-Y. Lee, E. Y. Song, H. Chun, and B. Lee, "Plasmonic nanostructures for nano-scale bio-sensing," *Sensors*, vol. 11, no. 11, pp. 10907–10929, 2011.
- [35] A.-P. Blanchard-Dionne, L. Guyot, S. Patskovsky, R. Gordon, and M. Meunier, "Intensity based surface plasmon resonance sensor using a nanohole rectangular array," *Optics Express*, vol. 19, no. 16, pp. 15041–15046, 2011.
- [36] G. Si, A. J. Danner, S. L. Teo, E. J. Teo, J. Teng, and A. A. Bettiol, "Photonic crystal structures with ultrahigh aspect ratio in lithium niobate fabricated by focused ion beam milling," *Journal of Vacuum Science & Technology B: Microelectronics and Nanometer Structures*, vol. 29, no. 2, Article ID 021205, 2011.
- [37] R. M. Langford, P. M. Nellen, J. Gierak, and Y. Fu, "Focused ion beam micro- and nanoengineering," *MRS Bulletin*, vol. 32, no. 5, pp. 417–423, 2007.
- [38] Z. L. Wang, Q. Wang, H. J. Li et al., "The field emission properties of high aspect ratio diamond nanocone arrays fabricated by focused ion beam milling," *Science and Technology of Advanced Materials*, vol. 6, no. 7, pp. 799–803, 2005.
- [39] O. Wilhelmi, S. Reyntjens, C. Mitterbauer, L. Roussel, D. J. Stokes, and D. H. W. Hubert, "Rapid prototyping of nanostructured materials with a focused ion beam," *Japanese Journal of Applied Physics*, vol. 47, no. 6, pp. 5010–5014, 2008.
- [40] G. H. Wang, X. T. Zheng, P. P. Shum, C. M. Li, H. P. Ho, and L. M. Tong, "Live cell index sensing based on the reflection mode of tilted fiber tip with gold nanoparticles," in *Proceedings of the 9th International Conference on Optical Communications and Networks*, vol. 574CP, p. 116, Nanjing, China, 2010.
- [41] S. Zhu and W. Zhou, "Plasmonic properties of two-dimensional metallic nanoholes fabricated by focused ion beam lithography," *Journal of Nanoparticle Research*, vol. 14, article 652, 2012.
- [42] S. L. Zhu and W. Zhou, "Optical properties of pentagram nanostructures based on localized surface plasmon resonance," *Journal of Optics*, vol. 40, no. 2, pp. 65–70, 2011.